Institut für Ionenstrahlphysik und Materialforschung
Forschungszentrum Dresden-Rossendorf

Transition metal implanted ZnO: a correlation between structure and magnetism

Dissertation

zur Erlangung des akademischen Grades
Doctor rerum naturalium (Dr. rer. nat.)

vorgelegt der Fakultät Mathematik und Naturwissenschaften
der Technischen Universistät Dresden

von
Shengqiang Zhou
geboren am 16.08.1976 in China

Dresden 2008

Gutachter:

1. Prof. Dr. Manfred Helm
2. Prof. Dr. Bruno K. Meyer
3. PD Dr. Jürgen Fassbender

ACKNOWLEDGEMENTS

There are lots of people I would like to thank for various reasons.

Firstly, I would like to thank my promotor, Prof. Manfred Helm, for his suggestions as I worked through problems and for his critical reading of this thesis.

I would like to thank my supervisor, Dr. Kay Potzger, for his constant support, hand-on instructions, and efforts to establish internal and external cooperation throughout my study.

I would like to thank Dr. Wolfgang Skorupa, and Dr. Jürgen Fassbender. Thank you for the friendly, flexible working atmosphere, many suggestions on techniques and data interpretation. Of course, I cannot forget all the group members from FWIM and FWIN, and I love this environment created by all of you!

I appreciate Mr. Frank Ludewig, Mr. Gunter Winkler, as well as Mr. Jörg Schneider, Mr. Stefan Eisenwinder for their work on ion implantation. Without their help, I could not finish this thesis.

I am grateful to Mr. Georg Talut and Dr. Helfried Reuther, for their help in CEMS measurement, and data interpretation.

I thank Dr. Karsten Küpper for XAS and XMCD measurements and useful discussion. I also thank Dr. Qingyu Xu, and Dr. Heidemarie Schmidt for transport measurement for my samples.

Additional thanks are due to Mrs. Andrea Scholz, Mrs. Valentina Cantelli, Mr. Gufei Zhang (now at Leuven, Belgium), Dr. Rainer Grötzschel, Dr. Frank Eichhorn, Dr. Johannes von Borany, Dr. Jörg Grenzer, Dr. Carsten Bähtz, Dr. Arndt Mücklich and Dr. Bernd Schmidt, for many conversations, suggestions, and assistance in XRD, RBS, TEM measurements and sample processing.

I also appreciate Dr. Thomas Herrmannsdörfer from High Field Lab for his help in SQUID installation and measurement, Dr. Niklas Volbers from Gießen for his help in SIMS measurement, and Dr. Micheal Lorenz from Leipzig for his help in sample growth and transport measurement.

Finally, I must say 'thank-you' to my family, wherever they are, particularly my wife, Rong, and my son De Jian. They remind me what is the most important in my life, and give me the possibility to get rid of the thesis work from my head for a while.

Shengqiang Zhou

07.12.2007

ABSTRACT

Nowadays ferromagnetism is often found in potential diluted magnetic semiconductor systems. However, many authors question the origin of this ferromagnetism, *i.e.* if the observed ferromagnetism stems from ferromagnetic precipitates rather than from carrier-mediated magnetic coupling of ionic impurities, as required for a diluted magnetic semiconductor. In this thesis, this question will be answered for transition-metal implanted ZnO single crystals. Magnetic secondary phases, namely metallic Fe, Co and Ni nanocrystals, are formed inside ZnO. They are - although difficult to detect by common approaches of structural analysis - responsible for the observed ferromagnetism. Particularly Co and Ni nanocrystals are crystallographically oriented with respect to the ZnO matrix. Their structure phase transformation and corresponding evolution of magnetic properties upon annealing have been established. Finally, an approach, pre-annealing ZnO crystals at high temperature before implantation, has been demonstrated to sufficiently suppress the formation of metallic secondary phases.

Kurzfassung

Potentiellen verdünnten magnetischen Halbleitern (engl.: DMS) werden heutzutage häufig ferromagnetische Eigenschaften zugeschrieben. Die Ursache dieses Ferromagnetismus ist allerdings noch nicht eindeutig geklärt, *d.h.* ob er von partikulären magnetischen Fremdphasen oder von einer indirekten Austauschwechselwirkung vermittelt durch die freien Ladungsträger herrührt. In meiner Dissertation wird diese Frage für ZnO-Einkristalle, die mit Übergangsmetallionen implantiert wurden, beantwortet. Magnetische Fremdphasen, *d.h.* Fe-, Co- und Ni-Nanokristalle, werden durch diese Präparationsmethode innerhalb des ZnO Wirtskristalls geformt. Diese sind verantwortlich für den beobachteten Ferromagnetismus, allerdings nur schwer durch gängige Strukturanalytik zu identifizieren. Speziell Co- und Ni- Nanokristalle sind kristallographisch in der ZnO-Matrix orientiert. Die Veränderung struktureller und magnetischer Eigenschaften dieser und anderer Dotanden aufgrund von Temperung wurde in dieser Arbeit untersucht. Schließlich stellen wir eine Methode vor, durch die die Formierung metallischer Fremdphasen verhindert werden kann, nämlich das Tempern des ZnO in Vakuum vor der Implantation.

Contents

ACKNOWLEDGEMENT **v**

ABSTRACT **vii**

1 Introduction **1**
1.1 Spintronics . . . 1
1.2 The aim of this thesis . . . 2

2 Fundamentals **5**
2.1 Ferromagnetic semiconductors . . . 5
2.1.1 Rare-earth chalcogenides . . . 5
2.1.2 Diluted magnetic semiconductors . . . 6
2.1.3 Ferromagnetic DMS . . . 6
2.2 Phase separation in DMS . . . 9
2.3 Magnetic nanoparticles . . . 12
2.4 Granular magnetic semiconductors . . . 15

3 Experimental Methods **17**
3.1 Ion Implantation . . . 17
3.1.1 Advantages of ion implantation . . . 17
3.1.2 Interaction between energetic ions and solids . . . 17
3.2 X-ray diffraction . . . 19
3.2.1 Basics of X-ray diffraction . . . 19
3.2.2 Phase identification: 2θ-θ scan . . . 20
3.2.3 Orientation: ϕ-scan and pole figure . . . 20
3.2.4 Synchrotron radiation XRD . . . 21
3.3 SQUID Magnetometry . . . 22
3.3.1 SQUID Magnetometry . . . 22
3.3.2 Notes on errors in SQUID measurement . . . 24
3.4 RBS/channeling . . . 24
3.4.1 Physical concepts . . . 24
3.4.2 Channeling . . . 26
3.5 Conversion Electron Mössbauer Spectroscopy . . . 27

4 Fe implanted ZnO: magnetic precipitates versus dilution **29**
4.1 Experiments . . . 30
4.2 Results . . . 30
4.2.1 Lattice damage accumulation . . . 30
4.2.2 Fe distribution . . . 33
4.2.3 Formation of Fe NCs . . . 34
4.2.4 Charge state of Fe . . . 36

4.2.5 Magnetic properties Fe implanted ZnO . . . 39
4.2.6 Fe implanted epitaxial ZnO layers . . . 44
4.2.7 Synthesis of magnetic $ZnFe_2O_4$ . . . 47
4.3 Discussion . . . 52
4.3.1 Phase diagram of Fe in ZnO . . . 52
4.3.2 Phase separation depends on ZnO materials . . . 53
4.3.3 Annealing behavior depends on the initial state . . . 54
4.3.4 Magnetic coupling of dispersed ionic Fe . . . 54
4.4 Summary and Conclusions . . . 55

5 Co and Ni implanted ZnO: crystallographically oriented precipitates 57
5.1 Experiments . . . 57
5.2 As-implanted samples . . . 58
5.2.1 ZnO lattice damage upon implantation . . . 58
5.2.2 Crystallographically oriented Co and Ni NCs . . . 58
5.2.3 Magnetic properties of Co and Ni NCs . . . 61
5.3 The effect of post-annealing . . . 64
5.3.1 Lattice recovery . . . 64
5.3.2 Evolution of structural properties . . . 65
5.3.3 Evolution of magnetic properties . . . 68
5.4 Discussion . . . 70
5.4.1 Magnetic anisotropy of Co and Ni NCs . . . 70
5.4.2 Annealing at 923 K . . . 72
5.5 Conclusions . . . 74

6 Suppression of secondary phase formation 75
6.1 Experiments . . . 75
6.2 Results and discussion . . . 76
6.3 Conclusion . . . 82

7 Transition metal implanted Si and TiO_2 83
7.1 Mn-implanted Si . . . 83
7.1.1 Introduction . . . 83
7.1.2 Experiments . . . 84
7.1.3 Results and discussion . . . 84
7.1.4 Conclusion . . . 86
7.2 TM-implanted TiO_2 (TM=Fe, Co, Ni) . . . 86

8 Conclusions and future trends 89
8.1 Formation of magnetic secondary phases . . . 89
8.2 Detecting crystalline secondary phases . . . 90
8.3 Suppression of secondary phases . . . 90
8.4 Suggestion on future work . . . 91
8.4.1 Granular magnetic semiconductors . . . 91
8.4.2 Anomalous magnetism induced by defects . . . 91

Bibliography 93

A Publications 107

B Curriculum vitae 111

Chapter 1

Introduction

In traditional electronic devices, charge and spin are used separately. Charge, on one hand, is used for the computing. Transistors operate by controlling the flow of carriers through the semiconductor by applied electric fields. Spin, on the other hand, is used for the magnetic data storage. The word "spintronics" (short for "spin electronics") refers to devices that manipulate the freedom of spin degree. A new generation of devices based on the manipulation of spins may have completely new functionality, therefore drastically improves the computation speed and reduces power consumption.

1.1 Spintronics

The first successful application of spintronics is the Giant Magnetoresistive (GMR) spin-valve read-head for magnetic hard-disk drives. Magnetoresistance describes the dependence of electric resistance on the magnetic field applied to the material. The discovery of GMR [1, 2] is considered as the birth of spintronics.

Datta and Das [3] extended the principle of spintronics to semiconductors. They proposed a spin-FET (field effect transistor), where the source and the drain are ferromagnets acting as the injector and detector of the electron spin. By modifying the gate voltage, the spin current can be controlled. The spin injector can be a ferromagnetic metal or a ferromagnetic semiconductor. The crucial problem is the efficiency of the spin injection, *i.e.* the amount of carriers that can persist their spin state in a long enough distance. While the degree of spin polarization for metallic spin injection is limited [4], a magnetic semiconductor could allow a robust spin injection into a nonmagnetic semiconductor. Thus it would facilitate the integration of spintronics and semiconductor-based electronics. For instance, semiconductors offer a tunability of the carrier concentration by orders of magnitude (ranging from almost insulating to metallic behavior) by controlled doping with donor or acceptor impurities. Therefore a huge effort is dedicated to find or to artificially fabricate a ferromagnetic semiconductor with the following requirements [5].

- The material should possess ferromagnetism which is induced by a low-density carrier

system so that magnetic properties can be tuned over a wide range by doping or by gates.

- The material should have a ferromagnetic transition temperature above 300 K for regular application.

- The material should be structurally compatible with conventional semiconductors, so that the magnetic and spin-related phenomena can be integrated with the mainstream microelectronics and optoelectronics as well as taking advantage of the already established fabrication processes.

1.2 The aim of this thesis

Among ferromagnetic semiconductors, (Ga,Mn)As, a diluted magnetic semiconductor (DMS), is the most well understood and promising for application in spintronics (Section 2.1). The main obstacle is that the highest Curie temperature of (Ga,Mn)As is reported to be 173 K [6], far below room temperature. Nevertheless, the spin-related devices based on (Ga,Mn)As, namely spin-polarized light emitter (spin-LED) [7], spin FET [8] and spinvalve [9], have been demonstrated at ***low temperature***. Now it is well accepted that (Ga,Mn)As materials can be used as a test bed for the future spintronics device [10].

Dietl *et al.* [11] proposed the mean-field Zener model to understand the ferromagnetism in DMS materials. It has been successfully applied in (Ga,Mn)As and (Zn,Mn)Te materials. This model predicts that wide bandgap semiconductor (WBS) like p-type GaN or ZnO doped with Mn can exhibit critical temperatures above 300 K. With this prediction, the mining for the room temperature DMS based on WBS has been drastically boosted. However the results are very disperse and controversial concerning the magnetization, the Curie temperature and the origin of the ferromagnetism. As stated in recent review articles [12, 13, 14, 15], the critical unanswered question is 'whether the resulting material indeed contains *uniformly distributed* transition-metal elements or contains *clusters, precipitates or second phases* that are responsible for the observed magnetic properties'. This can only be answered *by a careful correlation of the measured magnetic properties with analysis methods that are capable of detecting precipitates and preferably element-selective.* **That is the aim of this thesis**. With this aim, the thesis is organized as follows.

In Chapter 2, we will give a review on the history of ferromagnetic semiconductors, ZnO based DMS materials, and the phase separation in DMS materials. In chapter 3, the experimental methods used in this thesis are briefly introduced.

In Chapter 4, the dilution and precipitation of Fe in ZnO will be presented. Different implantation fluences and temperatures and post-implantation annealing temperatures have been chosen in order to evaluate the structural and magnetic properties over a wide range of parameters. Three different regimes with respect to the Fe concentration and the process

temperature are found: 1) Disperse Fe^{2+} and Fe^{3+} at low Fe concentrations and low processing temperatures, 2) $FeZn_2O_4$ at very high processing temperatures and 3) an intermediate regime with a co-existence of metallic Fe (Fe^0) and ionic Fe (Fe^{2+} and Fe^{3+}). Ferromagnetism is only observed in the latter two cases, where inverted $ZnFe_2O_4$ and α-Fe nanocrystals are the origin of the observed ferromagnetic behavior, respectively. The ionic Fe in the last case could contribute to a carrier mediated coupling. However, their separation is too large to couple ferromagnetically due to the lack of p-type carrier. For comparison investigations of Fe-implanted epitaxial ZnO thin films are presented. Additionally, crystallographically oriented Zn-ferrites have been synthesized by Fe implantation into ZnO and post annealing.

In Chapter 5, a thorough characterization of the structural and magnetic properties of Co and Ni implanted ZnO single crystals will be presented. The measurements reveal that Co or Ni nanocrystals (NCs) are the major contribution of the measured ferromagnetism. Already in the as-implanted samples, Co or Ni NCs have formed, and they exhibit superparamagnetic properties. The Co or Ni NCs are crystallographically oriented with respect to the ZnO matrix. Their magnetic properties, *e.g.* the anisotropy and the superparamagnetic blocking temperature can be tuned by annealing. The magnetic anisotropy of Ni NCs embedded in ZnO will be discussed concerning the strain anisotropy.

In Chapter 6, an approach, *i.e.* pre-annealing of the substrate before implantation, is given to suppress the formation of secondary phase in Fe implanted ZnO. In as-purchased ZnO crystals upon Fe implantation and post-annealing, α-Fe has formed. However, the same implantation and post-annealing leads the single phase formation in ZnO substrates, which are pre-annealed at high temperature in O_2 or in high vacuum.

In Chapter 7, a brief description will be given on the structural and magnetic properties of Si implanted with Mn, and TiO_2 implanted with Fe, Co and Ni.

In Chapter 8, all results will be summarized and some instructions for future work will be given.

Chapter 2

Fundamentals

2.1 Ferromagnetic semiconductors

2.1.1 Rare-earth chalcogenides

Since the 1960's rare-earth chalcogenides (*e.g.* EuO [16]) were found to possess both ferromagnetic and semiconducting properties. In these magnetic semiconductors, all magnetic atoms are periodically arranged in the crystal lattice as shown in Figure 2.1(a). Such ferromagnetic semiconductors show low transition temperatures usually not exceeding 70 K, *i.e.* far below room temperature. Moreover, the crystal structure of the rare-earth chalcogenides is quite different from that of technologically relevant semiconductors such as GaAs or Si, therefore these materials are rather difficult to integrate into semiconductor heterostructures for spintronic applications. But people never stop the effort to exceed these limitations. For instance, very recently GdN thin films have been epitaxially grown onto MgO with a T_C of around 70 K [17].

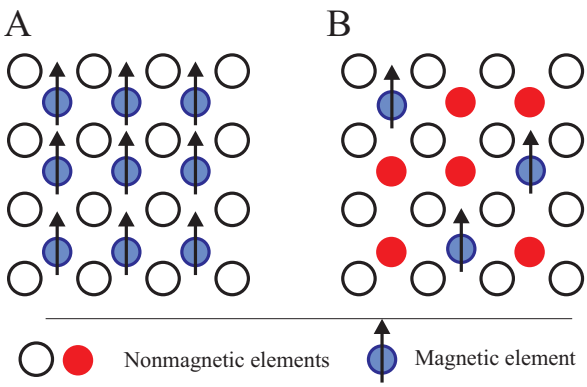

Figure 2.1: Schematic representation of (A) a magnetic semiconductor, and (B) a diluted magnetic semiconductor. Adapted from ref. [14].

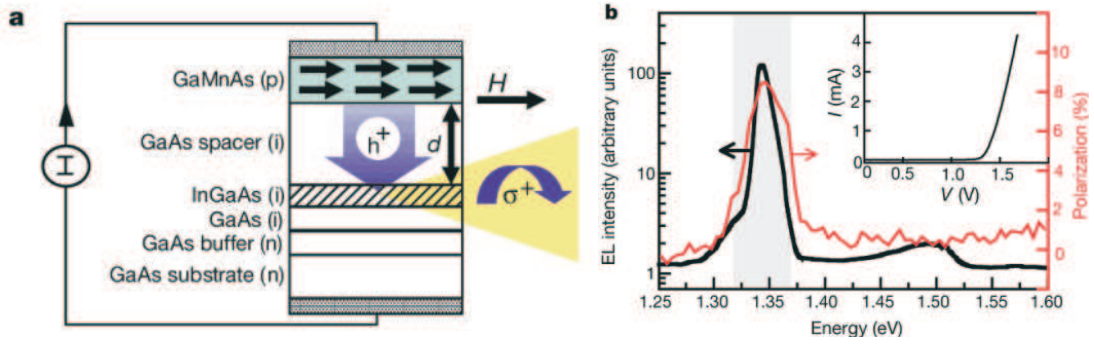

Figure 2.2: Electrical spin injection in an epitaxially grown ferromagnetic semiconductor heterostructure, based on GaAs. (a)Under forward bias, spin-polarized holes from (Ga,Mn)As and unpolarized electrons from the n-type GaAs substrate are injected into the (In,Ga)As quantum well (hatched region), through a spacer layer with thickness d, producing polarized electroluminescence. (b) Total electroluminescence intensity under forward bias at temperature T = 6 K and magnetic field H = 1000 Oe is shown with its corresponding polarization. From ref. [7].

2.1.2 Diluted magnetic semiconductors

A landmark towards application was the discovery of diluted magnetic semiconductors (DMS). DMS materials are semiconductors in which a fraction of the host cations can be substitutionally replaced by transition metal or rare earth ions (as shown in Figure 2.1(B)). The partially filled $3d$ states or $4f$ states contain unpaired electrons, which are responsible for localized magnetic moments.

Transition metal doped II-VI compounds (such as $Cd_{1-x}Mn_xSe$, $Hg_{1-x}Mn_xTe$, etc.) are the most common DMSs studied in the early period [18]. As the magnetic interaction in the II-VI DMS is dominated by antiferromagnetic exchange between the transition metal moments, only paramagnetic, antiferromagnetic, spin-glass behavior, or ferromagnetism with T_C as low as 1.8 K have been observed [19]. The difficulty in creating high p- and n-type doping levels, which is essential for obtaining high Curie temperatures, makes these systems less attractive for applications.

2.1.3 Ferromagnetic DMS

The research on DMS was greatly paved by the work of H. Ohno in Mn doping of InAs [20] and GaAs [21]. The discovery of hole-mediated ferromagnetism in (Ga,Mn)As opened the way to integrate spintronics with the mainstream microelectronics and optoelectronics as well as taking advantage of the already established fabrication processes. Until now, based on GaMnAs and InMnAs, electrically controlled spintronic devices have been successfully designed and tested at low temperatures. For instance, a spin-LED using GaMnAs as a spin injector has been demonstrated by Ohno *et al.* as shown in Figure 2.2[7].

The highest T_C reported in (Ga,Mn)As grown by molecular beam epitaxy (MBE), however, is $\sim$ 170 K [6], which limits the application of GaAs-based DMS.

In order to well understand the ferromagnetism in DMS, and to find new DMS materials

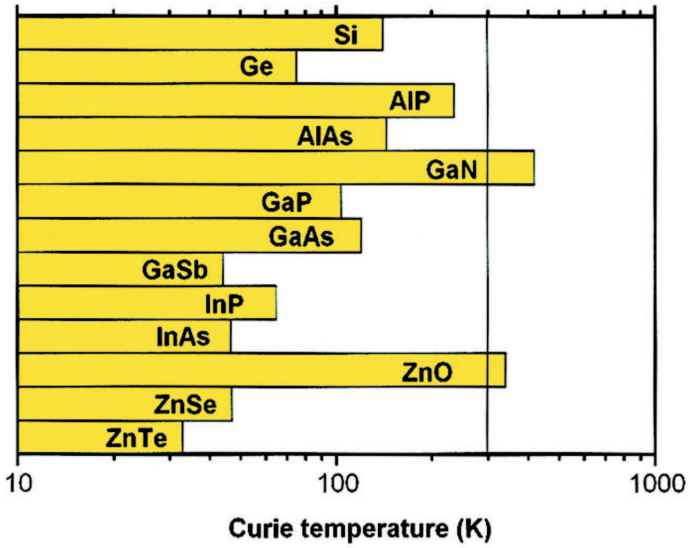

Figure 2.3: Predicted Curie temperatures as a function of the band gap. Computed values of the Curie temperature T_C for various p-type semiconductors containing 5% of Mn and 3.5×10^{20} holes per cm^3. From ref. [11]

with higher T_C, researchers have developed models to describe the magnetic interactions.

One of the most cited model is the the mean-field Zener model proposed by Dietl *et al.* [11]. It has been successful in explaining the transition temperatures observed for p-(Ga,Mn)As and (Zn,Mn)Te. The mean-field Zener theory is based on the original model of Zener and the Ruderman-Kittel-Kasuya-Yoshida (RKKY) interaction. An important aspect of the Dietl model is that it takes into account the anisotropy of the carrier-mediated exchange interaction associated with the spin-orbit coupling in the host material. It reveals the important effect of the spin-orbit coupling in the valence band in determining the magnitude of the Curie temperature and the direction of the easy axis in p-type ferromagnetic semiconductors. The Curie temperature is proportional to the density of Mn ions and hole density. This model suggests that Mn doped GaN and ZnO can exhibit critical temperatures above 300 K due to the small spin-orbit coupling, provided that a sufficiently high hole density can be achieved (10^{20} cm^{-3}), as shown in Figure 2.3. According to this model, it is difficult to achieve ferromagnetism in n-type semiconductors due to the generally smaller *s-d* interaction.

In contrast, Sato *et al.* used the Korringa-Kohn-Rostoker (KKR) Green function method based on the local density approximation of density functional theory to calculate the properties of n-type ZnO doped with 25% of 3*d* TM ions (V, Cr, Mn, Fe, Co, and Ni) [22]. The ferromagnetic state was predicted to be favorable for V, Cr, Fe, Co, and Ni in ZnO while Mn-doped ZnO was antiferromagnetic.

In addition to the models mentioned above, Coey *et al.* used a spin-split donor impurity-band model to explain the observed systematic variation of magnetic moments across the TM-doped ZnO series, where V and Co showed much larger magnetic moment than other TM metals [23]. For the light 3*d* elements, the $3d\uparrow$ states lie high in the $2p$(O) and $4s$(Zn)

Table 2.1: Basic properties of wurtzite ZnO. Adapted from ref. [25]

Property	Value
Stable phase at 300 K	Wurtzite
Lattice parameters at 300 K	
a	0.324 95 nm
c	0.520 69 nm
Energy gap	3.2 eV, direct
Density	5.606 g/cm^3
Melting point	1975 °C
Thermal conductivity	0.6, 1-1.2 W/(m·K)
Static dielectric constant	8.656
Intrinsic carrier concentration	$<10^6$ cm^{-3}
Electron effective mass	0.24 m$_e$
Electron Hall mobility at 300 K for low n-type conductivity	200 cm^2/V·s
Hole effective mass	0.59 m$_e$
Hole Hall mobility at 300 K for low p-type conductivity	5-50 cm^2/V·s

gap, overlapping the donor impurity band which is spin split. In the middle of the TM series, for instance Mn, there is no overlap with the 3d levels and exchange is weak, but towards the end of the series the 3$d\downarrow$ states overlap the impurity band, which then has the opposite spin splitting for the same occupancy. High Curie temperatures are found whenever unoccupied 3d states overlap the impurity band, but not otherwise. The likely origin of the donor impurity band in ZnO films is lattice defects, such as oxygen vacancies.

These predictions boosted intensive experimental activity on transition metal doped wide bandgap semiconductors. Among them, transition metal doped ZnO is one of the most promising systems.

ZnO is a direct band gap semiconductor with the bandgap of $\sim$3.3 eV at 300 K. ZnO normally has a hexagonal (wurtzite) crystal structure. The Zn atoms are tetrahedrally coordinated to four O atoms, where the Zn d electrons hybridize with the O p electrons. The basic properties are listed in Table 2.1. The band gap of ZnO can be tuned via divalent substitution on the cation site to produce heterostructures. For example, Cd substitution leads to a reduction in the band gap to 3.0 eV. Substituting Mg on the Zn site in epitaxial films can increase the band gap to approximately 4.0 eV while still maintaining the wurtzite structure. ZnO is usually n-type due to electron doping via defects originating from Zn interstitials, O vacancies in the ZnO lattice, or impurities including hydrogen. High electron carrier density can also be realized via group III substitutional doping. Until recently, however, ZnO has proven difficult to dope p type. This is fairly common in wide band-gap semiconductors. A comprehensive review of ZnO is given in Ref. [24].

Considering the magnetic properties, Han *et al.* reported room-temperature ferromag-

Table 2.2: List of recently reported ZnO:TM based DMS materials prepared by various methods.

Compound	TM content	Substrate or bulk	Preparation method	Preparation Temperature (°)	T_C(K)	Ref.
(Zn,Co)O	0.1	Al_2O_3	Implantation	300	>300	[40]
(Zn,CoFe)O	0.15	Si	Sputtering	600	>300	[41]
(Zn,Co)O	0.017		Electrodeposition	90	>300	[42]
(Zn,Ni)O	0.022		Electrodeposition	90	>300	[42]
(Zn,FeCu)O	0.05		Solid state reaction	900	550	[26]
(Zn,Mn)O		Al_2O_3	Implantation	350	>300	[43]
(Zn,Mn)O	0.1	Al_2O_3	PLD	600	>300	[27]
(Zn,V)O	0.1	Al_2O_3	PLD		>300	[44]
(Zn,Co)O	0.01-0.05	Si	Implantation	350	225-300	[45]
(Zn,Mn)O	0.03	Al_2O_3	PLD	400-600	>300	[46]
(Zn,Mn)O	0.3	Al_2O_3	MBE	400-600	45	[28]
(Zn,Mn)O	0.2		chemical synthesis	145	>300	[47]
(Zn,Co)O	<0.25	Al_2O_3	sol-gel method		>350	[48]
(Zn,Co)O	0.04	bulk	solid-state reaction	900	>300	[49]
(Zn,Ni)O	0.01-0.07	Si	PLD	25	>300	[50]
(Zn,Cr)O	0.03	bulk	Implantation	350	>300	[51]
(Zn,Fe)O	0.03	bulk	Implantation	350	>300	[51]
(Zn,Mn)O	0.03	bulk	Implantation	350	250	[52]
(Zn,Co)O	0.03	bulk	Implantation	350	250	[52]
(Zn,Co)O	0.35	Al_2O_3	MOCVD	300-650	350	[53]
(Zn,TM)O	0.05	Al_2O_3	PLD	600	>300	[54]
(Zn,Co)O			Wet chemical method		>300	[55]

netic semiconductors, bulk $Zn_{1-x}Fe_xO$ codoped with Cu, and the Curie temperature is as high as 550 K [26]. Sharma *et al.* reported ferromagnetism in bulk pellets, thin films, and powder form of $Zn_{1-x}Mn_xO$ with $x < 4\%$ and the Curie temperature is well above 425 K. Table 2.2 lists the recent reports on the magnetic properties of transition metal doped ZnO by various methods. However in these reports the magnetic properties of the same dopant are largely scattered. *E.g.* the saturation moment and Curie temperature for Mn doped ZnO are ranged from $0.075\mu_B$/Mn, 400 K [27] to $0.17\mu_B$/Mn, 30-45 K [28], respectively. In contrast to these reports, other groups reported the observations of antiferromagnetism [29, 30, 31], spin-glass behavior [32, 33], and paramagnetism [34, 30, 35, 36] in TM-doped ZnO, or some extrinsic reasons to contribute to the measured ferromagnetism [37, 38, 39]. These controversial results cast considerable doubt on the magnetism of TM-doped ZnO. Recently several review papers also critically examined the origin of the observed ferromagnetism in recent DMS materials [13, 14].

At the end of this section, Table 2.3 gives a comparison of these different ferromagnetic semiconductors.

2.2 Phase separation in DMS

As already stated in the former section 2.1, in order to establish the ferromagnetism in DMS materials, a sufficiently high concentration of TM atoms, around 10^{20} cm^{-3} (few percents) of the overall atomic density has to be incorporated into host semiconductor. How-

Table 2.3: Comparison of different ferromagnetic semiconductors.

FS or DMS	Properties and research status
Rare-earth chalcogenides	(1) Ferromagnetic and semiconducting (2) Rather low Curie temperature, 70 K for GdN [17]
$Cd_{1-x}Mn_xSe$, $Hg_{1-x}Mn_xTe$, etc.	(1) Mostly antiferromagnetic, or a few Kelvin ferromagnetic (2) Easy to grow epitaxial thin film
GaMnAs, InMnAs, etc.	(1) Carrier mediated ferromagnetism (2) High reproducibility (3) Perfect compatible with conventional electronic device (4) Electric controllable devices (spin-LED, spin-FET) have been demonstrated (5) Curie temperature still far below room temperature
TM:ZnO, TiO_2, etc.	(1) Compatible with conventional electronics (2) Curie temperature well above RT (3) Origin of the ferromagnetism is very controversial (4) Low reproducibility (5) No spin-based device has been demonstrated

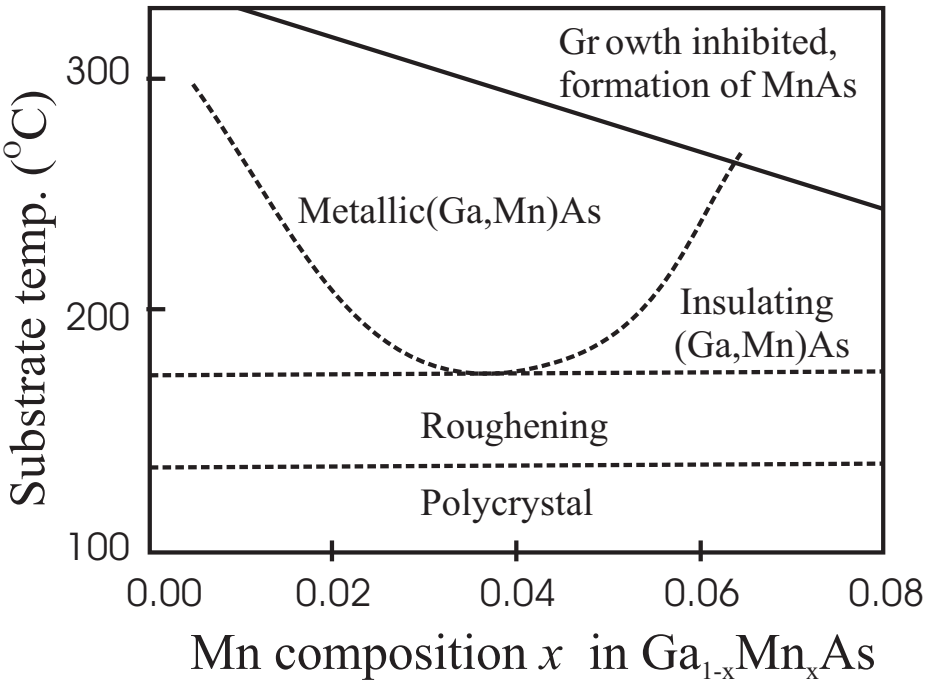

Figure 2.4: Schematic diagram of properties of (Ga,Mn)As films in relation to the growth parameters. Lines provide a rough guide [56].

Table 2.4: Second phases observed in TM-doped ZnO and their magnetic properties. Curie temperature (for ferro- or ferrimagnetic material) of these secondary phases in bulk form is given.

Secondary phase	Magnetism	Curie temperature	Reference
Fe	Ferromagnetic	800 K	[71], this thesis
$ZnFe_2O_4$ (inverted spinel)	Ferrimagnetic		[72, 73], this thesis
Co	Ferromagnetic	1373 K	[74, 75], this thesis
Ni	Ferromagnetic	630 K	[76] this thesis
$(Zn,Mn)Mn_2O_4$	Ferrimagnetic	40 K	[77]
Mn_3O_4	Ferromagnetic	43 K	[78]
$Mn_{2-x}Zn_xO_{3-\delta}$	Ferromagnetic	980 K	[78]

ever, TM impurities have very low solubility limits in semiconductors, rarely exceeding a few percent [57]. Phase separation happens when the concentration of the magnetic constituent is larger than the solubility limit. One is precipitation of a magnetic element or a magnetic compound. Another is spinodal decomposition into regions with low and high concentrations. In spinodal decomposition the fluctuations in composition are relatively small, and are different from nucleation that usually results in large fluctuations of composition and crystalline secondary phases. Phase separation has been well investigated in (Ga,Mn)As and (In, Mn)As materials [56]. Figure 2.4 shows the growth diagram by MBE of (Ga,Mn)As films. There is only a very narrow window, low temperature (below 300 °C) and low Mn concentration, to form high crystalline quality homogenous (Ga,Mn)As films. α-MnAs is a ferromagnetic phase with NiAs-type hexagonal structure and a Curie temperature of 318 K [58]. Moreover in the MBE-grown homogenous GaMnAs, a moderate post-annealing at about 650 °C also leads to ferromagnetic heterogeneous MnAs-rich GaAs layers [59]. In addition to MBE growth, ion implantation is another non-equilibrium fabrication method. By Mn ion implantation into GaAs and a subsequent annealing, ferromagnetic MnGa [60, 61] or MnAs [58] nanoparticles are also formed. Ferromagnetic MnAs precipitates epitaxially embedded inside GaAs matrix also show promising magneto-transport properties [62, 63, 64, 65, 66, 67, 68]. Theoretical calculation on phase separation in GaMnAs and GaMnN has been recently performed by Sato and Katayama-Yoshida [69, 70]. An attractive interaction between Mn impurities has been found, and Mn-Mn attraction in (Ga,Mn)N is one order of magnitude larger than that in (Ga,Mn)As. Therefore, phase separation in TM doped wide bandgap semiconductors is highly expected.

Table 2.4 lists some ferromagnetic (or ferrimagnetic) second phase precipitates reported in TM-doped ZnO. Concerning the phase separation in TM (TM=Fe, Co, and Ni) doped ZnO single crystals, this thesis will answer the following questions.

1. How does the formation of metallic TM nanocrystals depend on the concentration and on the implantation and annealing temperature?

2. How many percent of implanted TM ions are formed in metallic states, and in ionic

states (could be diluted into ZnO matrix)?

3. What are the magnetic properties of the metallic TM nanocrystals, and of the dispersed TM ions?

4. How do these TM nanocrystals orient inside host matrix?

2.3 Magnetic nanoparticles

For magnetic nanoparticles, a critical size may be reached, below which the formation of magnetic domains becomes energetically unfavorable. The size of the single-domain particle depends on the material, *i.e.* its anisotropy energy. The critical diameter d_c below which a particle acts as a single domain particle is given by

$$d_c \approx 18\frac{\sqrt{AK_{eff}}}{\mu_0 M^2} \tag{2.1}$$

where A is the exchange constant, K_{eff} the effective anisotropy energy density, and M the saturation magnetization [79]. The critical diameter is 15 nm for Fe and 35 nm for Co [79].

The magnetism of a single nanoparticle in a solid matrix follows the Néel process [80]. If the particle size is sufficiently small, above a particular temperature (so-called blocking temperature of T_B) thermal fluctuations dominate and the particle can spontaneously switch its magnetization from one easy axis to another. Such a system of superparamagnetic particles does not show hysteresis in the M-H curves above T_B; therefore the coercivity (H_C) and the remanence (M_R) are zero. Below the blocking temperature, the particle magnetic moment is blocked and its magnetization depends on its magnetic history. Phenomenologically there are two characteristic features in the temperature dependent magnetization of a nanoparticle system. One is the irreversibility of the magnetization under a small applied field (*e.g.* 50 Oe) after zero field cooling and field cooling (ZFC/FC) [80]. The other is the drastic drop of the coercivity and the remanence at a temperature close to or above T_B [81][82]. To measure the ZFC/FC magnetization curve [83], the sample is first cooled in zero field from above room temperature to 5 K. Then a small field (*e.g.* 50 Oe) is applied, the ZFC curve is measured with increasing temperature from 5 to 300 (or 350) K, after which the FC curve is measured in the same field from 300 (or 350) to 5 K with decreasing the temperature.

For a dc magnetization measurement in a small magnetic field by SQUID, the blocking temperatue T_B is given by

$$T_{B,Squid} \approx \frac{K_{eff}V}{30k_B} \tag{2.2}$$

where $K_{eff}(V)$ is the anisotropy energy density, V the particle volume, and k_B the Boltzmann constant [80]. With this equation, one can estimate the particle size [82]. However, as found in this thesis, the values from Eq.2.2 are normally much larger than that from XRD data.

Given the large size distribution in a practical magnetic nanoparticle system, T_B is overestimated by taking the temperature at the maximum of the ZFC curve [79]. This explains the overestimation of the average particle size.

In any fine particle system, there is a distribution of particle sizes, which is usually assumed as a log-normal distribution.

$$D(V) = \frac{A}{\sqrt{2\pi}\sigma_L V} exp[-\frac{[ln(V/V_{mean})]^2}{2{\sigma_L}^2}] \tag{2.3}$$

where V_{mean} is the most probable value, and σ_L is the standard deviation.

Such a volume distribution results in a distribution of blocking temperature $T_B(V)$. The ZFC/FC magnetization can be calculated as following.

$$M_{ZFC}(B,T) = \frac{{M_s}^2(T)B}{3kT}\frac{1}{norm}\int_0^{V_{limit}(T)} V^2 D(V)dV + \frac{{M_s}^2(T)B}{3K_{eff}}\frac{1}{norm}\int_{V_{limit}(T)}^{\infty} VD(V)dV \tag{2.4}$$

$$M_{FC}(B,T) = \frac{{M_s}^2(T)B}{3kT}\frac{1}{norm}\int_0^{V_{limit}(T)} V^2 D(V)dV + \frac{30{M_s}^2(T)B}{3K_{eff}}\frac{1}{norm}\int_{V_{limit}(T)}^{\infty} VD(V)dV \tag{2.5}$$

where M_s is the spontaneous magnetization of the particle, $D(V)$ the volume distribution, and $V_{limit}(T)$ ($= 30k_BT/K_{eff}$) the maximum volume in the superparamagnetic state. M_s is assumed to be a constant independent of temperature [79, 80]. The first integral represents the contribution of the superparamagnetic particles, while the second corresponds to the blocked ones. Figure 2.5(a) shows the ZFC/FC magnetization for a system consisting of Fe nanoparticles. The average size is 10 nm and the standard deviation is 0.1. Figure 2.5 (b) compares the ZFC magnetization with the same average size but with different standard deviations. One can see the maximum is largely shifted to higher temperature for a larger deviation.

A more precise determination on the size should be performed by fitting the ZFC curve with the equation 2.4. However for the fitting according to Eq. 2.4, one has to note that M_s and $K_{eff}(V)$ are assumed to be temperature independent, and the interaction between the nanoparticles is ignored. These contributions increase the uncertainty of the extracted values [84]. Nevertheless, using both techniques (XRD, and ZFC magnetization), we can determine the size of nanoparticles and its distribution.

Obviously one question is whether one can judge the ferromagnetic origin from the temperature dependence of ZFC/FC magnetization. At least, a system of DMS nanoparticles, *e.g.* nanostructured Mn-doped InP [85], behaves exactly the same as normal magnetic nanoparticles.

Kuroda *et al.* [86], found nanoscale Cr-rich metallic ferromagnetic regions within a Cr-poor semiconductor lattice of (Zn,Cr)Te (Figure 2.6(a)). The Cr-rich regions have the same crystalline phase as the host crystal lattice. This is so a called spinodal decomposition.

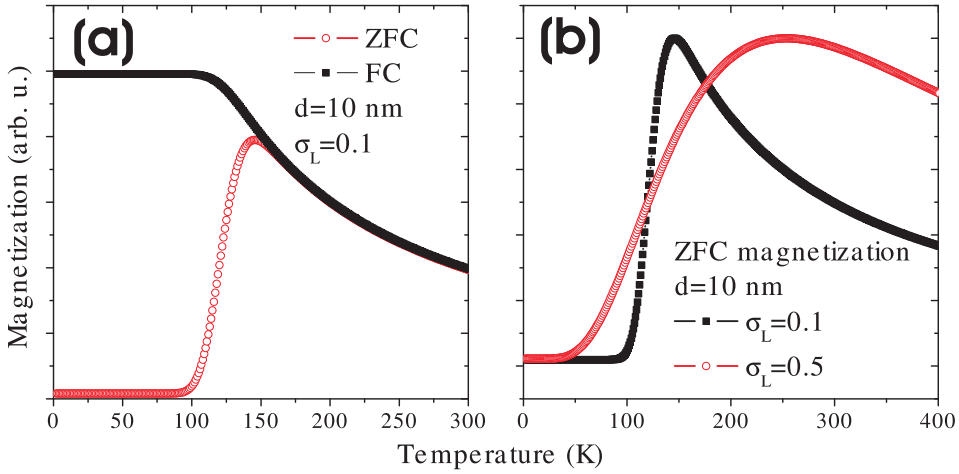

Figure 2.5: (a) Calculated ZFC/FC magnetization for Fe nanoparticles. The average size is 10 nm and the standard deviation is 0.1; (b) ZFC magnetization with the same average size but with different standard deviations.

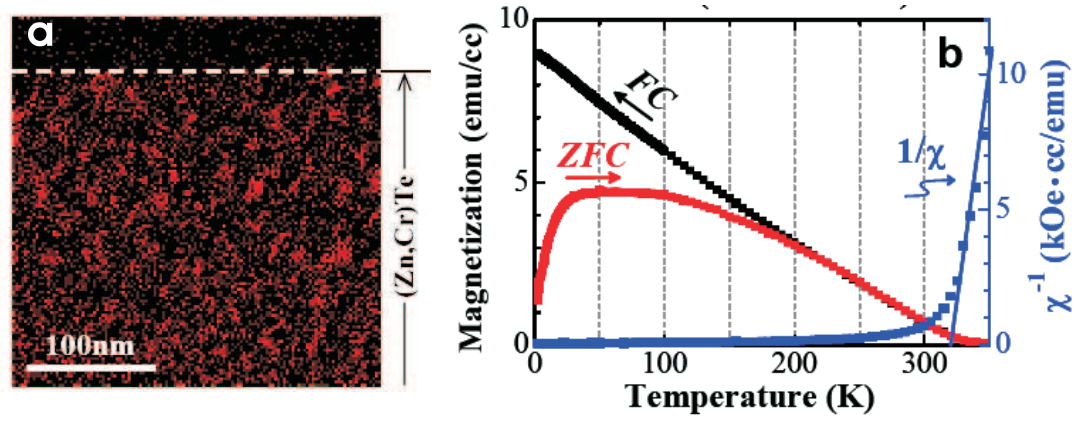

Figure 2.6: (a) Cr distribution probed in a thinner section of $Zn_{0.95}Cr_{0.05}Te$:I film. The Cr-rich regions (brighter spots) are in the size of 10 $\sim$ 20 nm. (b) ZFC/FC magnetization curves for the sample sample. Ref. [86]

Such a system also follows superparamagnetic theory. Therefore the ZFC/FC magnetization curves show similar shapes as the nanoscale secondary phase (Figure 2.6(b)). Spinodal decomposition was also observed in Mn doped Ge [87].

Shinde *et al.* investigated the ZFC magnetization of Co nanoclusters in TiO_2. They found that the maximum of the ZFC curve progressively shifts to a lower temperature with increasing magnetic field. This is due to the fact that a higher magnetic field can switch (deblock) the same sized Co nanocluster already in a lower temperature. This feature could be taken as a criteria to distinguish between superparamangetism and spin-glass.

Moreover, Roshko *et al.* used the Preisach model in order to calculate the ZFC/FC magnetization for a conventional ferromagnet [88]. The thermal fluctuation energy in a ferromagnet is very small so that blocking and activation only occur very close to Curie temperature (T_C). They found that ZFC/FC curves have similar shape as that of a superparamagnetic nanoparticle system, but with a maximum in ZFC curve just below T_C.

Additionally some frustrated systems, *e.g.* a spin glass, also show slow dynamical behavior, which results in the irreversibility of the magnetization after zero field cooling and field cooling [89].

Therefore, it is impossible to unambiguously judge the magnetic origin, *i.e.* secondary phase, spinodal-decomposition, nano-DMS, and spin-glass, by ZFC/FC magnetization measurement alone. For this purpose one has to correlate the structural and magnetic properties.

2.4 Granular magnetic semiconductors

In this thesis, the system of ferromagnetic nanoparticles embedded in semiconductors will be referred as GMS. A straightforward question would be whether GMS has any potential in spintronics application, which requires the interaction between ferromagnetic inclusions and free carriers in semiconductors.

Actually such coupling has been observed between TM thin films separated by a nonmagnetic metal layer. Depending on the thickness of the layers the magnetic films couple ferromagnetically or antiferromagnetically [90]. The coupling mechanism, *i.e.* RKKY interaction, leads to an oscillating polarization of the charge carriers as a function of distance.

Therefore in GMS, an interaction between nanoparticles and free carriers in the host semiconductors, is also expected. For instance, anomalous Hall effect, and giant magnetoresistance have been observed in the GMS systems of MnAs precipitates embedded inside GaAs matrix [63, 64, 65, 67], Fe nanoclusters inside ZnS [91], Co nanoclusters inside TiO_2 [82], and GeMn nanocolumns in Ge [92]. Therefore one would expect that ferromagnetic clusters can actually be used to tailor desirable spintronic functionality [93]. In this thesis, the magnetic and structural properties of ferromagnetic nanocrystals inside ZnO are carefully correlated. To measure the magneto-transport properties of ferromagnetic nanocrystals inside ZnO would be a future work.

Chapter 3

Experimental Methods

3.1 Ion Implantation

3.1.1 Advantages of ion implantation

Ion implantation is a common technique to incorporate foreign ions into a host material. This technique has been integrated into the standard microelectronics production line for integrated circuits in silicon technology. Implantation has a number of advantages:

- Speed, homogeneity and reproducibility of the doping process.
- Exact control of the implantation fluence by integration of the beam current.
- Isotopically selectively ion beams due to mass separation, *e.g.* ^{57}Fe.
- Possibility to exceed the solubility limit by operating far from thermal equilibrium.
- Simple masking methods to make lateral patterns for devices.

Ion implantation is particular useful to introduce enough transition metal ions into semiconductors. The low solubility of transition metal ions such as Mn in compound semiconductors presents an obstacle to obtaining high T_c ferromagnetism, since the strength of the magnetism is proportional to the number of transition metal ions substituted on the cation sites of the column III sublattice [11]. Hebard *et al.* gave a nice review on the works using ion implantation to fabricate diluted magnetic semiconductors based on GaN, AlN, GaP, and SiC [94]. However the main drawback of ion implantation is the damage of the host matrix. In order to repair the lattice damage, high-temperature annealing is normally required.

3.1.2 Interaction between energetic ions and solids

The ion implanted into a semiconductor undergoes collisions with the target atoms, and loses energy due to the ion stopping process. The total energy loss per unit distance is determined by the electronic stopping and the nuclear stopping. In the former process, the ion

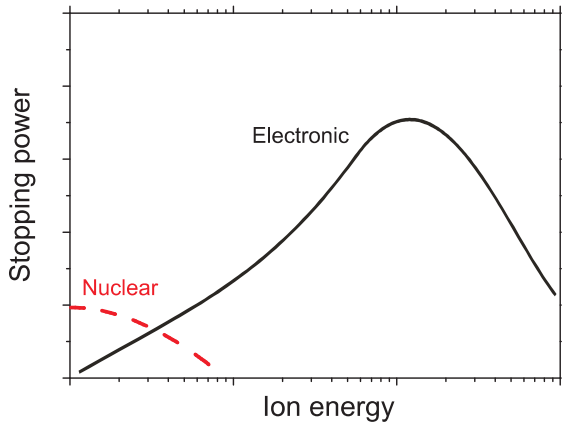

Figure 3.1: Schematic of the cross section for electronic and nuclear stopping processes as a function of ion energy.

energy is lost by excitation and ionization of atoms (inelastic). The lost energy eventually dissipates as heat, and does not create atomic displacements in the materials. The electronic stopping cross section is proportional to the velocity of the implanted ion and therefore to the square root of its energy. Its contribution dominates in the high-energy regime. Nuclear stopping occurs as a result of elastic collisions of ions with nuclei in the solid, and leads to atomic displacements. These displaced atoms may have enough energy to displace others, resulting in a cascade of recoiled atoms. Nuclear energy loss dominates at intermediate energies (hundreds of keV), and leads to the creation of deep-level compensating defects. At high energies, the contribution from this process tends to be small because fast ions have only a short time to interact with a target nucleus, and cannot transfer energy efficiently. Figure 3.1 shows a schematic of the relative energy loss due to electronic and nuclear stopping processes as a function of ion energy.

In this thesis, transition metal ions were implanted into ZnO. These heavy ions undergo a relatively higher degree of nuclear stopping, displacing target atoms right from the surface inwards, producing collision cascades, leading to considerable lattice damage.

Both the stopping effects produce an energy loss rate of some tens of eV per angstrom. The total value of dE/dx is roughly constant for many ions over the ranges of energies of interest for implantation. The projected range R_p is proportional to the initial incident ion energy. With an amorphous target material, the ion profile follows purely Gaussian stopping distribution, which is related to the projected range R_p, standard deviation ΔR_p (straggling) and implant fluence Φ:

$$N(x) = \frac{\phi}{\sqrt{2\pi}\Delta R_p} \exp[-\frac{(x - R_p)^2}{2(\Delta R_p)^2}] \tag{3.1}$$

The peak concentration

$$N_p = \frac{\phi}{\sqrt{2\pi}\Delta R_p} \tag{3.2}$$

occurs at R_p, and

$$N(R_p \pm \Delta R_p) = \frac{N_p}{\sqrt{e}} \tag{3.3}$$

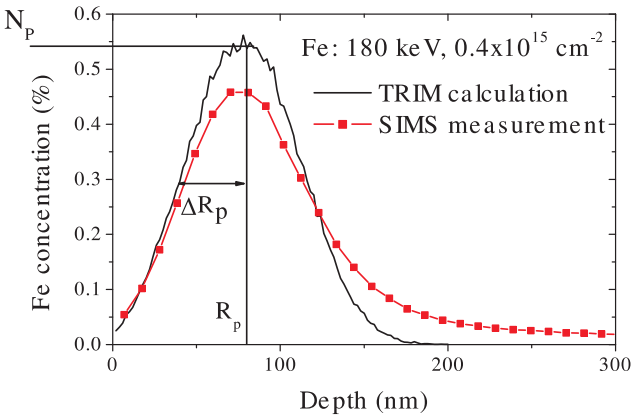

Figure 3.2: Comparison the depth profiles of Fe in ZnO calculated by TRIM and measured by SIMS. The ion distribution exhibits a Gaussian shape with a maximum at a depth of R_p = 80 nm, a straggling of ΔR_p=30 nm and a peak concentration of N_p∼0.5%.

. These parameters are illustrated in Figure 3.2.

The parameters of R_p and N_p can be obtained by computer simulation. TRIM (the Transport of Ions in Matter) is the most comprehensive program available. This is a Monte Carlo program developed by J.F. Ziegler and J.P. Biersack [95], which will calculate both the total three dimensional distribution of the ions and also all kinetic phenomena associated with the ion's energy loss: target damage, sputtering, ionization, and phonon production. An example is given in Figure 3.2. One can see that both the profile shape and the concentration are in a good agreement. The calculation is reliable as confirmed by secondary ion mass spectroscopy (SIMS).

In this thesis, the main implantation work was done on a Danfysik implanter, with an energy range from 80 keV to 180 keV and with temperatures from 240 K to 623 K. The samples were tilted by 7° from normal to minimize the channeling effect.

3.2 X-ray diffraction

3.2.1 Basics of X-ray diffraction

Since the wavelength of x-rays (0.5-2.5 Å) is of the same order of magnitude as the interatomic distances in solids, X-rays are frequently used to study the crystalline structure of materials. When x-ray photons interact with electrons, some photons from the incident beam will be deflected away from their original direction and may interfere with each other (Figure 3.3). The conditions for constructive interference given by the Bragg law:

$$n\lambda = 2d_{hkl}\sin\theta. \tag{3.4}$$

As shown in Fig. 3.3, d_{hkl} is the distance between the lattice planes, λ the X-ray wavelength, θ the angle of the incident light with respect to equidistant hkl lattice-planes, and n the order of diffraction. By varying the angle θ, the Bragg's Law conditions are satisfied by

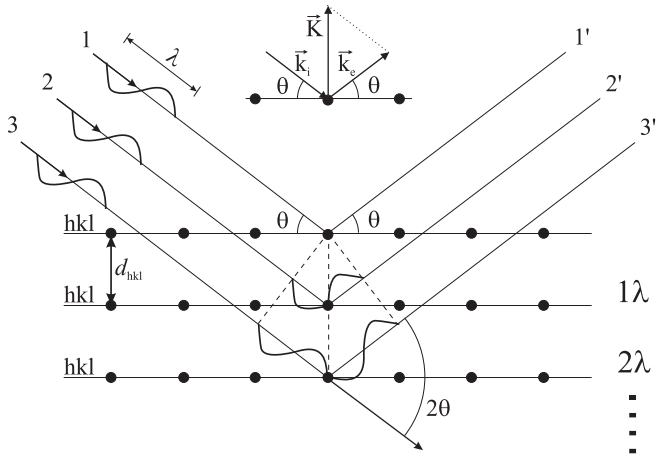

Figure 3.3: Reflection of X-rays from different atomic planes, illustrating Bragg's law. The scattering vector, is defined in the inset.

different d-spacings. Plotting the angular positions and intensities of the resultant diffracted peaks results in XRD pattern, which is characteristic of the sample. Where a mixture of different crystalline phases is present, the resulting diffractogram is formed by addition of the individual patterns.

In the following section, we will describe the type of X-ray diffraction measurements used in this work.

3.2.2 Phase identification: 2θ-θ scan

A 2θ-θ scan allows to determine the interplanar distance d_{hkl}. This interplanar distance is characteristic for a crystal and 2θ-θ scans thus allow the identification of the crystalline phases in a thin film.

In the symmetric 2θ-θ scan, the angle θ of the incoming beam with respect to the sample surface is varied while simultaneously keeping the detector at an angle of 2θ, with respect to the incoming beam (see Fig. 3.3). The scattering vector will always be perpendicular to the sample surface and only the interplanar distances for planes that are parallel to the sample surface can be determined. For a poly-crystalline film, different lattice planes will be parallel to the sample surface and different diffraction peaks will appear. For an epitaxial film, there is only one set of planes parallel to the sample surface and only the peaks for these planes will be observed. Figure 3.4 shows the 2θ-θ scan of Ni implanted ZnO single crystals, where ZnO(0002)(0004) and fcc-Ni(111) peaks appear.

3.2.3 Orientation: ϕ-scan and pole figure

In a 2θ-θ scan only to the planes that are parallel to the surface will be detected. The number of peaks in an experimental 2θ-θ XRD spectrum and their relative intensity give an indication of the texture of the film. However, the complete texture of a thin film is accessible only with pole figure measurements.

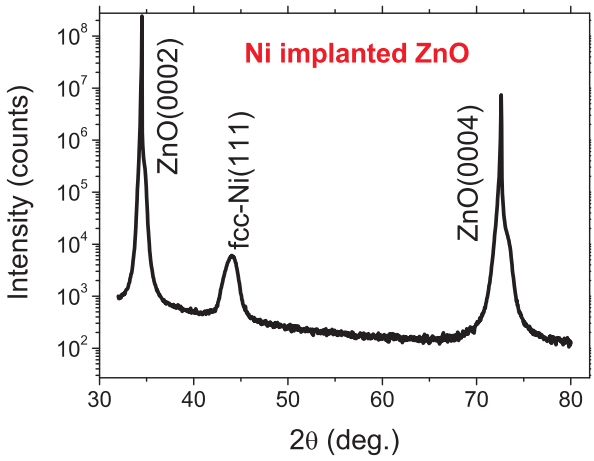

Figure 3.4: 2θ-θ scan of Ni implanted ZnO single crystals.

A pole figure is measured at a fixed scattering angle (constant d spacing) and consists of a series of ϕ-scans (in-plane rotation around the center of the sample) at different tilt or azimuth angles, as described below.

In this kind of measurement, a certain set of hkl-planes is selected. This fixes d_{hkl} in Eq. 3.4, which is achieved by fixing the detector (2θ) and incident beam (θ) angle. Hence, the scattering vector is fixed in space. Diffraction will only occur if the normal to the selected hkl-planes is parallel to the diffraction vector. Therefore, the sample has to be tilted and rotated in space.

For a random orientation of the grains in the thin film, the pole figure will be featureless. No preferred orientation for the normal to the hkl-planes is observed. For epitaxial-like (crystallographically oriented) nanocrystals, the pole figure is characterized by a small, discrete number of spots depending on the crystalline symmetry.

3.2.4 Synchrotron radiation XRD

In recent years synchrotron facilities have become widely used as preferred sources for x-ray diffraction measurements. These powerful sources provide light beams, which are thousands to millions of times more intense than laboratory x-ray tubes.

Obviously the diffraction intensity proportionally depends on the incoming X-ray intensity. In the case of detecting nano-scale phase separation in DMS materials, SR-XRD has its unique advantage. Figure 3.5 shows the comparison of XRD measurements on the Fe-implanted ZnO sample with a synchrotron radiation X-ray source and with a Cu-target x-ray source. The Fe nanocrystals could only be detected by SR-XRD. In this thesis, SR-XRD was performed at ESRF (Grenoble, France), at the Rossendorf Beamline (ROBL), and conventional XRD was performed on a Siemens D5005 diffractometer equipped with a Göbel mirror for enhanced brilliance.

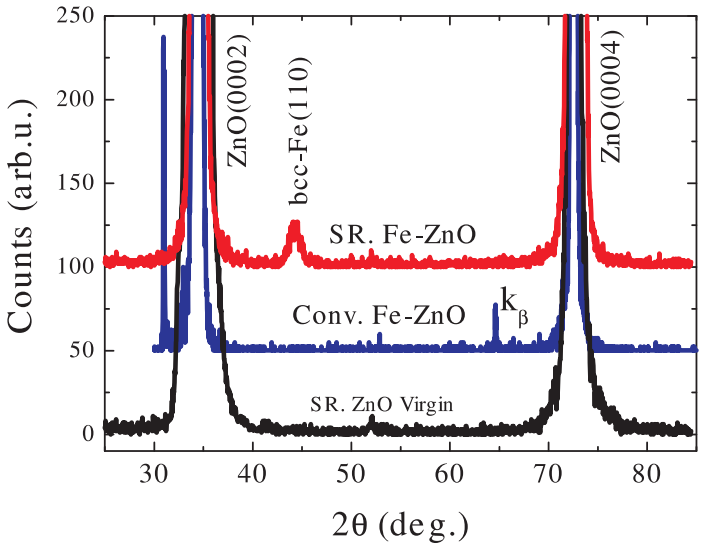

Figure 3.5: Conventional (Conv.) and SR-XRD pattern (θ-2θ scan) for the Fe implanted ZnO. A virgin sample is shown for comparison. Ref. [71].

3.3 SQUID Magnetometry

3.3.1 SQUID Magnetometry

SQUID (superconducting quantum interference device) magnetometry is one of the most sensitive methods to detect magnetic fields. A SQUID sensor consists of two superconductors separated by thin insulating layers to form two parallel Josephson junctions (Figure 3.6(a)).

In a SQUID magnetometry, the magnetic moments are determined by a set of pick-up coils in a so called gradiometer configuration (Figure 3.6(b)). A flux change in the pick-up coils generates a current which is due to the self induction in the loop. This current also generates a flux change in the SQUID sensor connected to the coils.

In order to determine its magnetic moment, the sample is moved along the symmetry axis through the pick-up coils, and the resulting flux changes are recorded (DC-mode). The software fits the observed curve (which has to be symmetric around the coil center) with the expected curve of a dipole.

The SQUID magnetometer used for this thesis is a Quantum Design Magnetic Property Measurement System, XXL MPMS, with temperatures ranging from 1.8 to 400 K, and magnetic fields available up to 70 kOe. Samples are mounted within a plastic straw and connected to one end of a sample rod which is inserted into the dewar/probe. The signal is fitted to an ideal dipole response using a non-linear least-squares routine as shown in Figure 3.7.

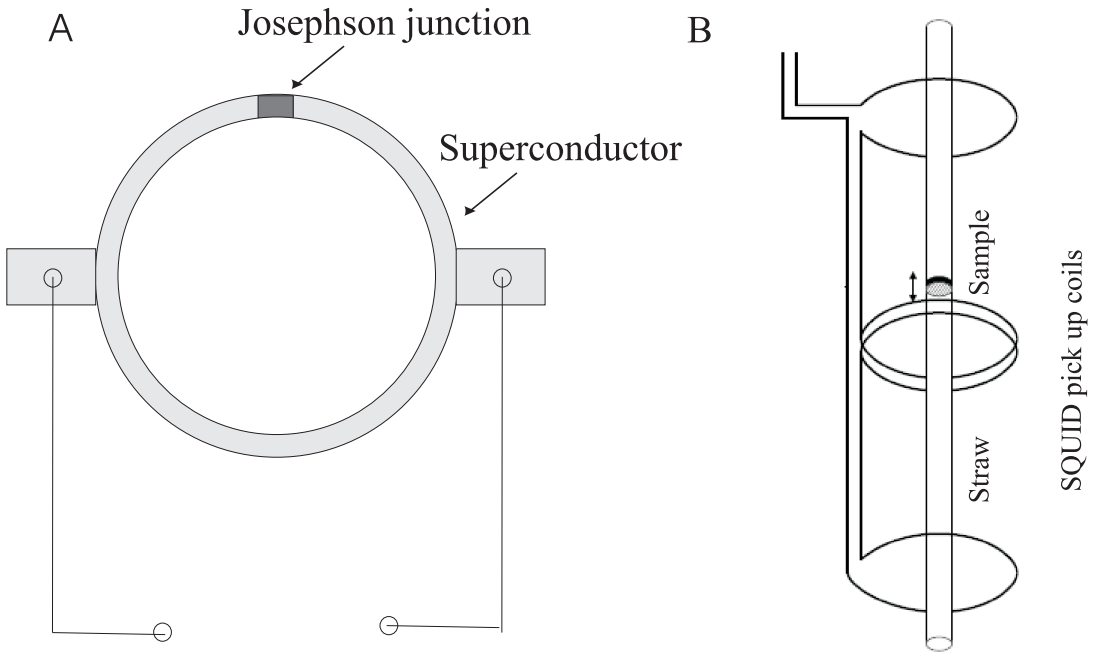

Figure 3.6: (a) A scheme for a SQUID. From ref. [96]. (b) Second-order gradiometer superconducting pick-up coils.

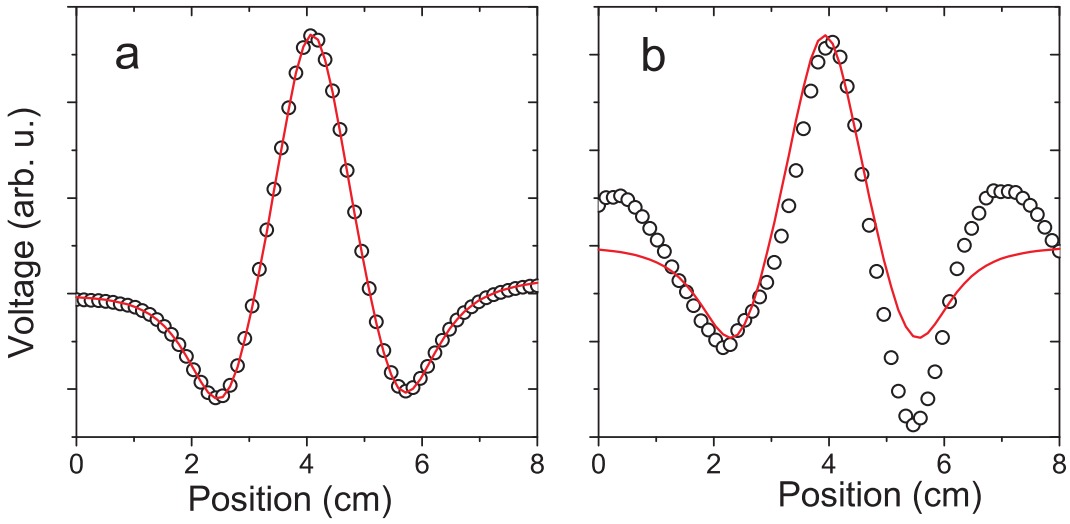

Figure 3.7: SQUID response, (a) a good measurement, and (b) a bad one.

3.3.2 Notes on errors in SQUID measurement

An error in SQUID magnetometer measurement is determined from the fit of the SQUID response (as shown in Figure 3.7). Moreover we found there is a typical mistake in the sample mounting. In the manual book, it is written the maximal size of the sample can be 6 mm (in horizontal direction) and 12 mm (in perpendicular direction). However this limitation works well only when the sample is strongly ferromagnetic, however fails when the magnetism is rather weak. In the latter case, if the sample is too large (*e.g.* >5 mm) in perpendicular direction, the SQUID response can be asymmetric, consequently results in a large error in the fitting or even a wrong fitting. Therefore in this case we always cut the sample to make sure a symmetric SQUID response.

Another typical mistake in SQUID measurement is the use of steel tweezers. Normally, the magnetization displayed by thin-film specimens of what is claimed to be a "ferromagnetic semiconductor" is typically only 10^{-5} emu. Of course, this level of weak magnetization can be easily detected by SQUID. However, careful attention should be paid to the fact that even tiny amounts of iron – as little as 1/2000 of the typical sample volume used in SQUID measurements – can generate these kinds of magnetic signals. A recent report cautioned that nonmagnetic HfO_2 and Si thin films generate clear, ferromagnetic signals after contact with stainless steel tweezers [38]. In this thesis, every sample was cleaned by Isopropanol right before SQUID measurement, and in all the processes the sample was handled by ceramic tweezers.

3.4 RBS/channeling

Rutherford backscattering spectrometry combined with channeling (RBS/C) is a powerful technique to determine the composition, thickness and crystalline quality of thin film materials, as well as the lattice location of impurities in crystals. In this thesis, RBS/C is mainly used to evaluate the lattice disordering of ZnO upon ion implantation, and its recovering after annealing. Therefore, in this section the physical concepts of RBS/channeling will be briefly introduced.

3.4.1 Physical concepts

The experimental setup, shown schematically in Fig. 3.8 (a), consists of a well collimated high energy beam that impinges on a target. The backscattered He projectiles are collected in a surface barrier detector generating an electrical signal proportional to the energy of the scattered particle. A RBS spectrum is the backscattered yield as a function of energy (channel number). From the energy of the particles, the mass of the target atom and its depth in the sample can be deduced. The amount of particles that are detected at a certain energy can be correlated to the concentration of a specific target element. Three physical concepts are important in understanding a backscattering spectrum.

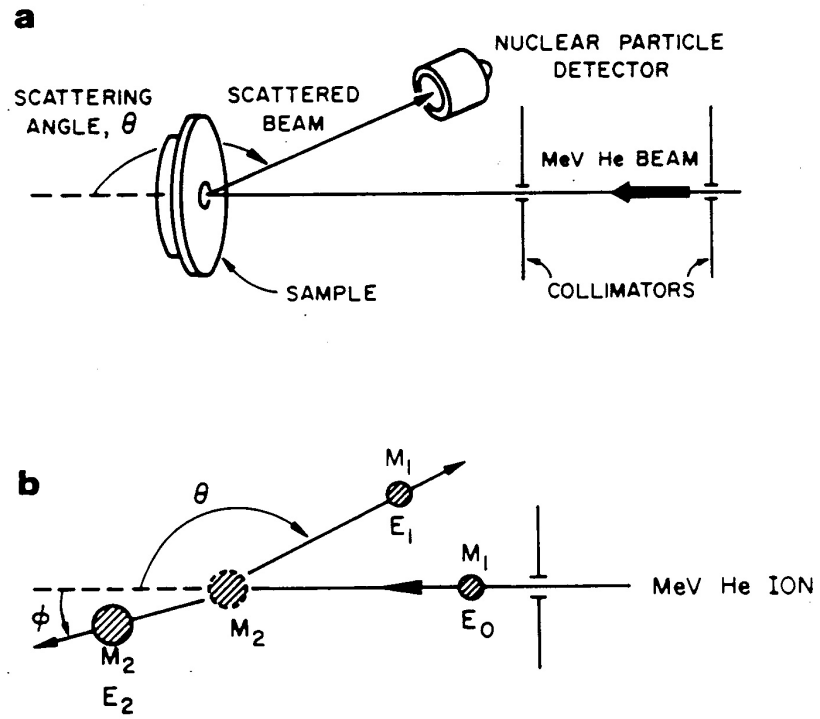

Figure 3.8: (a) Geometry of RBS measurement. (b) The elastic collision between a projectile ion and a target atom [97].

(1) **Kinematic factor** K determines the energy transfer from a projectile to a target nucleus in the two-body collision, as shown in Figure 3.8(b). In this elastic collision, the kinematic factor, the ratio between the projectile energies E_1 and E_0, can be calculated for $M_1 < M_2$ as

$$K = \frac{E_1}{E_0} = \left(\frac{(M_2^2 - M_1^2 \sin^2\theta)^{1/2} + M_1 \cos\theta}{M_1 + M_2} \right)^2 \tag{3.5}$$

where E_0 is the initial energy of the projectile, E_1 the energy of the projectile after collision and θ the detector angle. During an experiment, θ and M_1 are fixed. Therefore, the kinematic factor K only depends on the mass of the target atom M_2.

(2) **Electronic stopping** determines the average energy loss of an atom moving through (inward and outward) the investigated materials due to its colliding with electrons, which allows depth determination.

(3) **Scattering cross section** $\sigma(\theta)$ is proportional to the probability that a particle is backscattered towards a detector at an angle θ. For scattering of two fully stripped nuclei (which is the case in the RBS energy window), the scattering cross section can be approximated by the Rutherford scattering cross section

$$\sigma(\theta) = \left(\frac{Z_1 Z_2 e^2}{4E} \right)^2 \frac{1}{\sin^4(\theta/2)} \tag{3.6}$$

The Z_2^2 dependence of $\sigma(\theta)$ indicates that RBS is significantly more sensitive to high Z elements. Therefore, if equal amounts of a light and heavy element are present, the signal from the heavy element will be much higher.

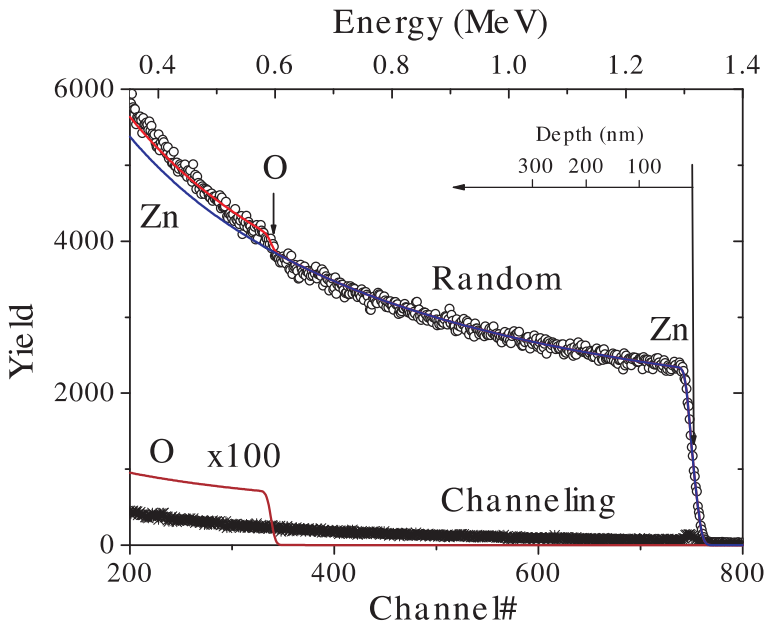

Figure 3.9: RBS/C spectra of a virgin ZnO crystal. The x-axis is the energy of detected backscattered He, and the y-axis is the amount of backscattered He at corresponding energy. The arrows label Zn and O indicate the backscattering energy from surface Zn and O, respectively.

As an example, Figure 3.9 shows the RBS spectrum of a virgin ZnO crystal. The arrows labelled by Zn and O indicate the energy from the Zn and O atoms at the surface, respectively. A depth scale is also indicated in the figure. One can see four features related to the physical factors discussed in the text: (i) the backscattering energy from O is much lower than that from Zn, (ii) the backscattering yield from O is much lower than that from Zn, (iii) due to electronic stopping, the backscattering energy is lower from deeper locations, and (iv) the channeling spectrum is much reduced in yield comparing with random one (explained in following section). One has to be reminded that RBS is only capable of thin film investigation, and the sensitive depth (with He energy of 1-2 MeV) is below 1 μm.

3.4.2 Channeling

The phenomenon of channeling was first predicted theoretically by Lindhard [98]. If the He^+ ions are incident on the crystal along a main crystalline axis (Figure 3.10), the RBS-yield will be much less that that along a random distribution of the target atoms as shown in Figure 3.9. By dividing the channeling and random spectrum, a value for the minimum yield χ_{min} is obtained. This reflects the crystalline quality. For a perfect Si crystal at room temperature, the χ_{min} is approximately 1%.

In this study, RBS/C was mainly used to evaluate the lattice disorder induced by implantation, and its recovering upon thermal annealing. In this thesis RBS/C measurements were performed with a 1.7 MeV $^4He^+$ beam produced by a Van de Graaff tandem accelerator. The samples were mounted on a three-axis goniometer that allows the determination of the channeling directions of the crystals with an accuracy of 0.01°. The detector was positioned

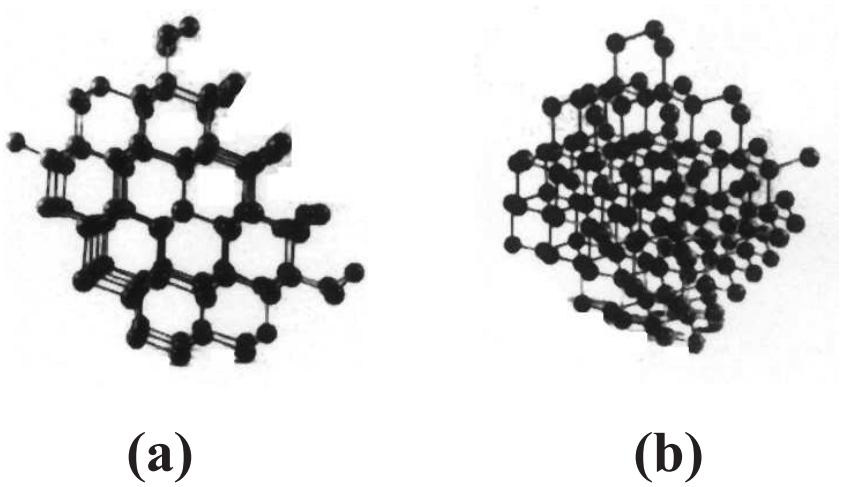

Figure 3.10: Orientation of a crystal with respect to the ion beam for (a) a channeled or (b) random RBS measurement. Imagine that the beam comes along the normal of the paper.

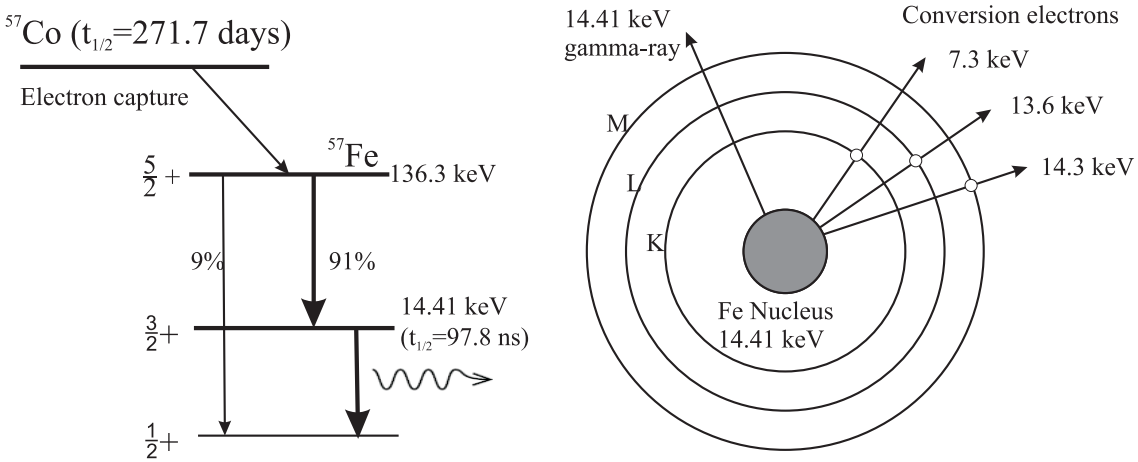

Figure 3.11: Decay scheme for a ^{57}Co source. From the state of 14.41 keV, the nucleus can decay either by gamma-ray emission, or by internal conversion as shown by the right panel.

at a fixed scattering angle of 170°.

3.5 Conversion Electron Mössbauer Spectroscopy

The Mössbauer effect involves resonant absorption of gamma rays by atoms of the same isotope. In our case, the source of the gamma rays is radioactive ^{57}Co, which undergoes a nuclear decay (electron capture) to ^{57}Fe in its I=5/2 excited state. This can decay in two ways as shown by figure 3.11, the main one gives a 14.4 keV excited state. The excited nucleus (I=3/2) can de-excite (i) radiatively by the emission of a gamma ray; (ii) non-Radiatively by internal conversion and the ejection of an atomic electron. Conversion Electron Mössbauer Spectroscopy (CEMS) records the emission of conversion electrons.

The Mössbauer spectrum can be affected by three intrinsic factors:

Isomer shift: resulting from the difference in the electron densities at the nuclear sites in

Table 3.1: Hyperfine parameters for metallic Fe and common Fe-compounds. From ref. [99].

Parameters	α-Fe	γ-Fe	α-Fe_2O_3	γ-Fe_2O_3	Fe_3O_4	$ZnFe_2O_4$
Isomer shift (mm/s)	0	-0.1	0.38	0.22/0.37	0.63/0.27	0.33
Quadrupole splitting (mm/s)	-	-	-0.21	0.08/0.02	0.05/-	0.41
Hyperfine field (T)	33.2	-	52	50.2/50.5	45/48.9	-
Charge state of Fe	0	0	3+	3+	2.5+/3+	3+

the emitting and absorbing atoms. This difference in density changes the Mössbauer transition energy and so the Mössbauer spectrum is shifted. Therefore the isomer shift allows to distinguish different ion charge states.

Quadrupole splitting: Nuclei in states with an angular momentum quantum number I>1/2 have a non-spherical charge distribution. This produces a nuclear quadrupole moment. The presence of an electric field gradient (produced by an asymmetric electronic charge distribution or ligand arrangement) splits the nuclear energy levels.

Magnetic splitting: In the presence of a internal magnetic field the nuclear spin moment experiences a dipolar interaction with the magnetic field *i.e.* Zeeman splitting. This magnetic field splits nuclear levels with a spin of I into (2I+1) sub-states.

These interactions, isomer shift, quadrupole splitting and magnetic splitting, alone or in combination are the primary characteristics of many Mössbauer spectra. Table 3.1 shows the hyperfine parameters for metallic Fe and common Fe-compounds. For a detailed description about Mössbauer Spectroscopy, please refer to the text book [99].

Chapter 4

Fe implanted ZnO: magnetic precipitates versus dilution

In this chapter, a comprehensive investigation of Fe-implanted ZnO single crystals will be presented. Different implantation fluences, temperatures and post-implantation annealing temperatures have been chosen in order to evaluate the structural and magnetic properties over a wide range of parameters. Three different regimes with respect to Fe concentration and process temperature are found: 1) Disperse Fe^{2+} and Fe^{3+} at low Fe concentrations and low processing temperatures, 2) $FeZn_2O_4$ at very high processing temperatures and 3) an intermediate regime with a co-existence of metallic Fe (Fe^0) and ionic Fe (Fe^{2+} and Fe^{3+}). Ferromagnetism is only observed in the latter two cases, where inverted spinel $ZnFe_2O_4$ and α-Fe nanocrystals are the origin of the observed ferromagnetic behavior, respectively. The ionic Fe in the last case could contribute to a carrier mediated coupling. However, the separation between the ions is too large to couple ferromagnetically due to the lack of p-type carriers. For comparison investigations of Fe-implanted epitaxial ZnO thin films are presented.

The chapter is organized as follows. First, all the experimental methods employed will be listed. Then the results will be discussed according to the physical phenomena as follows: lattice damage and recovering, the distribution of implanted Fe, the formation of precipitates (metallic Fe, or Zn-ferrites), the charge state of Fe, the ferromagnetic properties, and the Fe implanted epitaxial ZnO films. In the discussion part, we sketch a phase diagram of Fe in ZnO, and apply a model to explain the Fe nanocrystal aggregation. Moreover the reason for the absence of ferromagnetism in ZnO diluted with ionic Fe is discussed.

This chapter has been published in following papers: (1) Appl. Phys. Lett., **88**, 052508 (2006); (2) J. Phys. D-Appl. Phys., **40**, 964 (2007); and (3) J. Appl. Phys. **103**, 023902 (2008).

4.1 Experiments

Commercial ZnO bulk crystals were implanted with ^{57}Fe ions at temperatures ranging from 253 K to 623 K with fluences from 0.1×10^{16} cm^{-2} to 8×10^{16} cm^{-2}. The implantation energy was 180 keV, which results in a projected range of $R_P = 89 \pm 29$ nm, and a maximum atomic concentration from 0.14% to 11% (TRIM code [95]). For comparison, epitaxial ZnO thin films grown on Al_2O_3 by pulsed laser deposition were implanted with ^{57}Fe at selected implantation parameters (623 K, 4×10^{16} cm^{-2}). Three sample series are investigated and listed in Table 4.1.

For a detailed analysis we applied different techniques.

- Synchrotron radiation x-ray diffraction (SR-XRD) and conventional XRD
- Rutherford backscattering/channeling (RBS/C)
- Secondary ion mass spectrometry (SIMS)
- Conversion electron Mössbauer spectroscopy (CEMS) at room temperature
- SQUID-magnetometry with the magnetic field applied parallel to the sample surface.

In Chapter 3 a rather detailed description on these experimental methods has been given. SIMS was performed by a Riber MIQ-256 system with oxygen primary ions of 6 kV and monitoring positive secondary ions at Universität Gießen. The depth scale was calibrated by measuring the sputtered crater via profilometry. The absolute concentration was determined by calculating the sensitivity factors from the low fluence implants. By SQUID, virgin ZnO is found to be purely diamagnetic with a susceptibility of -2.65$\times 10^{-7}$ emu/Oe·g. This background was subtracted from the magnetic data.

4.2 Results

In this section, we present experimental data on structural and magnetic properties of ^{57}Fe implanted ZnO. Of interest in this study are the ion-implantation induced lattice damage, the distribution of Fe, the formation of metallic Fe nanocrystals, the charge state of Fe, the magnetic properties, and the structure and magnetism evolution upon post annealing. The difference between ZnO bulk crystals and epitaxial films upon Fe implantation is also compared.

4.2.1 Lattice damage accumulation

Fluence dependence

Figure 4.1(a) shows representative RBS/C spectra for different Fe fluences implanted at 623 K. The arrow labelled Zn indicates the energy for backscattering from surface Zn atoms.

Table 4.1: Structural properties of ^{57}Fe-implanted ZnO bulk crystals and epitaxial thin films. The implantation energy is 180 keV.

Fluence (cm^{-2})	Implantation Temp. (K)	Peak Concentration (TRIM)	Peak Concen. (SIMS)	χ_{min} (RBS/C) Bulk	Surface	Metallic Fe Formation
0.1×10^{16}	623	0.14%	0.1%	8.1%	5.9%	No
0.4×10^{16}	623	0.55%	0.46%	38%	14%	No
0.8×10^{16}	623	1.1%	0.89%	43%	16%	No
2×10^{16}	623	2.7%	2.6%	57%	39%	α-Fe
4×10^{16}	623	5.5%	6.0%	60%	32%	α-Fe
8×10^{16}	623	11%	-	65%	55%	α-Fe
0.4×10^{16}	253	0.55%	0.5%	31%	16%	No
4×10^{16}	253	5.5%	5.5%	65%	43%	No
4×10^{16}	298	5.5%	-	65%	40%	No
4×10^{16}	473	5.5%	-	66%	42%	No
4×10^{16}(^{a})	623 K	5.5%	-	44%	-	α and γ-Fe

^{a}ZnO epitaxial thin films.

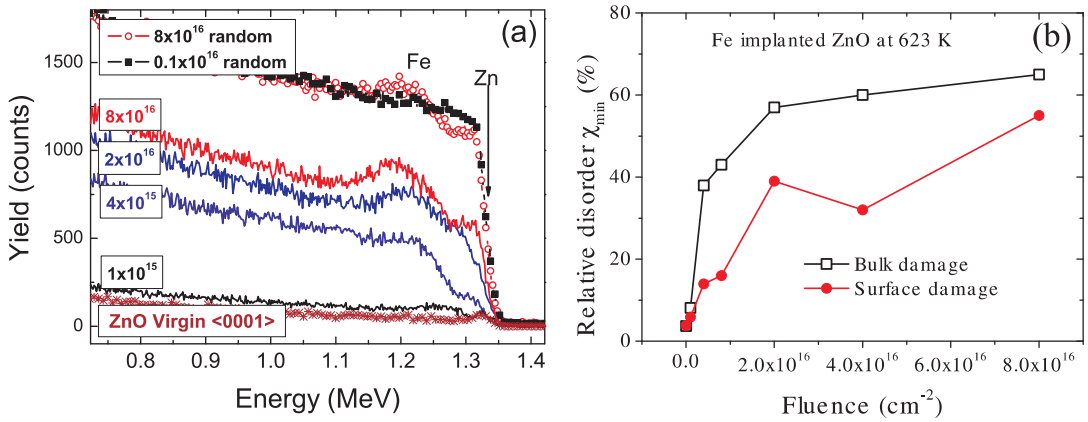

Figure 4.1: (a) Representative RBS random and channeling spectra of Fe implanted ZnO with the implantation energy of 180 keV. The fluence is indicated on the channeling spectra. The dashed line separates the damage regions of surface and bulk, where the number of displaced atoms is maximum. (b) The maximum relative disorder of the Zn lattice (χ_{min}) at different depth (surface and bulk) as a function of ion fluence.

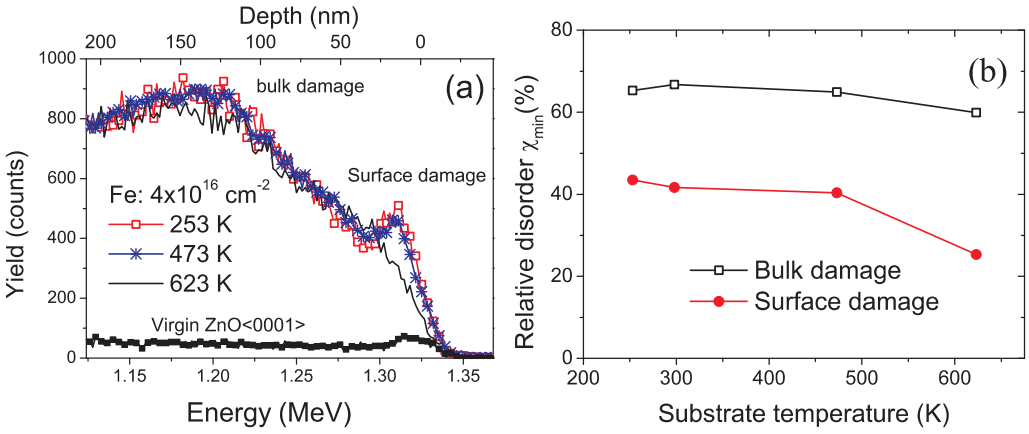

Figure 4.2: (a) Representative RBS/C spectra with different implantation temperature. The fluence is 4×10^{16} cm^{-2}, and implantation energy is 180 keV. (b) The calculated χ_{min} for different implantation temperature. Implantation at low temperature ($\leq$473 K) results in more damage at the surface region.

The implanted Fe ions cannot be detected for the lowest fluence (0.1×10^{16} cm^{-2}). However they are more pronounced as a hump in the random spectrum for a high fluence of 8×10^{16} cm^{-2}. The channeling spectrum of a virgin sample is provided for comparison. The yield increase in the channeling spectra mainly originates from the lattice damage due to implantation. However, in the higher-fluence case, the Fe ions also significantly increase the RBS yield. Two features are observed in the RBS/C spectra. One is the bimodal [100] distribution of maximum damage depths, *i.e.* in the bulk and at the surface, separated by the dashed line in Figure 4.1(a). Similar depth profiles have already been discussed by Kucheyev *et al.* [100]. In the bulk damage region the nuclear energy-loss profile is maximum, which induces a large number of atomic displacements. The surface damage peak is often a sink for ion implantation induced point defects [100].

Another feature is the saturation at larger fluences. χ_{min}, the ratio of the channeling spectrum to the random one, is calculated in both damage regions, as shown in Figure 4.1(b). Above a fluence of 2×10^{16} cm^{-2} both damage peaks saturate. This is due to the strong dynamic annealing effect, *i.e.*, migration and interaction of defects during ion implantation [100]. This strong dynamic annealing also makes ZnO an *irradiation-hard* material, *i.e.*, it still partly remains crystalline after irradiation by Fe ions up to a fluence of 8×10^{16} cm^{-2} (χ_{min} of 68%).

Implantation temperature dependence

In general increasing the substrate temperature during implantation can suppress the lattice damage in semiconductors. However this is not the case for ZnO. Figure 4.2(a) shows the channeling spectra for Fe implanted ZnO at different implantation temperatures. Although the surface damage peak increases drastically with decreasing implantation temperature, the bulk damage peak is hardly effected by implantation temperature. This can be observed clearly in Figure 4.2(b). The point defects induced by the ion-beam can be

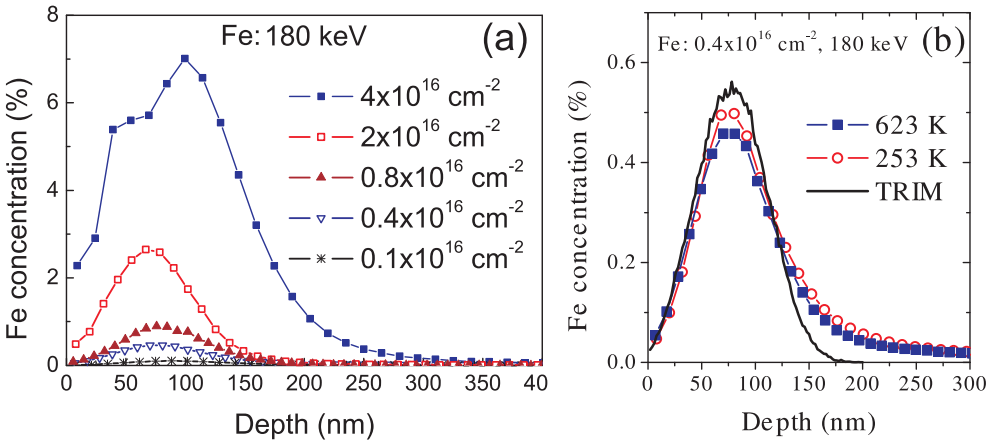

Figure 4.3: (a) Fe distribution in the samples implanted with Fe at 623 K for different fluences measured by SIMS. The ion fluences are indicated in the figure. (b) Distribution of Fe in ZnO implanted at different temperatures. The TRIM [95] simulation is presented for a comparison.

significantly suppressed by increasing the implantation temperature above 623 K. This temperature is very critical, and below 623 K, the surface damage peak also has no dependence on the substrate temperature. This is very important for the electrical doping of ZnO by ion implantation, where point defects are believe to decrease the conductivity [101].

Recovering by post-annealing

As shown above, the bulk damage cannot be suppressed by increasing the implantation temperature. It has to be removed by post annealing at higher temperature. The annealing was performed in high vacuum in order to avoid extrinsically induced oxidation of Fe. The temperature was varied from 823 K to 1073 K. The details have been reported in the Ref. [102]. Both the surface and bulk damage peaks decreased progressively with increasing the annealing temperature and time. However even after annealing at 1073 K for 3.5 hours, there is still considerable amount of damage. This is because of the high melting point of ZnO (∼2250 K). The extended defects can only be removed completely by annealing at approximately two-thirds of the melting temperature [103]. Therefore a high annealing temperature (1500 K) is necessary to completely recover the lattice structure of ZnO. However, high vacuum annealing above 1000 K also leads to decomposition of ZnO [104].

4.2.2 Fe distribution

RBS/C can give an overview of the lattice damage upon Fe implantation. However, since the mass of Fe is smaller than Zn, it is difficult to obtain the depth profile of the implanted Fe. Therefore, SIMS is employed to determine the Fe depth profile (see Figure 4.3(a)). It is observed that the peak concentration of Fe ranges from 0.1% to 7% for difference fluences, with a projected range of R_P=(80-90)±(20-30). This is in rather good agreement with TRIM simulations [95]. The only discrepancy concerns the the high-fluence sample (4×10^{16} cm^{-2}),

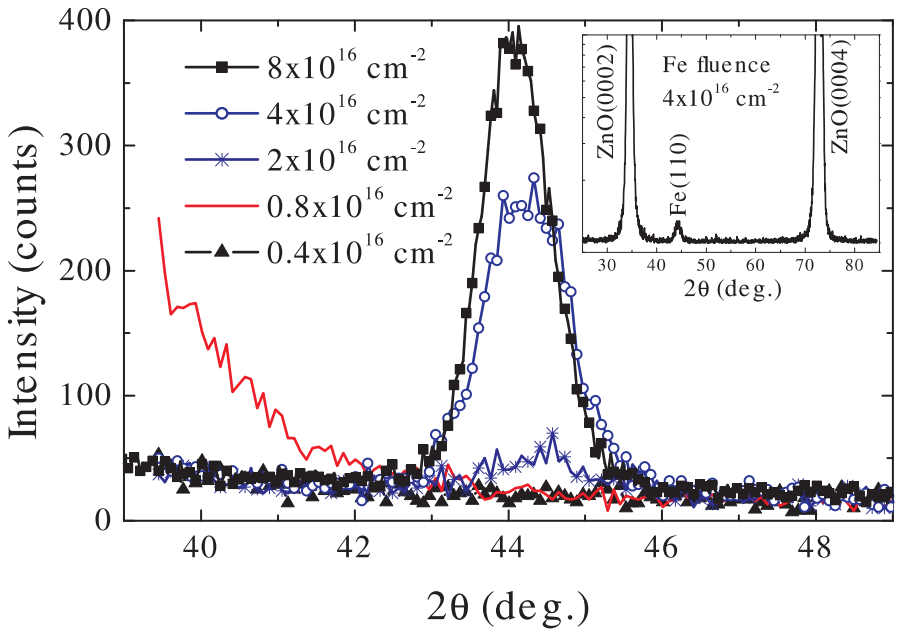

Figure 4.4: SR-XRD 2θ-θ scans of Fe implanted ZnO for different fluences reveal the formation of crystalline Fe nanoparticles when the fluence is above 2×10^{16} cm^{-2}. Inset shows a long-range scan, where Fe(110) is the only peak related to precipitation.

where TRIM simulations predict a peak concentration of 5%. This is due to the change in SIMS sensitivities for different materials, which implies that the determined concentrations are more accurate in the low concentration (below 1%) regime.

In Figure 4.3(b) the Fe depth profile for the fluence of 0.4×10^{16} cm^{-2} is compared for different implantation temperatures. The profile does not change significantly upon increasing the implantation temperature from 253 K to 623 K. The slightly higher concentration for implantation at 253 K is within the fluence error.

As discussed the in Ref. [102], Fe diffuses towards the surface after high temperature annealing. The same diffusion of Fe upon annealing was also observed by SIMS (not shown).

4.2.3 Formation of Fe NCs

By employing SR-XRD, we have systematically investigated the formation of Fe NCs, and its dependence on the fluence and implantation temperature.

Fluence dependence

Figure 4.4 shows the SR-XRD pattern (near the Fe(110) peak) as a function of fluence. At a low fluence (0.1×10^{16} to 0.8×10^{16} cm^{-2}), no crystalline Fe NCs could be detected, while above a fluence of 2×10^{16} cm^{-2}, an Fe(110) peak appears and increases with fluence. The inset shows a wide-range scan for the high-fluence sample (4×10^{16} cm^{-2}). No other Fe-oxide (Fe_2O_3, Fe_3O_4, and $ZnFe_2O_4$) particles are detected in the as-implanted state. The full width at half maximum (FWHM) of the Fe(110) peak decreases with increasing fluence,

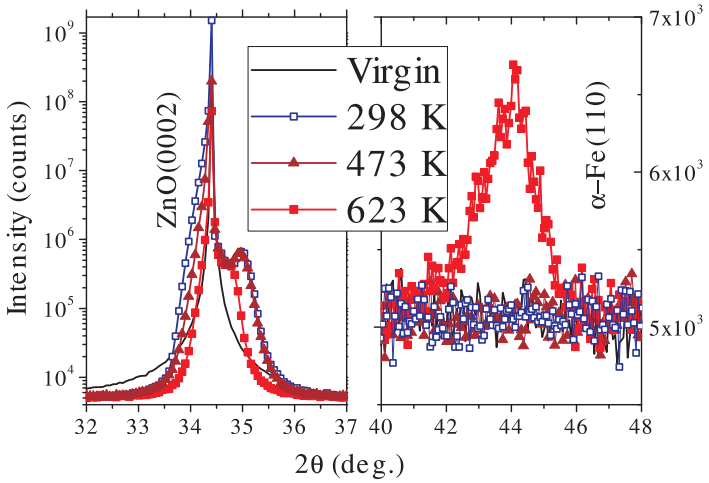

Figure 4.5: SR-XRD 2θ-θ scans of Fe implanted ZnO with the same fluence of 4×10^{16} cm^{-2} at difference temperature. In order to show the Fe(110) peak, the figure is spliced to two parts: left panel for ZnO(0002) and right panel for Fe(110). Only the sample implanted at 623 K shows α-Fe precipitates.

indicating a growth of the average diameter of these NCs. The crystallite size is calculated using the Scherrer formula [105],

$$d = 0.9\lambda/(\beta \cdot \cos\theta), \tag{4.1}$$

where λ is the wavelength of the x-ray, θ the Bragg angle, and β the FWHM of 2θ in radians. The crystallite size is listed in table 4.3.

Note that only one peak of Fe(110) appears in the inset of Figure 4.4. This indicates a texture of the Fe NCs. However no texture behavior is found even for the highest-fluence sample in pole figure measurements on Fe(110) and Fe(200) (not shown). This could be due to the difference in the crystalline symmetry of hexagonal ZnO (six fold symmetry) and bcc-Fe (four fold symmetry). For a bcc-crystal, one cannot find a six-fold symmetry viewed from any direction. In contrast, hcp-Co(0001) and fcc-Ni(111) NCs, which are six-fold symmetric, are found to be crystallographically oriented inside ZnO matrix. This highly ordered orientation allows them to be detected even by laboratory XRD [76, 106].

Implantation temperature dependence

SR-XRD was also performed for the samples with an Fe fluence of 4×10^{16} cm^{-2} implanted at different temperatures from 253 K to 623 K. As shown in Figure 4.5, for implantation temperatures of 473 K and below, no crystalline Fe could be detected. This is also confirmed by the CEMS results (shown later), where the Fe^0 state appears only at an implantation temperature of 623 K. Note the asymmetry of the ZnO(0002) diffraction peaks in Figure 4.5. A shoulder on the right side (smaller lattice constant) is clearly observed. This shoulder decreases with increasing implantation temperature, and can therefore be associated with lattice damage or ZnO substituted with Fe. In view of a detailed study of ion implantation into GaN where the implantation induces a lattice expansion of GaN (a

shoulder at left side) [107, 108], we rather attribute the observed right side shoulders to ZnO substituted with Fe. In the 623 K implantation, metallic Fe NCs start to form, therefore the substitution is reduced.

Growth with post-annealing

After thermal annealing at 823 K for 15 min, more α-Fe NCs of a larger size are formed for the samples implanted at 623 K. After 1073 K and 15 min annealing, the α-Fe almost disappears and $ZnFe_2O_4$ starts to form. The details of the structure and magnetism evolution upon thermal annealing can be found in Ref. [102].

4.2.4 Charge state of Fe

CEMS allows one to identify different site occupations, charge and magnetic states of ^{57}Fe. The hyperfine parameters calculated according to the evaluations of the spectra are given in Table 4.2. All isomer shifts are given relative to an α-Fe reference foil. In general, the implanted Fe occupy three different states: metallic Fe, Fe^{2+} and Fe^{3+} ions dispersed in the ZnO matrix and finally Fe^{3+} in Zn-ferrites. The hyperfine interaction parameters obtained from the best fits are different from that of ferromagnetic α-Fe_2O_3 or γ-Fe_2O_3 or ferrimagnetic Fe_3O_4 (see Table 3.1). Hence, the presence of these phases was excluded. The dispersed ionic Fe could substitute onto Zn site.

Fluence dependence

Figure 4.6(a) and (b) show the comparison of Fe implanted ZnO at 623 K with a fluence of 0.4×10^{16} and 4×10^{16} cm^{-2}, respectively. In spectrum (a), the singlet S and doublet D(I) are attributed to Fe^{3+}, while the doublet D(II) is from Fe^{2+}. In the high fluence sample (spectrum (b)), the majority of Fe are ionic states Fe^{3+} (singlet S) and Fe^{2+} (doublet D(I) and D(II)), while a considerable fraction of a sextet associated to α-Fe is present (sextet M). The formation of α-Fe is in agreement with SR-XRD observation (Figure 4.4). At room temperature, all Fe^{2+} and Fe^{3+} show no ferromagnetic interaction. Later on in subsection 4.2.5, we show that even at 5 K the measured ferromagnetism can only be attributed to α-Fe NCs.

Implantation temperature dependence

Figure 4.7(a) and (b) shows CEMS for the samples implanted at low temperatures, 473 K and 253 K, respectively, with a ^{57}Fe fluence of 4×10^{16} cm^{-2}. In these two samples, ionic Fe are the dominant charge states: Fe^{3+} (S and D(I)), and Fe^{2+} (D(II)). In contrast to Figure 4.6(b), there is no detectable α-Fe in these two samples. This is also in agreement with SR-XRD results (Figure 4.5), where up to an implantation temperature of 473 K no α-Fe is found.

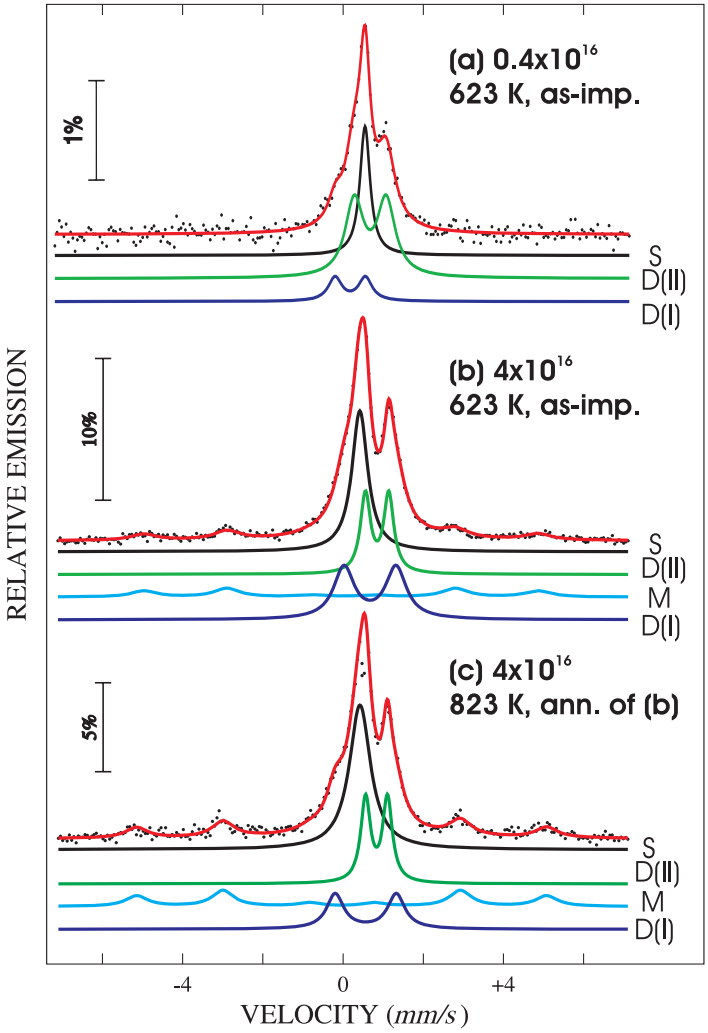

Figure 4.6: Room temperature CEMS of ZnO bulk crystals implanted with ^{57}Fe with different fluences, and after post-annealing. The notations for the fitting lines are given as S (singlet), D (doublet) and M (sextet). The fluence and the process temperatures are indicated.

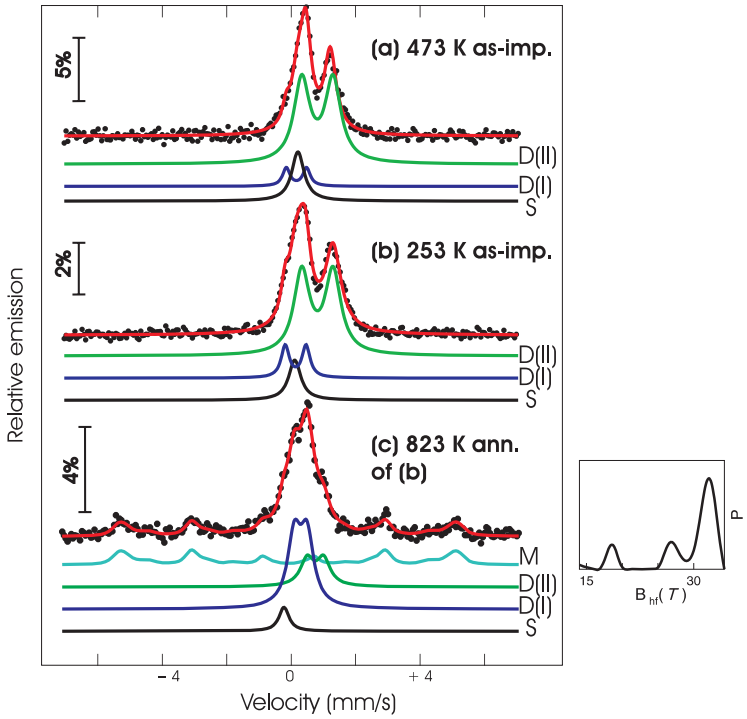

Figure 4.7: Room temperature CEMS for ZnO implanted with ^{57}Fe at 253 K or 473 K and subsequent annealed at 823 K for 15 min. The notations for the fitting lines are given as S (singlet), D (doublet) and M (sextet). On the right side of the spectrum, the probability distribution P for the magnetic hyperfine field (B_{hf}, solid line) are given.

Evolution with post-annealing

The post-annealing was performed on selected samples: S1 and S2 (Table 4.2). They were implanted with the same fluence of 4×10^{16} cm^{-2} at 623 K and 253 K, respectively. For sample S1, upon annealing at 823 K for 15 min, the intensity of the sextet increases up to 18.2% while the fraction of Fe^{2+} (doublet D(I)) decreases, suggesting the growth of the α-Fe nanoparticles and the recovery of lattice defects (Figure 6(c)). Moreover, the value for the magnetic hyperfine field B_{hf} increases upon annealing and moves closer (from 30.5 T to 31.7 T) to the known value for bulk α-Fe (33 T). For sample S2, after annealing at 823 K for 15 min, the relative fraction of metallic α-Fe increases up to 28.8%. The hyperfine field is distributed with maxima at 18 T, 27 T and mostly at 32.5 T (α-Fe). Comparing with the annealing of sample S1, a larger fraction of α-Fe is formed in the annealed sample S2. This is consistent with a larger magnetization measured by SQUID (shown later). In addition, a small fraction of singlet (S) presents, which is attributed to γ-Fe according to the isomer shift.

Higher-temperature (1073 K) annealing was performed on sample S1 and has been reported in Ref [102]. After annealing at 1073 K for 3.5 hours, Fe^{3+} is the only charge state, and Zn-ferrites ($ZnFe_2O_4$) are formed and are crystallographically oriented inside ZnO matrix.

Table 4.2: Hyperfine parameters obtained from the evaluation of CEMS for samples implanted or annealed at different temperatures. The fluence was 0.4×10^{16} cm^{-2} for the first sample, while 4×10^{16} cm^{-2} for all other samples. The codes of S1, S2 and S3 notate the samples for post-annealing process. The notations for the fitting lines are given as S (singlet), D (doublet) and M (sextet).

Sample			S		D(I)			D(II)			M (α-Fe)		
Code	$T_{imp.}$ (K)	$T_{ann.}$ (K)	FR[a] (%)	IS[b] (mm/s)	FR[a] (%)	IS[b] (mm/s)	QS[c] (mm/s)	FR[a] (%)	IS[b] (mm/s)	QS[c] (mm/s)	FR[a] (%)	IS[b] (mm/s)	B_{hf}[d] (T)
	623	-	27.7	0.57	13.7	0.31	0.75	58.6	0.81	0.79	-	-	-
S1	623	-	32.8	0.53	31.5	0.78	1.29	23.2	0.96	0.58	12.5	0.06	30.5
S1	623	823	42.6	0.42	16.7	0.68	1.52	22.5	0.94	0.54	18.2	0.07	31.7
S1	623	1073	-	-	100	0.35	0.43	-	-	-	-	-	-
S2	253	-	13.6	0.22	14.1	0.24	0.65	72.3	0.92	0.97	-	-	-
	473	-	22.2	0.32	9.7	0.27	0.63	68.1	0.94	0.77	-	-	-
S2	253	823	6.2	-0.09	46.8	0.42	0.39	18.2	0.88	0.51	28.8	0.04	Dist.[e]
S3[f]	623	-	23.0	-0.09	26.3	0.45	0.32	37.3	0.91	0.80	13.4	0	Dist.[e]
S3[f]	623	823	13.9	-0.09	31.4	0.45	0.35	15.9	0.92	0.58	38.8	0.02	Dist.[e]

[a] Fraction corresponding to the relative area of the subspectrum.
[b] Isomer shift: 0 mm/s for α-Fe, 0.7-1.2 mm/s for Fe^{2+}, 0.2-0.7 mm/s for Fe^{3+}, and -0.1 mm/s for γ-Fe.
[c] Quadrupole splitting.
[d] Magnetic hyperfine field.
[e] Hyperfine field distribution.
[f] ZnO epitaxial thin films.

4.2.5 Magnetic properties Fe implanted ZnO

In the previous sections, we have reported a thorough investigation on the structural properties, and the charge states of Fe. The main conclusion can be summarized as follows: (i) Upon implantation at a temperature of 623 K, a small part (around 12%) of the implanted Fe ions forms as crystalline Fe already in the as-implanted state, while the major part of the implanted Fe is in ionic states (Fe^{2+}, and Fe^{3+}); (ii) Implantation at a low temperature (253 K) suppresses the metallic Fe formation, and the implanted Fe ions are in ionic states, but they are not magnetically coupled at room temperature; (iii) Post-annealing at 823 K largely enhances the Fe NC formation in all implanted samples for both implantation temperatures (253 K and 623 K). Since CEMS was performed at room temperature only, the magnetic properties of metallic and ionic Fe at low temperature could not be determined. Here we present the results from SQUID magnetometry measured from 5 K to 350 K. We will show that the metallic Fe NCs are superparamagnetic, and they are the predominant contribution to the measured ferromagnetic response even at 5 K. In contrast the ionic Fe is not ferromagnetically coupled even at 5 K.

Fluence dependence

Figure 4.8(a) shows the ZFC/FC magnetization curves in a 50 Oe field for different fluences of Fe implanted ZnO. The FC curves for low fluences of 0.1×10^{16} (not shown for clarity) and 0.8×10^{16} cm^{-2} completely overlap with the corresponding ZFC curves at values close to zero. No superparamagnetic particles are present in the two samples. For larger fluences (above 2×10^{16} cm^{-2}), a distinct difference in ZFC/FC curves was observed. ZFC

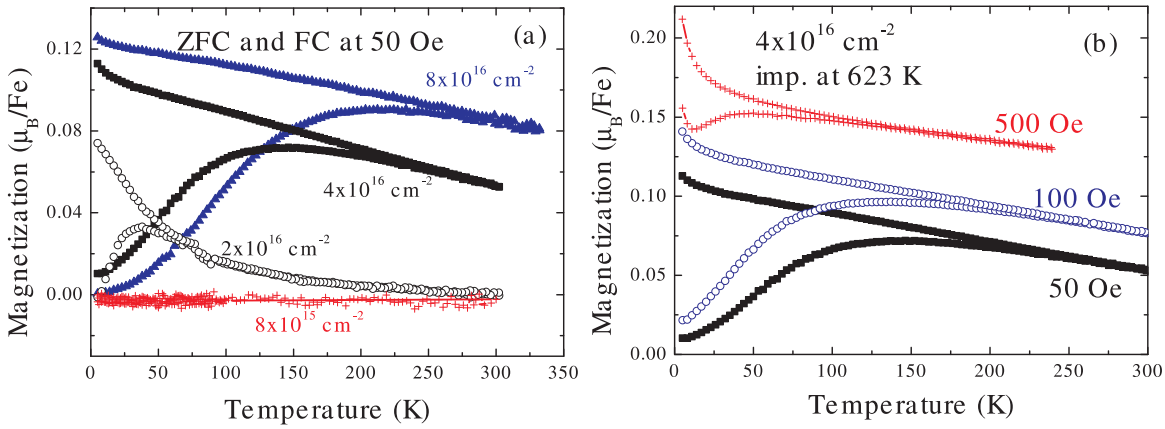

Figure 4.8: (a) Magnetization curves with an applied field of 50 Oe after ZFC/FC for the Fe implanted ZnO. With increasing fluence, the Fe NCs are growing in size, resulting in a higher blocking temperature; (b) ZFC/FC curves with different applied fields. The blocking temperature decreases progressively with increasing field.

curves show a gradual increase (deblocking) at low temperatures, and reach a broad peak with a maximum, while FC curves continue to increase with decreasing temperature. The broad peak in the ZFC curves is due to the size distribution of Fe NCs. In this paper, the temperature at the maximum of the ZFC curve is taken as the average blocking temperature (later referred as T_B). At a much higher temperature than T_B, FC curves still depart from corresponding ZFC curves, which distinguish the Fe particle system from a conventional spin-glass system where the FC curve merges together with ZFC curve just at T_B and shows a plateau below T_B [83]. The ZFC/FC curves are general characteristics of magnetic nanoparticle systems with a broad size distribution [109]. T_B increases with the fluence, *i.e.* the size of nanoparticles. Table 4.3 lists the average size of Fe NCs calculated by Eq. 2.2 and by XRD data (Eq. 5.1), and simulated by Eq. 2.4. Although the trend is the same for all calculations, the values from Eq.2.2 are larger than that from Eq. 2.4 and from XRD data. Given the large size distribution in the present magnetic nanoparticle system, T_B is overestimated by taking the temperature at the maximum of the ZFC curve [79]. This explains why Eq. 2.2 gives a large average particle size. For the fitting according to Eq. 2.4, one has to note that M_s and $K_{eff}(V)$ are assumed to be temperature independent, and the interaction between the NCs is ignored. These effects contribute to the error bars [84]. Nevertheless, from both techniques (XRD, and ZFC magnetization), we have determined the size of Fe NCs and its distribution.

Figure 4.8(b) shows ZFC/FC curves with an applied field ranging from 50 Oe to 500 Oe for the sample with fluence of 4×10^{16} cm^{-2}. T_B in the ZFC curves clearly shifts to lower temperatures with increasing field. This behavior is expected for magnetic nanoparticles. The external magnetic field can reduce the energy barrier (the term of $K_{eff}V$ in Eq. 2.2). Therefore T_B is smaller when the external field is larger [75, 82].

Figure 4.9(a) shows the magnetization versus field reversal (M-H) of samples implanted with large fluences. At 5 K, hysteretic behaviors were observed for all three samples. The

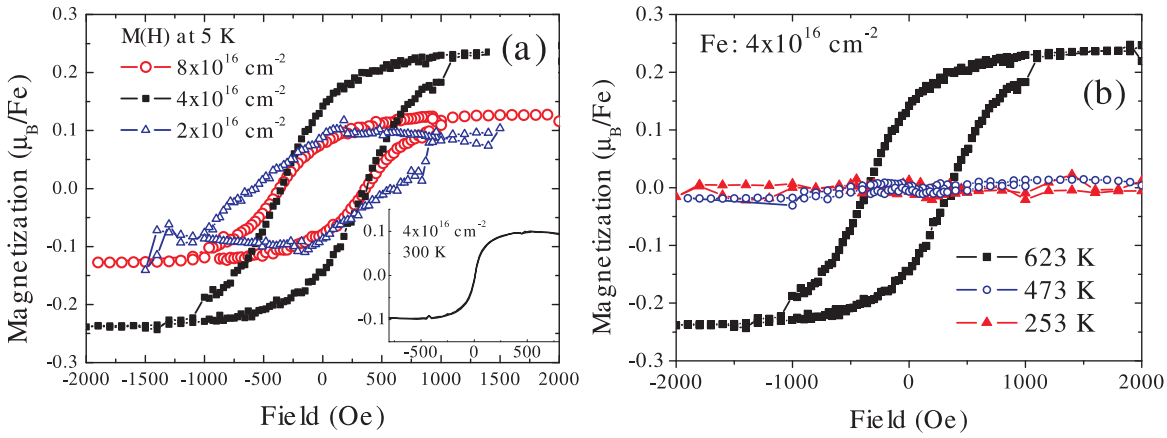

Figure 4.9: (a) Hysteresis loops measured at 5 K for Fe implanted ZnO with different fluence. The inset shows the room temperature M-H loop for the sample implanted with a fluence of 4×10^{16} cm^{-2}. (b) Hysteresis loops measured at 5 K for Fe implanted ZnO at different implantation temperatures with the same fluence of 4×10^{16} cm^{-2}.

saturation moment is increased with increasing fluence, however the coercivity is decreased from 600 Oe for a fluence of 2×10^{16} cm^{-2} to 330 Oe for larger fluences (see table I). This can be explained by the enhanced coercivity effect for the interfacial spins, which increases with decreasing the size of nanoparticles [110]. The inset shows the M-H curve at 300 K for the sample implanted with the fluence of 4×10^{16} cm^{-2}. As expected for a magnetic nanoparticle system, above the blocking temperature, both remanence and coercivity drop to zero.

Implantation temperature dependence

Figure 4.9(b) shows the magnetization versus field reversal of samples implanted with Fe (4×10^{16} cm^{-2}) at different implantation temperatures. Only the sample implanted at 623 K shows a hysteretic behavior due to the presence of Fe NCs, while the other samples implanted at 473 K or below show no ferromagnetic response down to 5 K. This is in full agreement with SR-XRD and CEMS measurements.

Post annealing effect

The annealing behavior of the samples implanted at 623 K has been reported in a previous paper [102]. The main conclusions are the following: the annealing at 823 K results in the growth of α-Fe NCs. During annealing at 1073 K the majority of the metallic Fe is oxidized; after a long-term annealing at 1073 K, crystallographically oriented $ZnFe_2O_4$ NCs form. Here we mainly present the annealing at 823 K for the samples implanted at 253 K. Due to the different initial state from the 623 K implanted samples, the same annealing temperature leads to different results.

Figure 4.10 shows the magnetic properties of the samples implanted at 253 K with subsequent post annealing. In the as-implanted state, there is no ferromagnetism down to 5 K, while after 823 K annealing, magnetization of 0.52 m_B/Fe was observed. The ZFC/FC

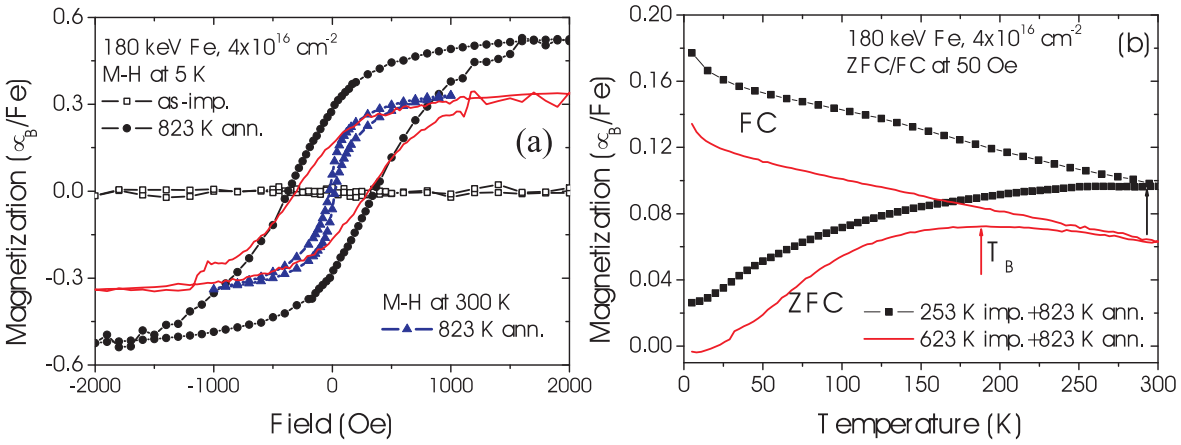

Figure 4.10: Hysteresis loops measured at 5 K for ZnO implanted with 180 keV Fe at 253 K (as-implanted and post annealed). The fluence is 4×10^{16} cm^{-2}. For comparison, the sample implanted with the same energy and fluence, but at a high implantation temperature (623 K), after the same annealing process is shown as the solid line. (b) ZFC/FC magnetization of the sample after 823 K annealing. The arrows indicate the blocking temperatures.

magnetization curves show the characteristics of magnetic nanoparticle system. According to SR-XRD and CEMS results, we attribute this to Fe NCs. The ZFC curve is very broad and T_B is above room temperature. The M-H curve at 300 K is still open, though with much smaller coercivity and remanence compared to 5 K. However the magnetic properties are quite different from the 623 K implanted sample after post annealing at 823 K, where the T_B is well below 300 K, and at 300 K there is neither coercivity nor remanence. We will discuss this difference in section 4.3.

Magnetic anisotropy of Fe NCs

M-H loops were also measured for selective samples which have been implanted with a fluence of 4×10^{16} cm^{-2} with the field applied perpendicular to the sample surface. Figure 4.11 shows the comparison of the magnetization between the in-plane and out-of-plane directions at 5 K. The in-plane (parallel to the ZnO surface) is the easy axis, while the out-of-plane (perpendicular) is the hard axis. At 5 K, the coercivity of the easy axis is around 360 Oe, and the ratio of M_R/M_S (remanence and saturation moment) is around 58%. The anisotropy energy, K, can be calculated according to the equation of $K=M_sH_A/2$, where M_s is the saturation moment of $4\pi M_s$=22000 G, H_A is the effective anisotropy field. Indeed H_A is rather difficult to be deduced since it is not easy to measure a *real* hard axis loop with SQUID magnetometry without a precise control of the sample alignment. Moreover the size distribution of Fe NCs could result in a distribution of H_A. Therefore, we deduce a lower and upper limit of H_A as 1030 Oe and 1880 Oe, respectively, according to the shape of the hard axis loop. Using this approach, the anisotropy energy is estimated to be in the range of (0.9-1.6)$\times10^5$ Jm^{-3}. It is larger than the magnetocrystalline anisotropy, and around one order of magnitude larger than the uniaxial anisotropy observed in Fe thin films [111] and

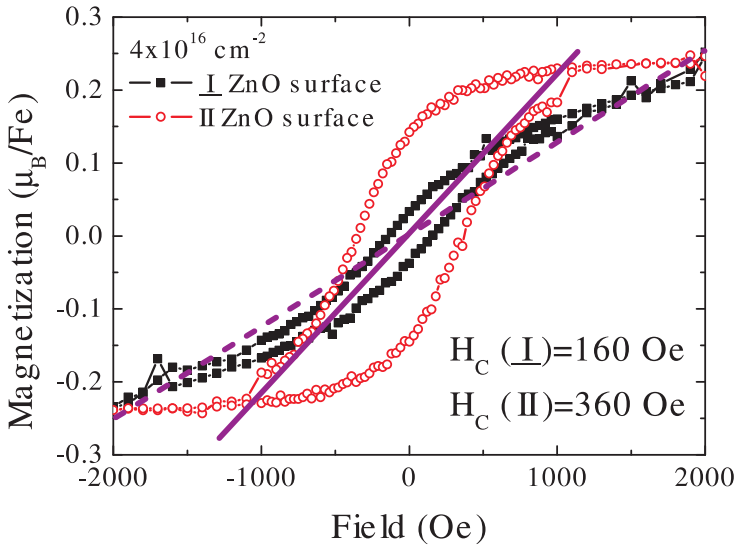

Figure 4.11: Hysteresis loops measured at 5 K for Fe implanted ZnO at 180 keV and 623 K up to a fluence of 4×10^{16} cm^{-2}. The field is changed from parallel to perpendicular with respect to the sample surface, revealing the magnetic anisotropy. The intersections between the easy axis M-H curve and solid and dashed direct lines indicate the lowest and highest H_A.

micro-scale Fe nanomagnets [112]. If the Fe NCs are assumed to be sphere-like, their magnetism should be isotropic, unless they are textured. However as found by XRD, these Fe NCs are not textured. This magnetic anisotropy could be due to the shape effect of Fe NCs, *i.e.* they are not sphere-like, or magnetostriction. There is, however, no evidence for any of these two possibilities.

Memory effect of Fe NCs

Below the blocking temperature, a magnetic nanoparticle system has a rich and unusual behavior. For instance a slow relaxation and a history-dependent magnetic memory are found in the dc magnetization as a function of temperature [83, 109, 113, 114, 115]. In our system, Fe nanoparticles embedded inside ZnO crystals, the temperature dependent memory effect was also observed (Figure 4.12) using a cooling and heating protocol suggested by Sun *et al.* [83]. At 300 K a magnetic field of 50 Oe was applied and the sample was cooled down to 5 K at a constant cooling rate of 3 K/min. Then the sample was heated continuously at the same rate and the magnetization was recorded. The obtained M(T) curve is referred as the reference curve (solid line in Figure 4.12). Thereafter, we cooled the sample at the same rate and recorded the magnetization with cooling, but temporarily stopped at T = 50 K for a waiting time of 2 hours. During the waiting time the field was switched off. After the stop, the 50 Oe field was reapplied and cooling and measuring were resumed. The temporary stop resulted in a steplike M(T) curve (solid squares in Figure 4.12). After reaching the lowest temperature 5 K, the sample was heated back with the rate of 3K/min in the same field, and the magnetization was recorded again. The M(T) curve during this heating also has a steplike behavior at the stop temperature of 50 K, then recovers the previ-

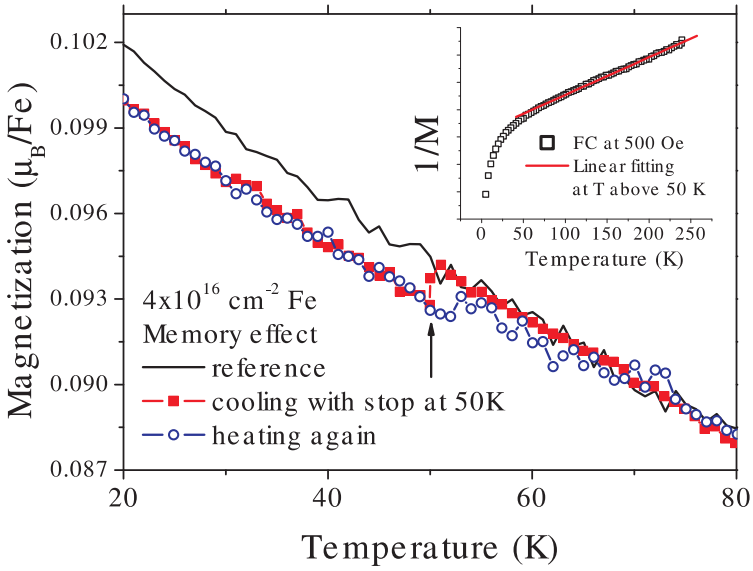

Figure 4.12: Temperature dependent memory effect in the dc magnetization. The reference curve is measured on heating at a constant rage of 3 K/min after FC in 50 Oe. The solid squires are measured during cooling in 50 Oe at the same rate but with a stop of 2 hours at 50 K. The field is cut off during stop. The open circles are measured with continuous heating at the same rate after the previous cooling protocol. Inset shows the reciprocal magnetization versus temperature.

ous M(T) curve measured during cooling. The system remembers its thermal history. Two explanations have been suggested for such a memory effect [114]. The first one is a broad distribution of blocking temperatures originating from the distribution of the anisotropy energy barriers. Another explanation is the strong dipolar interaction between nanoparticles, which frustrates the nanomagnetic moments, and slows down their relaxation. Our observations rather support the first model. First of all, the memory effect is also observed for two other samples (2×10^{16}, and 8×10^{16} cm^{-2}) (not shown). Therefore the effect is independent of ion fluence, *i.e.* particle density. Second, the inset of Figure 4.12 shows the reciprocal FC magnetization at 500 Oe versus temperature. The perfect linearity of the curve for T>50 K strongly suggests that the dynamics of the nanoparticles above blocking temperature can be well described by superparamagnetism. Therefore, the magnetic properties of the sample depend only on the individual particle behavior. Third, the size of Fe nanoparticles is widely dispersed according to the analysis on the ZFC magnetization curve. Therefore, we would attribute the memory effect to the broad distribution of particle size, *i.e.* of anisotropic energy barriers.

4.2.6 Fe implanted epitaxial ZnO layers

The epitaxial ZnO layers used in this study were grown by pulsed layer deposition on Al_2O_3(0001). These thin films are n-type conducting with a carrier concentration of 10^{15}-10^{17} cm^3 at room temperature. Details about the sample preparation can be found in Refs. [116, 117, 118]. ^{57}Fe ions were implanted at an energy of 180 keV at 623 K. Then the samples were subjected to the same thermal annealing, and structural as well as magnetic characterization

Table 4.3: Structural and magnetic properties of Fe-implanted ZnO. The ferromagnetic fraction corresponds to the percentage of ferromagnetic Fe (at 5 K) compared with all implanted Fe ions. The crystallite size evaluated by ZFC magnetization is only for α-Fe NCs.

Sample			Cryst. size	T_B	Cryst. size		Saturation	Ferro. Fe	Coercivity
Fluence	$T_{imp.}$	$T_{ann.}$	(XRD)	(ZFC)	Eq. 2.2	Eq. 2.4	magn. (5 K)	fraction[b]	at 5 K
(cm^{-2})	(K)	(K)	(nm)	(K)	(nm)		(μ_B/Fe)	(%)	(Oe)
2×10^{16}	623	-	5.6	38	8	6.6	0.08	3.6	600
4×10^{16}	623	-	7.1	137	12	8.9	0.24	11	360
8×10^{16}	623	-	8.9	212	14	11.3	0.13	5.9	360
4×10^{16}	623	823	9.4	200	14	10.2	0.34	15	360
4×10^{16}	253	823	-	295	16	9.5	0.52	24	370
4×10^{16}[a]	623	-	-/6 (α/γ-Fe)	26	7	4.6	0.55	25	220
4×10^{16}[a]	623	823	8.1/11 (α/γ-Fe)	280	15	10.2	1.3	59	220

[a] ZnO epitaxial layers implanted with Fe at 180 keV and 623 K.

[b] Ferromagnetic Fe fraction, calculated by comparing the saturation magnetization with the value (2.2 μ_B/Fe) for bulk Fe.

like the bulk crystals.

Formation of Fe NCs

Figure 4.13(a) shows the XRD 2θ-θ scans of Fe implanted ZnO epitaxial layers (as-implanted and post annealed at 823 K). In the left panel, one can see the diffraction from ZnO(0002) and Al_2O_3(0006). The right panel is a zoom on the Fe-related peak region. A single crystal sample implanted with the same fluence and at the same temperature is shown for comparison. Obviously, the epitaxial ZnO behaves differently from the bulk crystals upon Fe implantation. In the epitaxial-layer, γ-Fe is the predominant phase, while it is α-Fe in the single crystal. This difference will be discussed in section 4.3. Upon thermal annealing at 823 K, the epitaxial ZnO behaves similar to the low-temperature implanted bulk crystals. Both metallic Fe phases (α and γ) are growing.

Charge state of Fe

The charge and chemical states of Fe deduced from CEMS are shown in Figure 4.14. The hyperfine interaction parameters are given in Table 4.2. In the as-implanted sample, ionic Fe is the predominant phase, while also α- and γ-Fe are present (sextet M and singlet S, respectively). After annealing at 823 K, the fraction of ferromagnetic α-Fe is drastically increased from 13.4% to 38.8%. In the bulk crystal implanted at the same condition, there is no γ-Fe neither in as-implanted nor in annealed samples. Also the fraction of α-Fe after annealing (18.2%) is much lower than that in epitaxial films (38.8%).

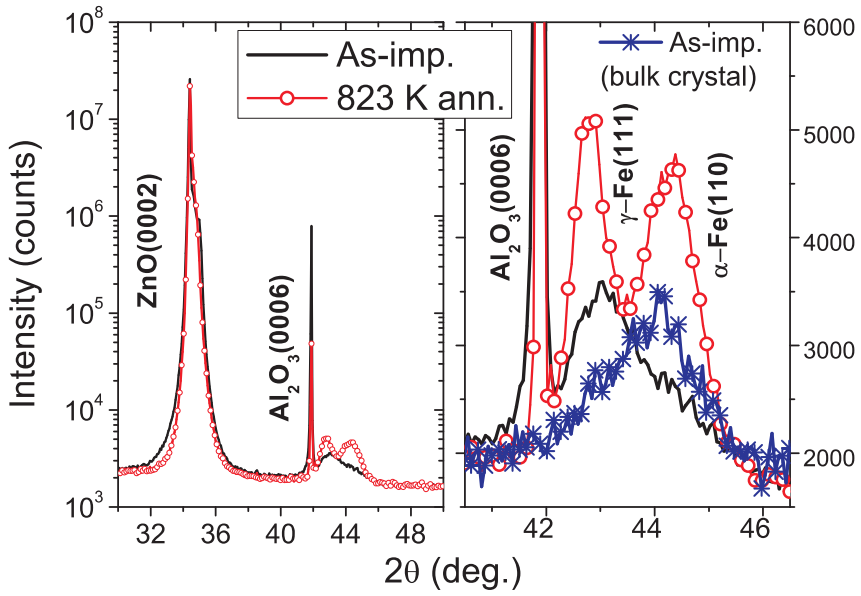

Figure 4.13: SR-XRD 2θ-θ scans of Fe implanted epitaxial ZnO layers: as-implanted and post annealed at 823 K. Left panel shows long-range scans and right panel shows the range near Fe related peaks. The bulk crystal ZnO implanted at the same condition is shown for comparison (star symbolled line in the right panel).

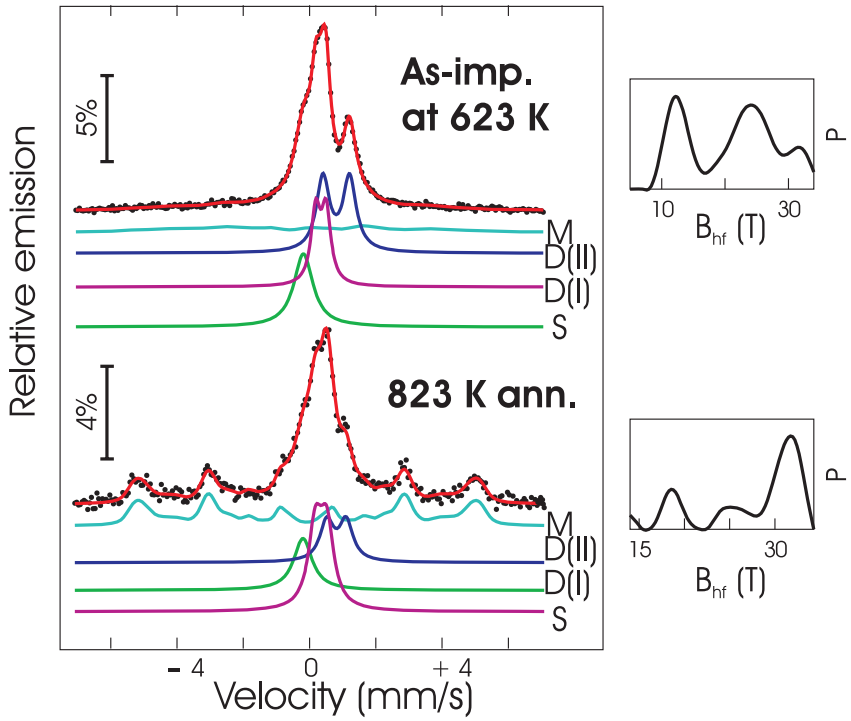

Figure 4.14: Room temperature CEMS of ZnO epitaxial thin films as-implanted with ^{57}Fe and post-annealed at 823 K for 15 min. The notations for the fitting lines are given as S (singlet), D (doublet) and M (sextet). On the right side of the spectra, the probability distribution P for the magnetic hyperfine field (B_{hf}, solid lines) are given.

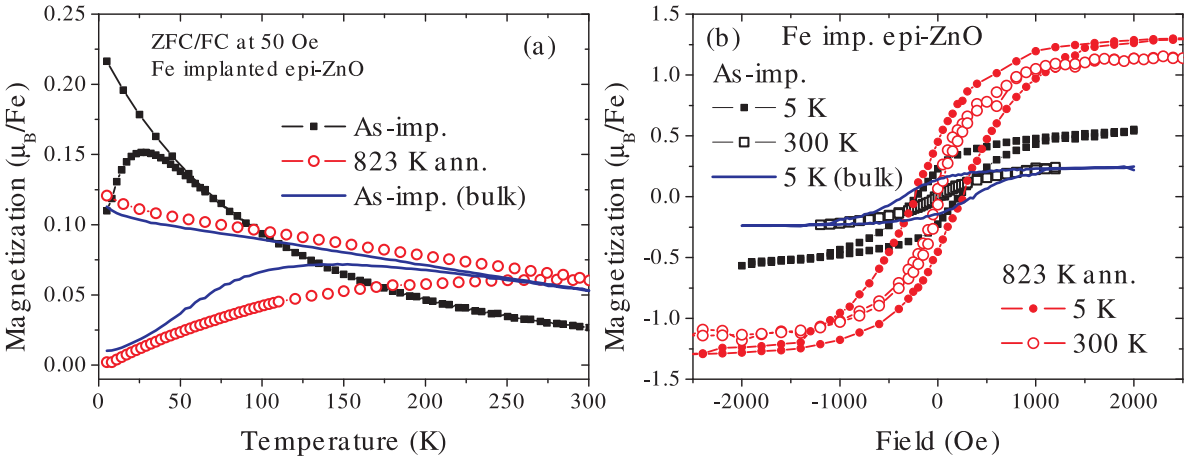

Figure 4.15: (a) ZFC/FC magnetization curves at an applied field of 50 Oe for the as-implanted and 823 K annealed ZnO films; (b) M-H loops at 5 K and 300 K. The bulk crystal ZnO implanted at the same condition is shown as solid lines for comparison.

Magnetic properties

The ZFC/FC magnetization measurements for the as-implanted and 823 K annealed samples (Figure 4.15(a)) shows the typical behavior of a magnetic nanoparticle system. However T_B in the ZFC curves increases from 26 K to around 300 K with post annealing. The absolute magnetization value per Fe in the ZFC/FC curves for the annealed sample is lower than that of the as-implanted sample. This is due to the fact that there are more bigger Fe NCs after annealing, and the bigger NCs are more difficult to be aligned at field as small as 50 Oe. Figure 4.15(b) shows the M-H curves. The coercivity is not significantly changed with annealing, while the saturation magnetization is increased from $0.55\mu_B$/Fe to $1.3\mu_B$/Fe at 5 K and from $0.24\mu_B$/Fe to $1.1\mu_B$/Fe at 300 K, respectively, with annealing. For both samples, the M-H loops show no hysteresis at 300 K without coercivity and remanence. Obviously, the annealing behavior is different from the single crystal implanted at same temperature of 623 K, but similar to the single crystal implanted at 253 K. We will discuss this point in section 4.3.

4.2.7 Synthesis of magnetic $ZnFe_2O_4$

In this section, I show the synthesis of Zn-ferrites by Fe implantation into ZnO and post-annealing. In the as-implanted ZnO sample, a fraction of Fe is in metallic state, and is responsible for the magnetic property. An annealing at 823 K enhanced the Fe particle formation, but Fe nanoparticles were oxidized after an annealing at 1073 K. A further annealing at 1070 K for 3.5 h induced the formation of crystallographically oriented $ZnFe_2O_4$ onto ZnO with the orientation relationship of $ZnFe_2O_4(111)[110]||ZnO(0001)[11\underline{2}0]$. These $ZnFe_2O_4$ nanocrystals show a hysteretic behavior upon magnetization reversal at 5 K

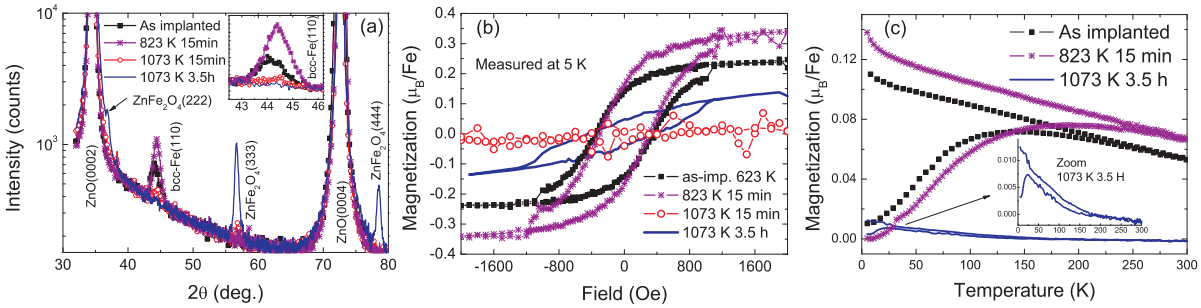

Figure 4.16: (a) SR-XRD patterns (2θ-θ scans) of Fe implanted ZnO reveal the second phase development (from α-Fe to $ZnFe_2O_4$) upon annealing. (b) Magnetization versus field reversal revealing the magnetism evolution upon annealing; (c) ZFC/FC magnetization curves at 5 mT, which exhibit a typical characteristic of a magnetic nanoparticle system.

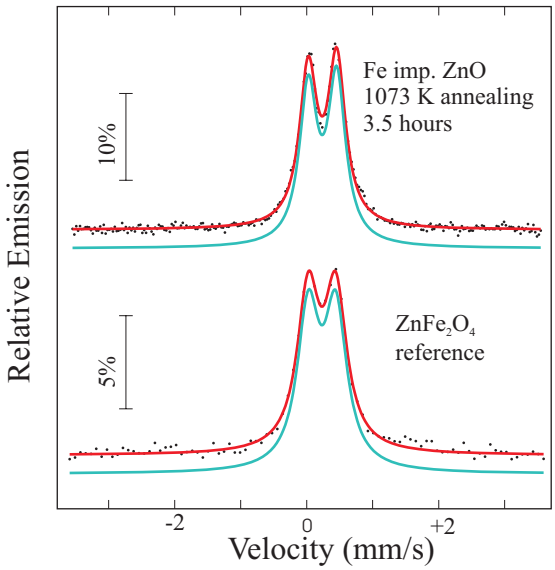

Figure 4.17: CEMS of Fe implanted ZnO after annealing at 1073 K for 3.5 hours. A reference sample of powder $ZnFe_2O_4$ is also shown for comparison.

Formation of $ZnFe_2O_4$

Figure 4.16(a) shows the SR-XRD patterns for the as-implanted and annealed samples. For the as-implanted sample, crystalline α-Fe nanoparticles were observed, and no other Fe-oxide (Fe_2O_3, Fe_3O_4, and $ZnFe_2O_4$) particles were detected. The crystallite size is calculated using the Scherrer formula [105]. After 823 K and 15 min annealing, larger and more Fe nanoparticles are formed reflected by an increase and the sharpening of the corresponding peak at 44.4° in the 2θ-θ scan. After 1073 K and 15 min annealing, the Fe(110) peak almost disappeared and the sample already shows an indication for the presence of $ZnFe_2O_4$. After 3.5 hours annealing at 1073 K, crystalline and oriented $ZnFe_2O_4$ particles are clearly identified. The inset shows a zoom of the Fe(110) peak to show the development of Fe nanoparticles more clearly.

The formation of Zn-ferrites is further confirmed by CEMS (Figure 4.17. After 3.5 hours annealing, the CEMS pattern exhibits only one quadrupole split line typical for $ZnFe_2O_4$ at

room temperature [119, 120, 121, 122].

Magnetic properties of $ZnFe_2O_4$

Figure 4.16(b) shows the magnetization versus field reversal (M-H) at 5 K. Magnetic hysteretic loops are observed for the as-implanted sample, which contains α-Fe nanoparticles. After annealing at 823 K for 15 min, the ferromagnetism is enhanced, *i.e.* Fe nanoparticles are growing in size and amount. However, after annealing at 1073 K for 15 min, no hysteresis loop is observed. Probably the majority of Fe particles were oxidized to some amorphous nonmagnetic compound. The magnetism evolution is in a good agreement with the XRD measurement. After annealing at 1073 K for 3.5 hours, the hysteretic behavior is observed again, which - according to the SR-XRD - cannot come from Fe nanoparticles, but from partially inverted $ZnFe_2O_4$, which is ferrimagnetic [119, 120, 121, 122, 123]. bulk $ZnFe_2O_4$ which is a weak antiferromagnet with a Neél-temperature of 10.5 K. Bulk $ZnFe_2O_4$ exhibits normal spinel structure with Zn^{2+} ions solely at the tetrahedral (A) sites and antiferromagnetically coupled Fe^{3+} ions solely at the octahedral (B) sites. A recent theoretic description along with an overview of experimental results for that material is given by D. J. Singh *et al.* [124]. Recent experiments, however, reveal that nanocrystalline $ZnFe_2O_4$ shows ferrimagnetic behaviour up to 460 K, almost independently on the preparation method [73, 119, 121, 122, 123, 125, 126]. The explanation for such behavior is the partial inversion of the spinel structure, *i.e.* the additional occupation of tetrahedral A sites by Fe and octahedral B sites by Zn as well as a strong superexchange coupling of the intra-sublattice Fe ions.

In order to confirm the superparamagnetic properties of the embedded nanoparticles, zero-field cooled (ZFC) and field cooled (FC) magnetization vs. temperature measurements were performed using SQUID. Figure 4.16(c) shows the ZFC/FC magnetization curves in an applied field of 50 Oe. For all samples, although there is a difference in magnetic moment, ZFC curves show a gradual increase (deblocking) at low temperatures, and reach a plateau at a particular temperature of T_B, while all FC curves continue to increase with decreasing temperature. The shape of the ZFC/FC curves are general characteristics of magnetic nanoparticle systems [80], *i.e.* magnetic nanoparticles are the origin of the ferromagnetism in all the samples. The increase of T_B after annealing at 823 K for 15 min confirms the growing of α-Fe nanoparticles. After annealing at 1073 K for 3.5 h, $ZnFe_2O_4$ crystallites with an average grain size of 20 nm were formed. However the degree of inversion (transition from Fe^{3+} to Fe^{2+}) is decreased with increasing crystallites [122], therefore comparing with the grain size of 6.6 nm and 14.8 nm in Ref. [122], the rather bigger grain size of $ZnFe_2O_4$ crystallites (20 nm) results in a small magnetic moment and a low T_B. Also the effective anisotropy constant of $ZnFe_2O_4$ is lower than that of α-Fe [121], which could explain the lower Tmax than that of Fe nanoparticles [80].

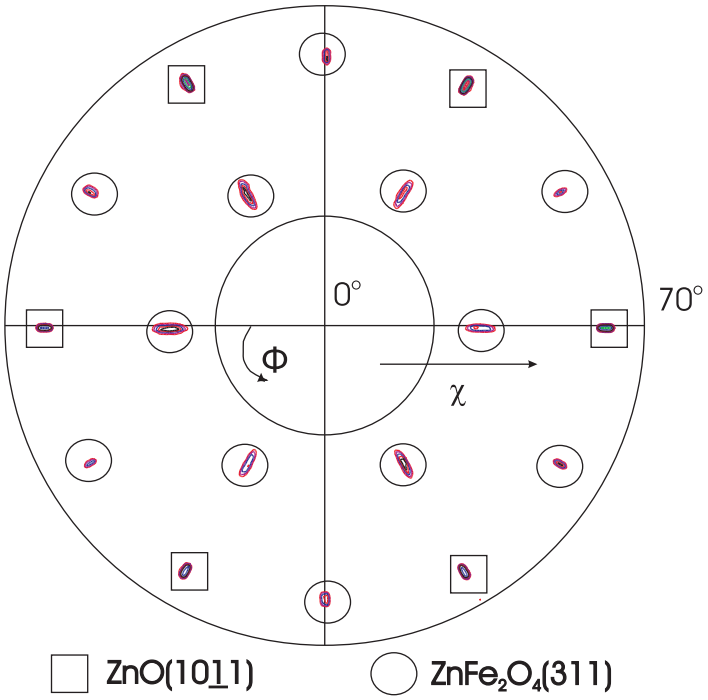

Figure 4.18: Pole figure of $ZnFe_2O_4$(311) reveals the crystallographical orientation of $ZnFe_2O_4$ and its twin crystallites.

Crystallographical orientation of $ZnFe_2O_4$

In Figure 4.16(a), the XRD pattern for the sample after 3.5 hours annealing at 1073 K shows only three peaks of $ZnFe_2O_4$(222) (333) and (444), which means that the crystallites of $ZnFe_2O_4$ are not randomly oriented, but highly oriented. The surface orientation is $ZnFe_2O_4$(111)//ZnO(0001). The crystallographical orientation of $ZnFe_2O_4$ was revealed by the XRD pole figure. Figure 4.18 shows the pole figure for $ZnFe_2O_4$(311). The radial coordinate is the angle (χ) by which the surface is tilted out of the diffraction plane from 0° to 70°. The azimuthal coordinate is the angle of rotation about the surface normal. The pole figure shows poles of $ZnFe_2O_4$(311) at χ∼29.5°and 58.5°, respectively, with sixfold symmetry. Since ZnO(1011) (2θ=36.25°) has a close Bragg angle with $ZnFe_2O_4$(311) (2θ=35.27°), the poles of ZnO(1011) also show up at χ∼61.6° with much more intensities. The result is consistent with the theoretical $ZnFe_2O_4$(311) pole figure viewed along [111] with rotation twins. The in-plane orientation relationship is $ZnFe_2O_4$[110]//ZnO[11$\bar{2}$0]. Moreover, a 2θ-θ scan was carried out for $ZnFe_2O_4$(311)(622) and (220)(440), respectively, by tilting the sample with an angle of χ at an azimuthal position found by pole figure. The results are shown in Figure 4.19, and confirm the crystallographical orientation of $ZnFe_2O_4$. The coherence length of crystallites is around 20 nm in the out-of-plane direction. The in-plane coherence length is evaluated to be also as large as 20 nm by measuring the diffraction of (311) at χ∼80°, nearly parallel with the surface [127]. Due to the fcc structure of $ZnFe_2O_4$ (a=0.844 nm), it is not difficult to understand its crystallographical orientation onto hcp-ZnO (a=0.325 nm) with twin-crystallites of $ZnFe_2O_4$ of an in-plane rotation by 60° (Fig.5). The lattice mismatch

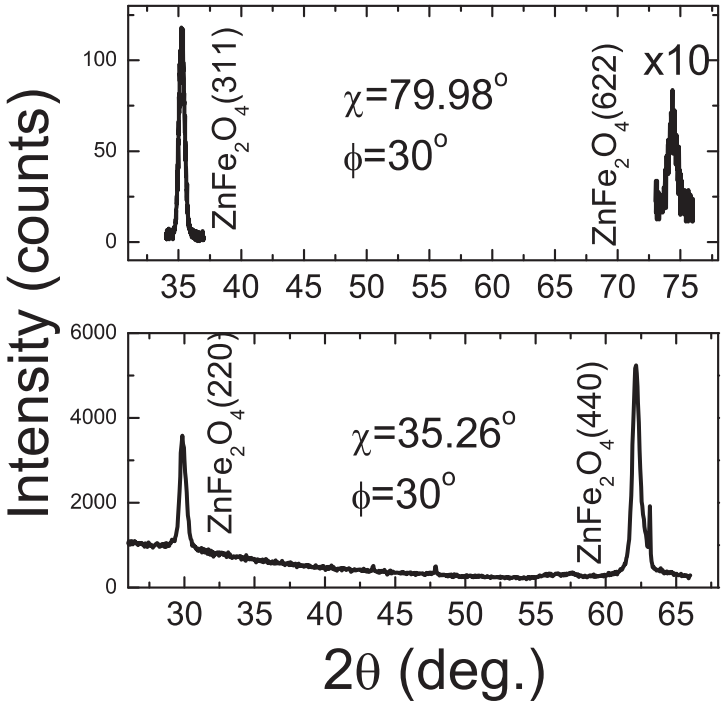

Figure 4.19: 2θ-θ scans of $ZnFe_2O_4$(311)(622) and (220)(440).

between $ZnFe_2O_4$ and ZnO is 6%.

Additionally SEM was performed to check the sample morphology. Figure 4.21(a) and (b) show the SEM results for the as-implanted and the annealed samples. After the annealing, the morphology was pronouncedly changed. Some speckle-like features with dimensions of 100 nm were formed on top of ZnO. Using energy dispersive x-ray (EDX), these features are Fe-riched islands, while in the flat area, no Fe is detectable (Figure 4.21(c)). Together with above-mentioned SR-XRD and CEMS observations, these speckle-like Fe-riched features are most probably $ZnFe_2O_4$. This feature size is not necessary to be the same as the coherence length (crystallite size) as revealed by XRD since one feature can consist several crystallites,

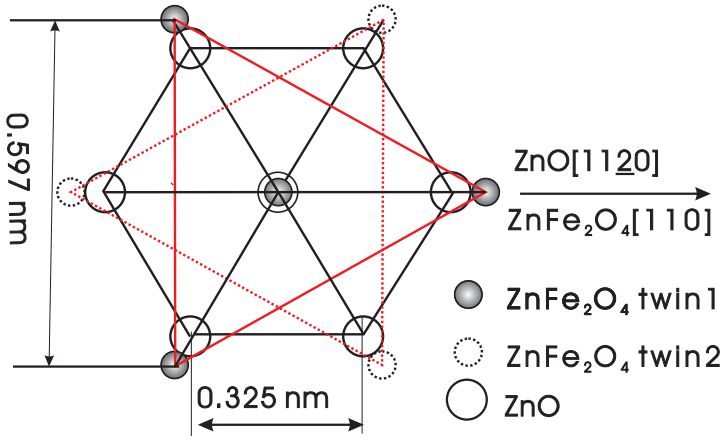

Figure 4.20: A schematics for the crystallographical orientation of $ZnFe_2O_4$ onto ZnO.

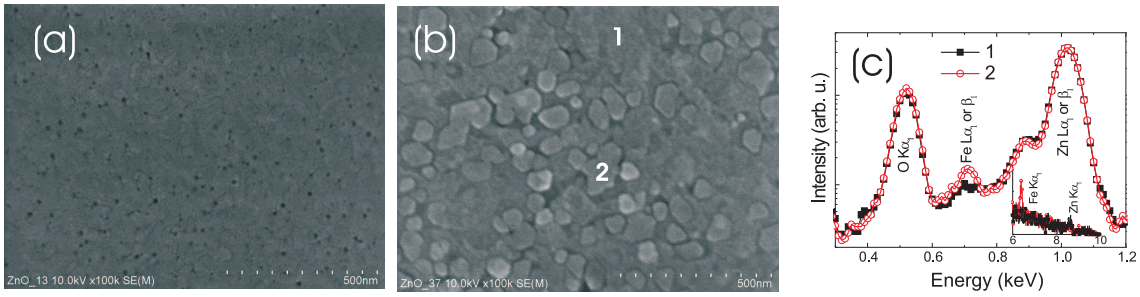

Figure 4.21: SEM shows the morphology of samples (a) rather flat surface in as-implanted sample, (b) Fe-riched features on the surface after 3.5 h annealing at 1073 K. (c) EDX spectra at different spot of Figure (b) (inset shows the higher energy parts of the spectra).

however SEM cannot distinguish them. Thus, Fe is partially diffused towards the sample surface during annealing, and therefore the $ZnFe_2O_4$ crystallites are located in the region near surface.

Generally, spinel ferrites (MFe_2O_4, M=Ni, Co, Fe, Mn, Zn) have a large variety of magnetic properties and have significant potential application in millimeter wave integrated circuitry and magnetic recording [128]. They all have an fcc structure with the lattice constant a of around 0.84 nm, and exhibit different magnetic properties depending on the chemical composition and cation site occupancy [129]. In the view of lattice mismatch, our results could suggest the epitaxy of spinel ferrites onto ZnO, and even a multi-layered MFe_2O_4/ZnO structure given the growth method compatibility by pulsed laser deposition or molecular beam epitaxy for both materials [24, 128]. The magneto-transport properties of inverted $ZnFe_2O_4$ nanoparticles are recently investigated. Ponpandian et al. discussed a hopping mechanism between Fe^{3+} and Fe^{2+} pairs present at the octahedral sites [130]. In Ref. [73], Shinagawa *et al.* reported ferromagnetic ZnO-Spinel iron oxide composites prepared by wet chemical process with a negative magnetoresistance of -0.35% at room temperature. Thus, a hybrid structure of spinel ferrites/semiconducting ZnO could be a potential candidate for spintronic devices.

4.3 Discussion

4.3.1 Phase diagram of Fe in ZnO

In section 4.2, we have presented the structure and magnetic properties of Fe implanted ZnO. The implantation parameters, *i.e.* fluence, energy, temperature, were varied. In general, metallic Fe NCs have been formed already in the as-implanted state when the implantation temperature is above 623 K and the fluence is above 2×10^{16} cm^{-2}. By summarizing all results, a phase diagram of Fe in ZnO can be sketched, as shown in Figure 4.22. Note that the materials studied in this research are ZnO bulk crystals grown by the hydro-thermal method. They are semi-insulating in the as-purchased state with n-type carrier concentration of 10^{12}-10^{14} cm^{-3}. The phase diagram will likely be different for epitaxial-ZnO and for

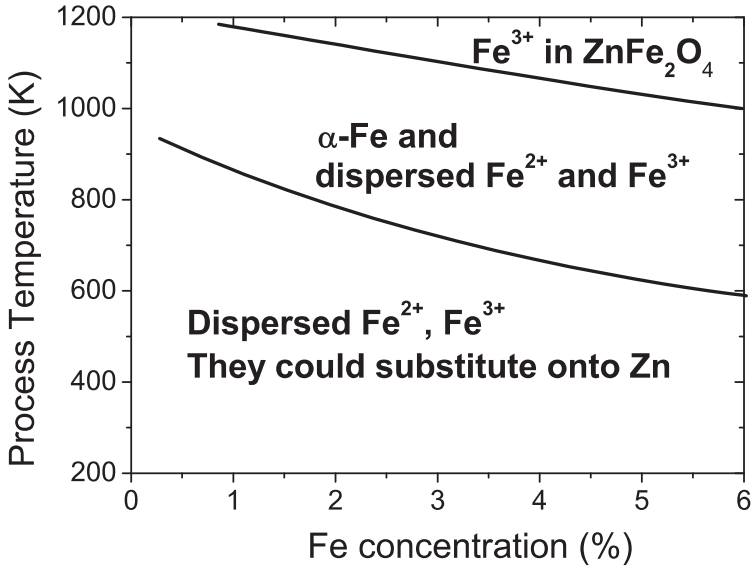

Figure 4.22: The phase diagram of Fe in ZnO bulk crystals derived from the data presented in this work. The process temperature refers to the implantation or annealing temperature.

p-type ZnO.

4.3.2 Phase separation depends on ZnO materials

In section 4.2, we have shown the structural and magnetic properties of ZnO bulk crystals and epitaxial thin films implanted at the same temperature and with the same Fe fluence. They are obviously different from each other (see table 4.3). In the bulk crystals, only 11% (increased to 15% after 823 K post annealing) of the implanted Fe is ferromagnetic and mainly α-Fe, while 25% in the epitaxial ZnO films (increased to 59% after 823 K post annealing). Recently Dietl proposed the self-organized growth driven by the charge state of the magnetic impurities [57][131]. The energy levels derived from the open *d* shells of transition metals reside usually in the bandgap of the host semiconductor. The mid-gap levels of magnetic impurities trap carriers origination from residual impurities or defects. This trapping alters the charge state of the magnetic ions and hence affects their mutual Coulomb interactions. Therefore, different carriers (electrons or holes, with different concentrations) could lead to different interactions (*e.g.* repulsion or attraction) between the implanted transition metal ions, and finally result in a different phase separation. Both ZnO materials (bulk crystals and epitaxial thin films) used in this study are n-type semiconductors. The carrier concentration is around 10^{12}-10^{13} cm^{-3} for bulk crystals and 10^{15}-10^{17} cm^3 for epitaxial thin films [116, 117] at room temperature. Therefore, we can explain the different behavior in ZnO bulk crystals and epitaxial layers upon Fe implantation in the above-mentioned model. A higher concentration of free electrons leads to more agglomerations of Fe. Moreover the nanocrystal aggregation could be largely reduced or avoided by the realization of p-type doping in ZnO.

However, one has to note that there are a lot of defects, such as dislocations, and stacking

faults, in the epitaxial ZnO films grown on Al_2O_3 due to the large lattice mismatch [132]. Kaiser *et al.* demonstrated that in high-fluence Er implanted SiC the defects act as nucleation sites in the formation of Er-atom cluster and NCs [133]. A similar effect can be present in the case of Fe implanted ZnO films.

4.3.3 Annealing behavior depends on the initial state

Note that three kind of samples have been annealed at the same temperature of 823 K. One is the ZnO single crystal implanted at 623 K, in which Fe NCs have already been formed in the as-implanted states. One is the ZnO single crystal implanted at 253 K, in which no Fe NCs could be detected in the as-implanted sample. The last one is the ZnO thin film implanted at 623 K, in which rather small Fe NCs have been formed in the as-implanted sample compared to that in the single crystal. The annealing behavior in the first case is quite different from the latter two cases. One reason is the fact that diffusion of Fe NCs is much more difficult than of single Fe ions. In the 623 K implanted sample, Fe NCs have already been formed, and they are not so mobile during 823 K annealing. Therefore the size and the amount of Fe NCs only slight increase after annealing. However, in the sample without Fe NCs or with very small NCs, Fe ions are more mobile with annealing, and they aggregate into rather larger Fe NCs. Another reason could be the same as discussed in the above section, given the fact that implantation at 253 K induces more point defects than that at 623 K (see Figure 4.2).

4.3.4 Magnetic coupling of dispersed ionic Fe

Although a part of the implanted Fe ions have aggregated to metallic NCs, the remaining ones are in the ionic state. Even after 823 K annealing, there is still a considerable amount of ionic Fe. By SR-XRD no crystalline Fe-oxides could be detected. Therefore, these ionic Fe could be diluted inside ZnO matrix. However, as measured by SQUID down to 5 K and CEMS at room temperature, Fe^{2+} and Fe^{3+} are not ferromagnetically coupled.

In addition to conventional thermal annealing which is an equilibrium process, a nonequilibrium annealing technique, *i.e.* flash lamp annealing at a pulse length of 20 ms, was also used by us [134]. For an intermediate light power, the implantation-induced surface defects could be removed without creation of secondary phases within the implanted region. However, there is still no detectable ferromagnetic coupling between these dispersed Fe ions.

Moreover, currently the absence of ferromagnetism in transition metal doped ZnO is a universal problem. Several groups have shown that transition metal ions, *e.g.* Fe [135], Mn [34, 135], and Co [34, 35, 135], are substitutional inside ZnO. However, no ferromagnetism could be observed due to the possible reason of the lack of p-type conductivity.

4.4 Summary and Conclusions

(1) In general, a combination of SR-XRD, ZFC/FC magnetization and element specific spectroscopy measurements is a reliable approach to clarify the observed magnetism in DMS materials.

(2) By correlating the structural and magnetic properties of all investigated samples, it is clear that ferromagnetism is only observed when α-Fe (or $ZnFe_2O_4$) NCs are present. In as-implanted and 823 K annealed samples, dispersed Fe^{2+} and Fe^{3+} are the predominant charge states. However, they are not ferromagnetically coupled.

(3) α-Fe (bcc) NCs are not crystallographically oriented inside ZnO matrix. However, fcc-$ZnFe_2O_4$ NCs formed after annealing at 1073 K are epitaxially embedded in ZnO. This is due to the crystalline symmetry. Hexagonal ZnO crystals are six-fold symmetric, while α-Fe is four-fold symmetric. Fcc-$ZnFe_2O_4$ is also six-fold symmetric viewed along [111] direction.

(4) The magnetic properties of these Fe NCs were carefully investigated regarding their memory effect and magnetic anisotropy. A memory effect is observed in the temperature dependent magnetization measurement, which is induced by the different relaxation times originating from the different grain sizes of the Fe nanoparticles, and consequently different anisotropy energy barriers. The in-plane magnetic anisotropy could be due to the shape effect.

(5) The phase separation, *i.e.* the formation of metallic Fe, depends on the initial state of the host materials, namely the carrier and/or the defect concentrations. The n-type carriers could facilitate the self-organization of metallic Fe NCs.

(6) The next question is directed to the magnetical activation of the diluted ionic Fe in ZnO. The realization of p-type doping for ZnO could be the solution.

(7) Additionally, the ion beam synthesis of Zn-ferrites is demonstrated. $ZnFe_2O_4$ nanoparticles are crystallographically oriented inside ZnO. These $ZnFe_2O_4$ nanocrystals show a hysteretic behavior upon magnetization reversal at 5 K

Chapter 5

Co and Ni implanted ZnO: crystallographically oriented precipitates

In this chapter, a thorough characterization of the structural and magnetic properties of Co and Ni implanted ZnO single crystals will be presented. The measurements reveal that Co or Ni nanocrystals (NCs) are the major contribution to the measured ferromagnetism. Already in the as-implanted samples, Co or Ni NCs have formed, and they exhibit superparamagnetic properties. The Co or Ni NCs are crystallographically oriented with respect to the ZnO matrix. Their magnetic properties, *e.g.* the anisotropy and the superparamagnetic blocking temperature can be tuned by annealing. We discuss the magnetic anisotropy of Ni NCs embedded in ZnO concerning the strain anisotropy.

This chapter is organized as follows. In section 5.1 the procedure of sample preparation will be described briefly. Then the results will be presented in two sections. In section 5.2 we will focus on the as-implanted samples, and discuss the orientation, the superparamagnetism, the magnetic anisotropy of Co and Ni NCs. In section 5.3 we will describe the structure and magnetism evolution due to high vacuum annealing. Finally in section 5.4 we discuss the origin of the magnetic-anisotropy for the oriented Co, Ni NCs system, and the possible formation of Co/CoO and Ni/NiO core/shell structures upon annealing at 923 K.

This chapter has been published in following papers: (1) J. Appl. Phys. **100**, 114304 (2006); and (2) Phys. Rev. B **77**, 035209 (2008).

5.1 Experiments

Commercial ZnO single crystals grown by the hydrothermal method were implanted with Co or Ni ions at 623 K with a fluence ranging from 0.8×10^{16} cm^{-2} to 8×10^{16} cm^{-2}. The implantation energy was 180 keV, which resulted in a projected range of $R_P = 89 \pm 29$ nm, and a maximum atomic concentration from $\sim$1% to $\sim$10% (TRIM code [95]). Thermal

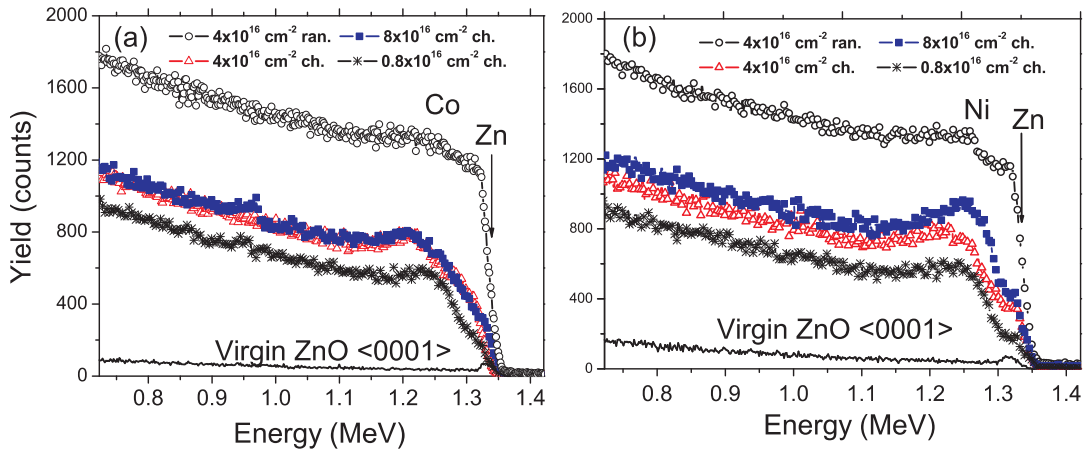

Figure 5.1: RBS random (ran.) and channeling (ch.) spectra, (a) Co implanted ZnO, and (b) Ni implanted ZnO (the fluence for Co and Ni ions is indicated). The yield of channeling spectra progressively decreases with increasing fluence.

annealing was performed in a high vacuum ($<10^{-6}$ mbar) furnace from 823 K to 1073 K.

For a detailed analysis we applied different techniques: (1) Rutherford backscattering/channeling (RBS/C), (2) Synchrotron radiation x-ray diffraction (SR-XRD) and conventional XRD, and (3) SQUID-magnetometry. In chapter 3, one can find the descriptions on these techniques.

5.2 As-implanted samples

5.2.1 ZnO lattice damage upon implantation

RBS/C is used to check the lattice damage after implantation. Figure 5.1 shows RBS/C spectra for different fluences. The arrow labelled Zn indicates the energy for backscattering from surface Zn atoms. The implanted Co or Ni ions cannot be detected for the very low fluence (0.8×10^{16} cm^{-2}, not shown). However, they are more pronounced as a hump in the random spectrum for a larger fluence of 4×10^{16} cm^{-2} and 8×10^{16} cm^{-2} (not shown). The humps (between channel 650 to 750) in the channeling spectra mainly originate from the lattice disordering due to implantation. As expected, χ_{min} increases with increasing fluence (see Table 5.1). Note that the highest Co fluence induced comparable lattice damage with the middle fluence, and less than the damage created by the same fluence of Ni. The reason could be a dopant specific self-annealing process [100]. RBS/C measurements also reveal that the ZnO is a hard material with respect to irradiation. The host material still partly remains in a crystalline state after irradiation with Co and Ni ions up to a fluence of 8×10^{16} cm^{-2} (χ_{min} of 59% and 69%, respectively).

5.2.2 Crystallographically oriented Co and Ni NCs

SR-XRD is used to identify the precipitates in ZnO after Co or Ni implantation. Figure 5.2 shows the XRD 2θ-θ scans for all samples implanted with different fluences. At a low

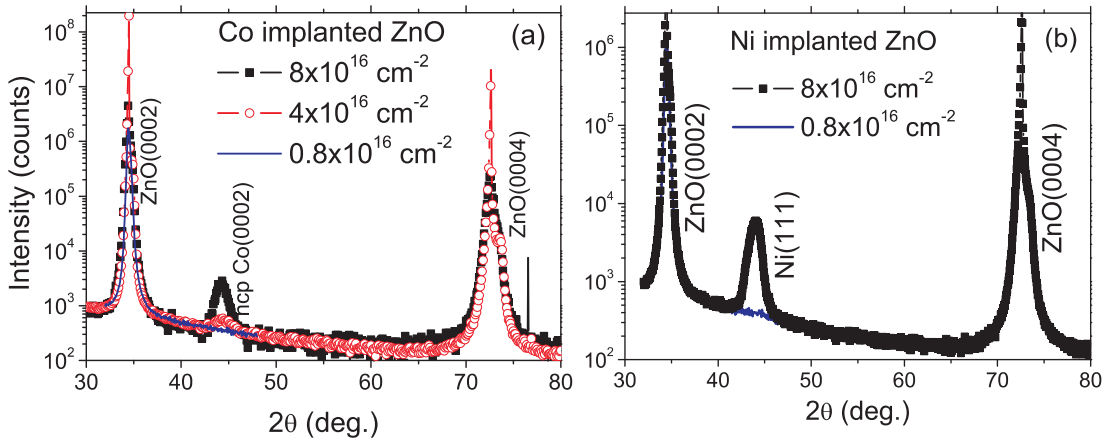

Figure 5.2: SR-XRD 2θ-θ scan revealing the existence of Co or Ni precipitates in (a) Co implanted ZnO, and (b) Ni implanted ZnO.

fluence (0.8×10^{16} cm^{-2}), no crystalline Co or Ni NCs could be detected. At a fluence of 4×10^{16} cm^{-2} the hcp-Co(0002) (or fcc-Co(111)) and Ni(111) peak appear, respectively, and grow with increasing fluence. The full width at half maximum (FWHM) of the Co or Ni peak decreased with fluence, indicating the growth of the average diameter of these NCs (table 5.1). The crystallite size is calculated using the Scherrer formula [105],

$$d = 0.9\lambda/(\beta \cdot \cos\theta), \tag{5.1}$$

where λ is the wavelength of the x-ray, θ the Bragg angle, and β the FWHM of 2θ in radians.

Note that there is only one peak for Co or Ni detectable, which indicates that the crystallites of Co or Ni are highly oriented with respect to the host matrix. The surface orientation is hcp-Co(0001)(or fcc-Co(111))$\|$ZnO(0001) and fcc-Ni(111)$\|$ZnO(0001), respectively.

The Co hcp structure only differs in the stacking from the fcc one. Since the Bragg angles (θ) for hcp-Co(0002) (θ=22.38°) and fcc-Co(111) (θ=22.12°) are rather close to each other, it is difficult to assign these peaks in Figure 5.2(a) to hcp-Co or fcc-Co. A ϕ-scan or pole figure on one of the diffraction planes not parallel with the sample surface (i.e. tilted by an angle χ from sample surface) helps to identify hcp or fcc-Co NCs and also reveals the crystallographical orientation relationship. By this approach, we find that only hcp-Co is present in the as-implanted samples. Figure 5.3 (a) and (b) show the pole figure of hcp-Co(10$\underline{1}$1) and Ni(200), respectively. The radial coordinate is the angle (χ) by which the surface is tilted out of the diffraction plane. The azimuthal coordinate (ϕ) is the angle of rotation about the surface normal. The pole figure shows poles of hcp-Co(10$\underline{1}$1) at $\chi\sim$61.9°, and Ni(200) at $\chi\sim$54.8°, respectively. Both exhibit a sixfold symmetry. Since ZnO(10$\underline{1}$2) and hcp-Co(10$\underline{1}$1) have similar Bragg angle, the poles of ZnO(10$\underline{1}$2) also show up at $\chi\sim$42.8° with much more intensities. The results are consistent with the theoretical Co(10$\underline{1}$1) pole figure viewed along [0001], and Ni(200) pole figure viewed along [111] direction, respectively. Therefore, we can conclude that these Co and Ni NCs are crystallographically oriented with respect to the ZnO matrix. The in-plane orientation relationship is hcp-Co[10$\underline{1}$0]$\|$ZnO[10$\underline{1}$0], and Ni[112]$\|$ZnO[10$\underline{1}$0],

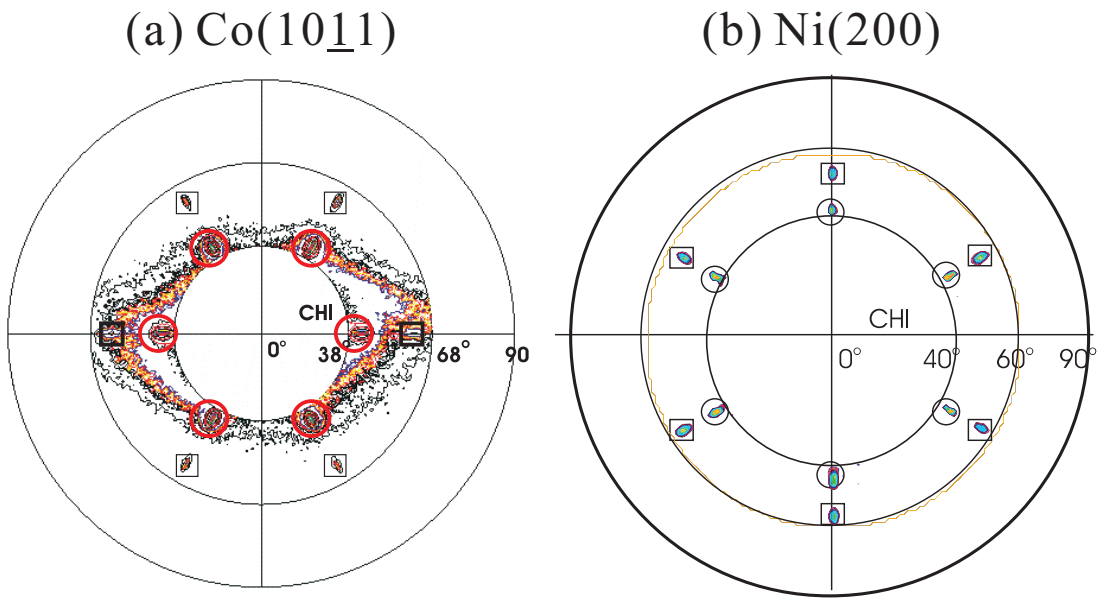

Figure 5.3: XRD Pole figure revealing the crystallographical orientation relationship between Co/Ni NCs and ZnO matrix, (a) Co(10$\underline{1}$1) (in square) together with the tail of ZnO(10$\underline{1}$2) (in circle); (b) Ni(200) (in square) together with the tail of ZnO(10$\underline{1}$2) (in circle).

Table 5.1: Structural and magnetic properties for Co and Ni-implanted ZnO with different fluence. Metallic Co/Ni fraction corresponds to the percentage of metallic Co/Ni compared with all implanted Co/Ni.

Fluence (cm^{-2})	χ_{min} (RBS/C)	Cryst. size (nm) (XRD)	Saturation [a] (μ_B/Co(Ni))	Metallic fraction	Coercivity[a] (Oe)	T_B (K)	Cryst. size[b] (nm)
Co: 0.8×10^{16}	44%	-	-	-	-	-	
Co: 4×10^{16}	54%	5	0.29 (5 K)	17%	1400 (5 K)	45	4.3
Co: 8×10^{16}	57%	8	0.44 (5 K)	26%	1400 (5 K)	300	8.1
Ni: 0.8×10^{16}	45%	-	0.05 (10 K)	8%	10 (10 K)	≤ 5	< 9.4
Ni: 4×10^{16}	57%	6	0.16 (10 K)	27%	30 (10 K)	16	14
Ni: 8×10^{16}	69%	8	0.22 (10 K)	37%	120 (10 K)	70	23

[a] Saturation magnetization, refer to the easy axis.
[b] Calculation from the average blocking temperature by Eq. 2.2.

respectively. Due to the hexagonal structure of Co and sixfold symmetry of Ni viewed along [111] direction, it is not difficult to understand their crystallographical orientation onto hexagonal-ZnO.

Conventional XRD (CXRD) reveals similar results as SR-XRD (from the Ni fluence of 4×10^{16} cm^{-2}, Ni NCs start to form). However, CXRD fails to detect Fe NCs in ZnO [71], where Fe NCs are not well oriented like the case of Ni in ZnO. The peak intensity in XRD is proportional to the diffraction volume, *i.e.* the number of diffraction planes which are parallel to each other. For a 2θ-θ scan, the crystallographic orientation results in much more diffraction volume than the random orientation. Therefore, the highly ordered orientation of NCs make them easier to be detected. As expected, Co NCs are also detectable in the CXRD measurement (not shown).

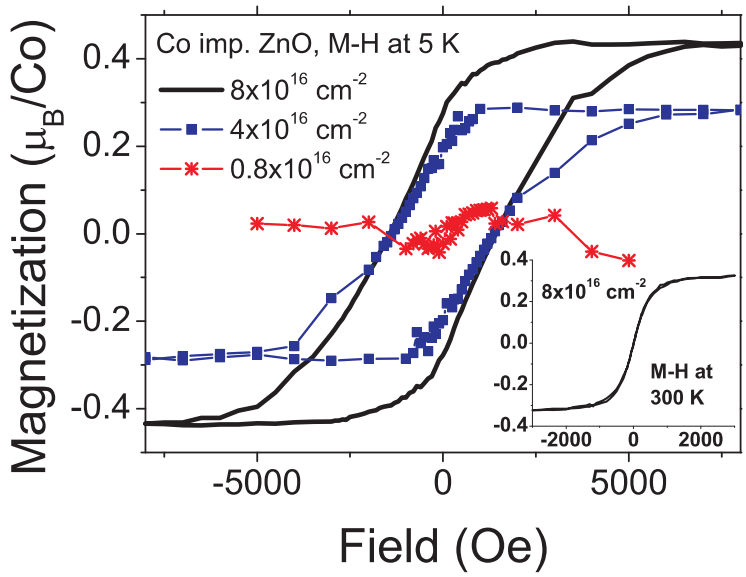

Figure 5.4: Hysteresis loops measured at 5 K for Co implanted ZnO with different fluences. For the fluence of 0.8×10^{16} cm^{-2}, only a half loop was measured. Inset: Hysteresis loop measured at 300 K for the sample with the highest fluence.

5.2.3 Magnetic properties of Co and Ni NCs

The magnetic properties of Co and Ni implanted ZnO were measured by SQUID magnetometery with the field parallel and perpendicular to the sample surface. Co implanted samples exhibit a hard axis parallel to the sample surface, while the easy axis is perpendicular to the surface. For Ni-implanted samples, the anisotropy directions are vice versa. In this section, we investigate the superparamagnetism of the implanted ZnO samples and their magnetic anisotropy.

Superparamagnetic Co and Ni NCs

Figure 5.4 shows the magnetization versus field reversal (M-H) measured at 5 K with the field applied perpendicular to the sample surface (along ZnO[0001]). A hysteretic behavior is observed for the high-fluence implanted samples. A saturation behavior is also observed at 300 K for the sample with the highest fluence (Figure 5.4 inset). However, neither coercivity nor remanence can be observed at 300 K. This is a strong indication for the superparamagnetism of a magnetic nanoparticle system. Knowing the formation of hcp-Co from XRD, it is reasonable to assume that hcp-Co NCs are responsible for the magnetic behavior. For bulk hcp-Co crystals, the magnetic moment is 1.7 μ_B/Co at 0 K. Assuming the same value for Co NCs, around 16% and 26% of implanted Co ions are in the metallic state for the fluence of $4\times$ and 8×10^{16} cm^{-2}, respectively. Similar results are observed for Ni implanted ZnO [76].

Temperature dependent magnetization with H= 50 Oe was measured after ZFC and FC to confirm the superparamagnetism (Figure 5.5). For the magnetic samples, a distinct difference in ZFC/FC curves is observed. ZFC curves show a gradual increase (deblocking)

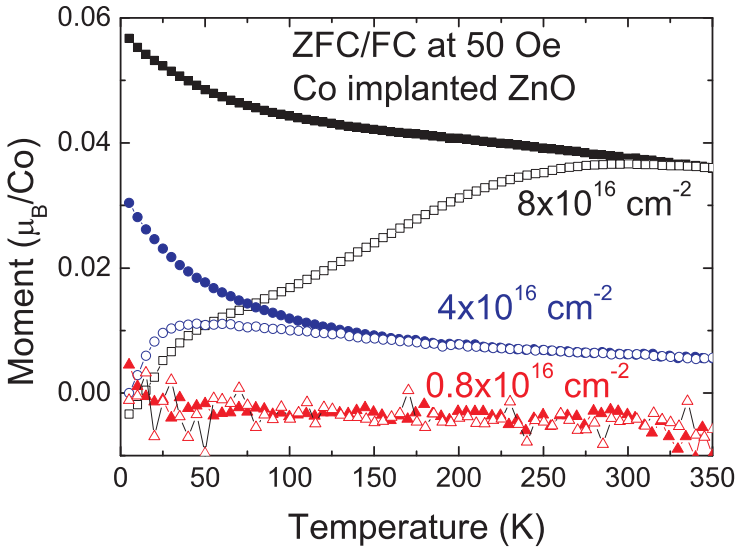

Figure 5.5: Magnetization curves at 50 Oe after ZFC/FC for the Co implanted ZnO. With increasing fluence, the Co NCs is growing in size, resulting in a higher blocking temperature.

at low temperature, and reach a broad peak, while FC curves continue to increase with decreasing temperature. The broad peaks in ZFC curves are due to the size distribution of Co NCs. In this thesis, the temperature at the maximum of the ZFC curve is taken as the average blocking temperature (later referred as T_B). The ZFC/FC curves are general characteristics of magnetic nanoparticle systems with a broad size distribution [109]. T_B increases with the fluence, *i.e.* the size of nanoparticles. Table 5.1 lists the average size of Co NCs calculated by Eq. 5.1 (XRD) and Eq. 2.2 (SQUID). They are in a good agreement although there is also a size distribution in Co NCs [79]. The ZFC/FC magnetization was also measured for Ni implanted samples [76]. Comparing with Co, Ni has a much lower anisotropy energy density. For similar sizes of Ni NCs, the blocking temperature is therefore much lower than that of Co. Table 5.1 lists the average size of Ni NCs calculated by Eq. 5.1 (XRD) and Eq. 2.2 (SQUID). Although the trend is the same for both calculations, the values from SQUID are much larger than the ones from XRD data. One reason could be the anisotropy energy density is underestimated by assuming the magneto-crystalline anisotropy constant. Another reason could be due to the large size distribution of Ni NCs, *i.e.* T_B is overestimated by taking the temperature at the maximum of the ZFC curve [79].

Magnetic anisotropy

M-H loops were also measured for selective samples with Co fluence of 8×10^{16} cm^{-2} with the field both perpendicular and parallel to the sample surface. Figure 5.6(a) shows the comparison of the magnetization along ZnO[10$\underline{1}$0] and [0001] at 300 K. Figure 5.6(c) shows the orientation relationship between hcp-Co and ZnO, and the measurement geometry. Obviously Co[0001] is the easy axis, the same as a bulk hcp-Co crystal. The intersection of both curves gives an effective anisotropy field of 3000 Oe. At 5 K, the magnetic anisotropy is the

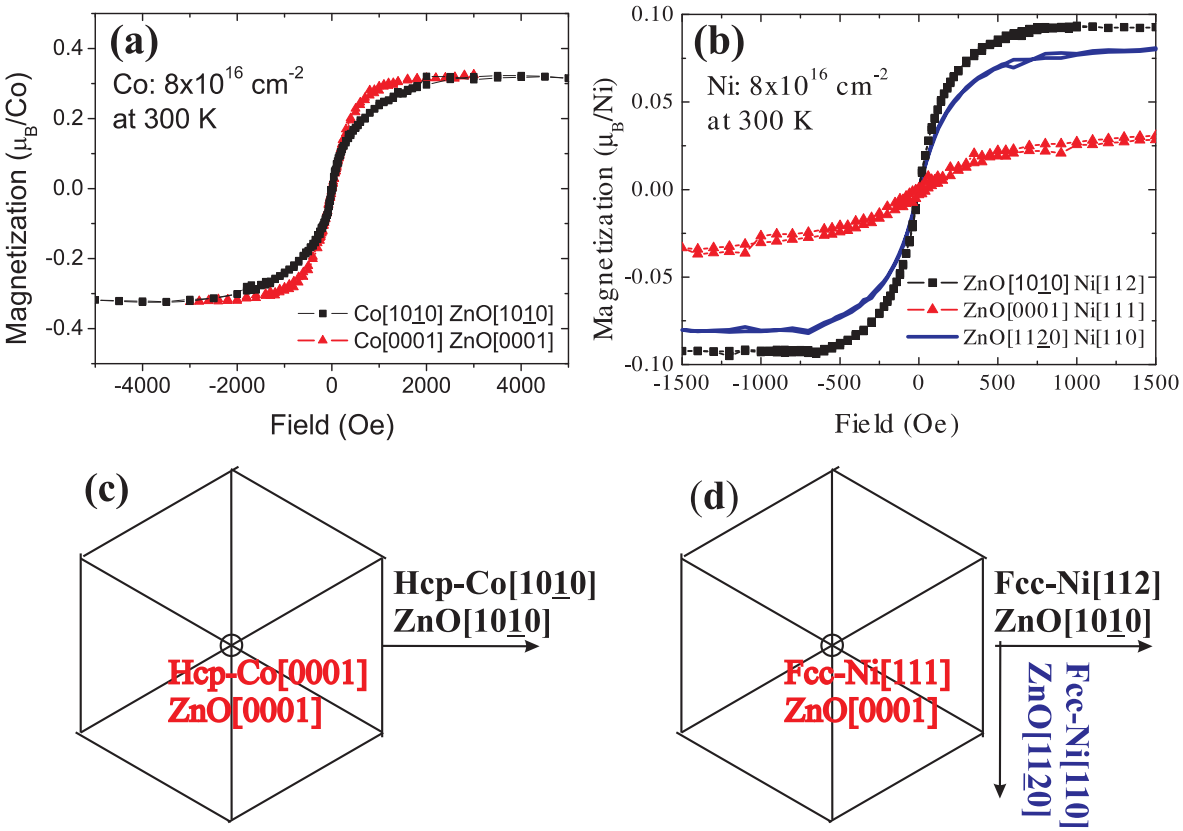

Figure 5.6: Hysteresis loops measured with the field along ZnO[0001] (out-of-plane) and [10$\bar{1}$0] (in-plane) for Co/Ni implanted ZnO with the fluence of 8×10^{16} cm^{-2} measured at 300 K, (a) Co implanted ZnO; and (b) Ni implanted ZnO. (c) and (d) show the schematic geometry for magnetization measurements.

same (not shown), and the coercivity of the easy axis is around 1400 Oe. The ratio between remanence and saturation magnetization is around 60%. Figure 5.6(b) shows the same measurement of Ni implanted ZnO, while (d) shows the orientation relationship between fcc-Ni and ZnO, and the measurement geometry. In contrast to bulk Ni where [111] is the easy axis, the easy axis is Ni[112] and the hard axis is Ni[111]. Moreover, as shown in Figure 5.6(b), another in-plane direction Ni[110] is also an easy axis. Within the applied field, the magnetization curve along the hard axis does not intersect with that along the easy axis. The effective anisotropy field is much larger than 1500 Oe. That means that there are other contributions to the anisotropy dominating over the crystalline magnetic anisotropy. This will be discussed in section 5.4.

In the work by Norton *et al.* [74], epitaxial Co nanocrystals have been observed in Co implanted ZnO single crystals. The nanocrystal size is estimated to be ~3.5 nm, which is below the superparamagnetic limit at room temperature. Therefore the ferromagnetism above 300 K is very possible due to Co substitution onto the Zn site in the ZnO matrix. In our case, the measured superparamagnetism is well explained by the presence of Co and Ni nanocrystals. The formation of metallic nanocrystals already in the as-implanted state is due to the elevated implantation temperature (623 K), which facilities the precipitation process.

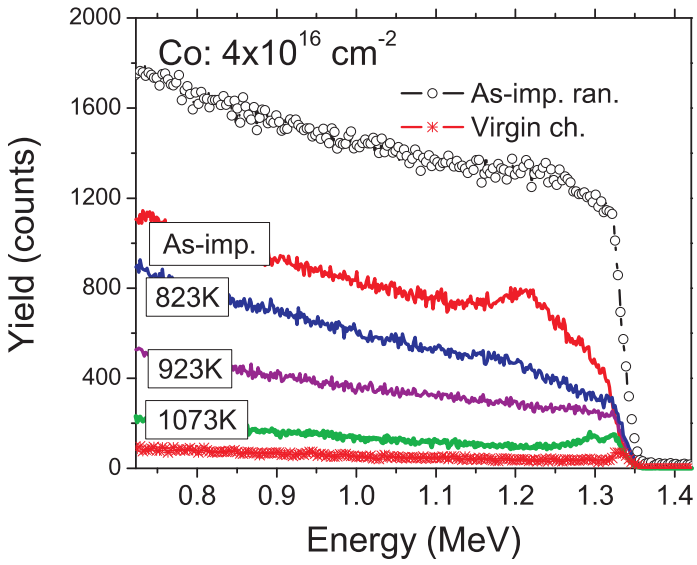

Figure 5.7: RBS random (ran.) and channeling (ch.) spectra for Co implanted ZnO with a fluence of 4×10^{16} cm^{-2} after thermal annealing at different temperatures. The lattice damage induced by implantation is progressively reduced by increasing annealing temperature.

Implantation at low temperatures (*e.g.* 253 K) prohibits precipitation, however results in non-magnetism in our case, *e.g.* Fe implanted ZnO [136].

5.3 The effect of post-annealing

The post-annealing was performed in high vacuum at temperatures ranging from 823 K to 1073 K for 15 min. The samples to be annealed were selected according to the SQUID measurement capability, namely the temperature range from 1.8 to 400 K. Due to the higher anisotropy energy of Co, T_B in the ZFC curve of the highest fluence is already 300 K in the as-implanted state (see Figure 5.5). The annealing is expected to increase the size of Co NCs, and consequently increase T_B in the ZFC curve, which will exceed the temperature range of the SQUID magnetometery. Therefore, the sample implanted with the middle Co fluence was chosen. For Ni the highest implantation fluence was chosen.

5.3.1 Lattice recovery

As shown in Figure 5.1, ion implantation substantially induces lattice damage of ZnO crystals. Here we show that this damage can be partially recovered by post-annealing.

Figure 5.7 shows the RBS/C spectra for the sample implanted with a Co fluence of 4×10^{16} cm^{-2}. The annealing temperatures are given in the figure. With increasing annealing temperature, the channeling spectra indicate that the lattice disorder of ZnO progressively decreases. After annealing to 1073 K, the channeling spectrum is almost comparable with the virgin ZnO. Similar RBS/C results are observed for Ni-implanted ZnO upon annealing (not shown).

Table 5.2: Structural and magnetic properties for Co and Ni-implanted ZnO with different fluence. Metallic Co/Ni fraction corresponds to the percentage of metallic Co/Ni compared with all implanted Co/Ni.

Sample	Peak area (XRD)	Cryst. size (nm) (XRD)	Saturation [a] (μ_B/Co(Ni))	Metallic fraction	Coercivity[a] (Oe)	T_B (K)	Cryst. size[b] (nm)
Co: As-imp.	380	5	0.29	17%	1400	45	4.3
Co: 823K ann.	8330	-	0.36	21%	250	80	5.2
Co: 923K ann.	1400	10	0.32	19%	450	330	8.3
Co: 1073K ann.	0	-	-	-	-	-	-
Ni: As-imp.	7312	8	0.22	37%	230	70	< 9.4
Ni: 823K ann.	6590	9	0.22	37%	200	80	14
Ni: 923K ann.	750	7	0.18	30%	220	-	-
Ni: 1073K ann.	0	-	-	-	-	-	-

[a]Saturation magnetization, refer to the easy axis magnetization at 5 K.
[b]Calculation from the average blocking temperature by Eq. 2.2.

5.3.2 Evolution of structural properties

Figure 5.8(a) shows the development of Co NCs upon thermal annealing. The peak area and crystallite size calculated using the Scherrer formula [105] are compared in table I. A broad scan (the inset of Figure 5.8(a)) reveals only one peak from Co besides the ZnO peaks. An XRD ϕ-scan has been used to distinguish between hcp- and fcc-Co (Figure 5.9(a)). We find only hcp-Co in the as-implanted sample and the sample annealed at 923 K, while both fcc- and hcp-Co are present in the sample annealed at 823 K. The broad peak in Figure 5.8(a) (823 K ann.) is a superposition of hcp-Co(0002) and fcc-Co(111). The crystallographical orientation relationship between Co NCs and ZnO is hcp-Co(0001)[10$\underline{1}$0]//ZnO(0001)[10$\underline{1}$0]//fcc-Co(111)[112]. With this orientation, the 2θ-θ scans for hcp-Co(10$\underline{1}$1) and fcc-Co(200) are expected with a skew geometry [137] at one of the azimuthal position (*e.g.* at ϕ=0) as shown in Figure 5.9(b) and (c), respectively. Note that the peak area of Co in Figure 5.8, which is an approximate measure of the amount of Co NCs, increases drastically after 823 K annealing, while decreases after 923 K annealing. It is reasonable to attribute this change to the formation and disappearance of fcc-Co. The fcc-Co is probably oxidized to the amorphous CoO after 923 K annealing, while finally all Co NCs are oxidized to an amorphous state after annealing at 1073 K.

For Ni implanted ZnO, the structure evolution upon annealing is similar as shown in Figure 5.8(b). The peak area and the crystallite size is listed in table 5.2. The mild temperature annealing (823 K) only slightly increases the grain size of Ni. The annealing at 923 K drastically decreases the peak area, while the grain size also decreases. Note that there is a significant shift in the Ni(111) peak (labelled by dash lines), which indicates the relaxation of lattice strain. The Ni NCs could be completely oxidized to amorphous state after 1073 K annealing.

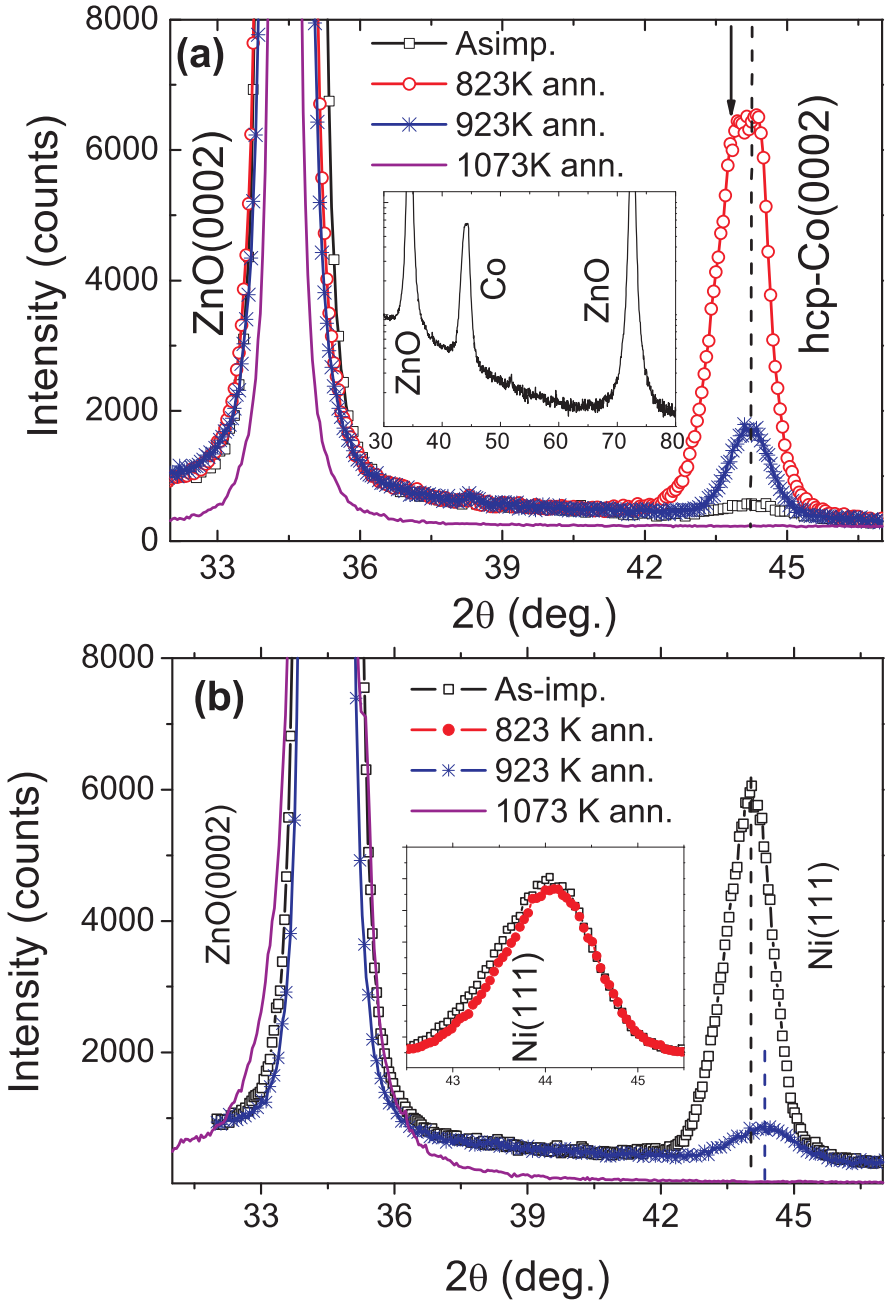

Figure 5.8: XRD 2θ-θ scans: (a) Co implanted ZnO crystals with different annealing temperature. The wide range XRD pattern for one of the samples (inset) reveals that no other crystalline phase (e.g. CoO) could be detected. The arrow points the peak shoulder coming from fcc-Co(111) diffraction in the sample of 823 K ann. (b) Ni implanted ZnO crystals with different annealing temperature. The pattern of the sample annealed at 823 K is not shown to avoid overlapping. The inset shows a comparison between as-implanted and 823 K annealed samples.

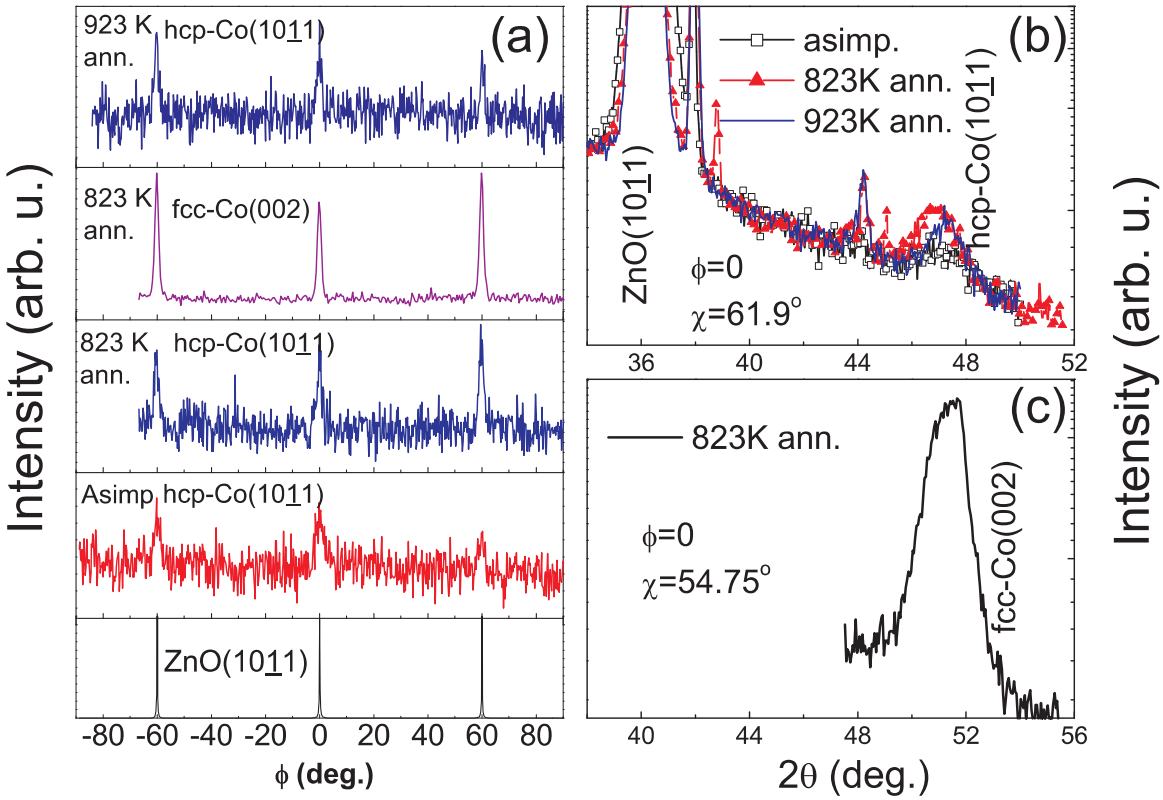

Figure 5.9: (a) XRD ϕ-scans for hcp-Co(10$\underline{1}$1) (θ=23.78° and $\chi\sim$61.9°), fcc-Co(002) (θ=25.76° and $\chi\sim$54.8°) and ZnO(10$\underline{1}$1) (θ=18.13° and $\chi\sim$61.6°) reveal the in-plane orient relationship for Co NCs respect to ZnO; (b) 2θ-θ scans for ZnO(10$\underline{1}$1) and hcp-Co(10$\underline{1}$1), those small sharp peaks are from artificial noise in the measurements; (c) 2θ-θ scan for fcc-Co(002).

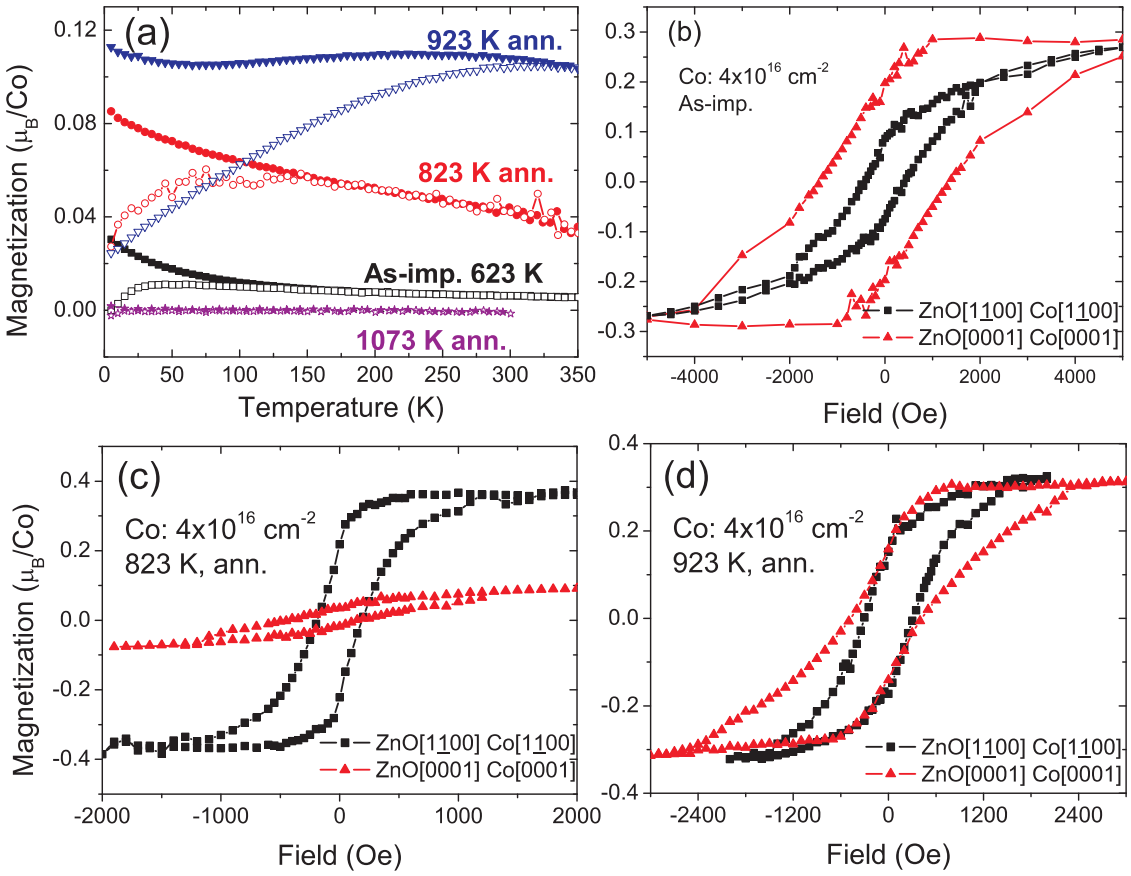

Figure 5.10: (a) ZFC/FC magnetization curves at 50 Oe for the samples after implantation and annealing at different temperatures. Solid symbols are FC curves, while open symbols are ZFC curves; (b)-(d) M-H curves measured at 5 K for all samples: along ZnO[10$\bar{1}$0]||hcp-Co[10$\bar{1}$0]||fcc-Co[112] (solid symbols) and ZnO[0001]||hcp-Co[0001]||fcc-Co[111] (open symbols). Implantation or annealing temperature is shown.

5.3.3 Evolution of magnetic properties

The structural phase transformation of Co NCs results in different magnetic properties as revealed by SQUID. Figure 5.10(a) shows the ZFC/FC magnetization curves for all samples annealed at different temperatures. Obviously, except the sample annealed at 1073 K, ZFC curves show a gradual increase (deblocking) at low temperature, and reach a maximum at a temperature of T_B (shown in table 5.2), while FC curves continue to increase with decreasing temperature. No significant magnetization response is detected for the sample annealed at 1073 K. Note that T_B increases drastically above 330 K after annealing at 923 K. However Jacobsohn *et al.* [138] reported a much lower T_B (250 K) of hcp Co NCs with similar grain size (∼10 nm). The higher T_B could be due to some other anisotropy energy, which stablized the superparamagnetism at higher temperature. This will be discussed in section 5.4.

Hysteresis loops were measured for all samples in both parallel (ZnO[10$\bar{1}$0]||hcp-Co[10$\bar{1}$0] ||fcc-Co[112]) and perpendicular (ZnO[0001]||hcp-Co[0001]||fcc-Co[111]) directions. Figures 5.10(b)-(d) reveal that the anisotropy and coercivity can be tuned by different annealing procedures. The as-implanted sample only consists of hcp Co NCs, which persist the bulk-like

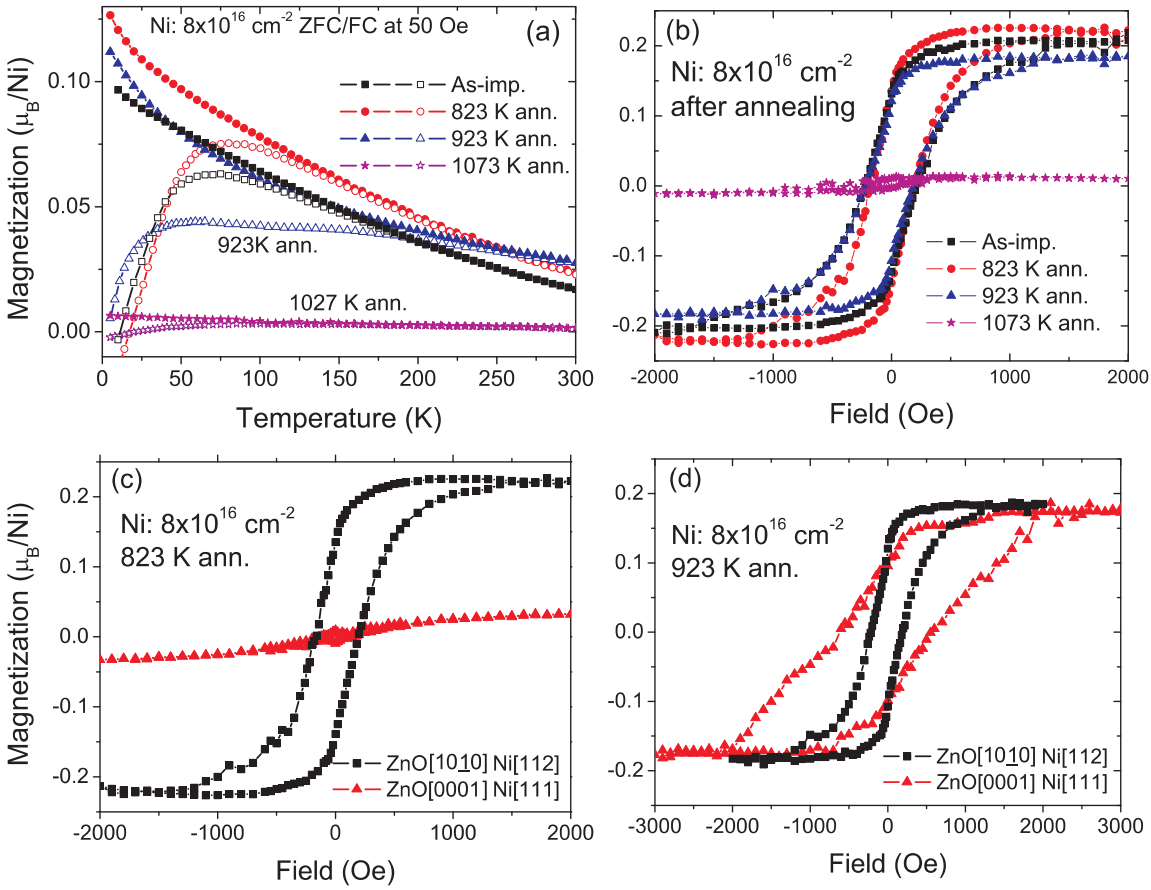

Figure 5.11: (a) ZFC/FC magnetization curves at 50 Oe for the samples after implantation and annealing at different temperatures. Solid symbols are FC curves, while open symbols are ZFC curves; (b) M-H curves measured at 5 K for all samples along ZnO[10$\bar{1}$0]||fcc-Ni[112]; (c) and (d) M-H curves measured at 5 K for all samples along ZnO[10$\bar{1}$0]||fcc-Ni[112] (solid symbols) and ZnO[0001]||fcc-Co[111] (open symbols) after 823 K and 923 K annealing, respectively. Implantation or annealing temperature is shown.

anisotropy along [0001] direction with a high coercivity (Figure 5.10(b)). The sample annealed at 823 K mainly consists of fcc-Co with easy axis is along the fcc-Co[112] direction (Figure 5.10(c)). After annealing at 923 K, the sample shows an easy axis both along hcp-Co[10$\bar{1}$0] and hcp-Co[0001], but a higher coercivity along the latter direction. The magnetic properties of different samples are listed in table 5.2.

Figure 5.11 shows the magnetic properties of Ni implanted ZnO upon annealing. As expected, the 823 K annealing increases T_B in the ZFC curve due to the increase of crystallite size. However upon annealing at 923 K, the shape of ZFC magnetization curve deviates from others. There is no real maximum, but a broad plateau. The formation of Ni/NiO core/shell structures could introduce an exchange coupling, which contributes to another anisotropy energy. This will be discussed in the following section.

5.4 Discussion

5.4.1 Magnetic anisotropy of Co and Ni NCs

As shown before, the magnetic anisotropy of Ni NCs embedded in ZnO is drastically different from bulk Ni. For bulk Ni, the magnetocrystalline anisotropy constant of K_1 is -5.7$\times 10^3$ J m^{-3} at 300 K. The [111] direction is the easy axis. For a single magnetic NC, the magnetocrystalline, shape, and magnetoelastic anisotropy have to be considered.

In principle, a uniformly magnetized single domain spherical particle has no shape anisotropy, because the demagnetizing factors are isotropic in all directions. However, a nonspherical sample will be easier to be magnetized along a long axis than along a short one. The FWHM of the Ni peak in XRD 2θ-θ scans is a measure of the crystallite size. Along the Ni[111] direction, the crystallite size is estimated to be around 8 nm. For the in-plane direction, the crystallite size could be estimated by measuring a diffraction plane not parallel to the sample surface. We chose the Ni(200) diffraction plane. Figure 5.12 shows the comparison of the normalized Ni(111) and (200) peaks. Actually the Ni(200) is broader than (111), which means that the crystallite size along the in-plane direction is even smaller than in the [111] direction. Therefore, the shape anisotropy is not the key reason to induce the easy axis along the in-plane direction.

Now we consider the strain anisotropy. This kind of anisotropy is often described by a magnetoelastic energy term

$$k_{magnetoelastic} = -\frac{3}{2}\lambda_S \sigma \cos^2 \phi \tag{5.2}$$

where λ_S is the magnetostriction constant, σ the stress, and ϕ the angle between magnetization and the strain tensor axis [129]. The strain ϵ along the [111] direction of our Ni NCs can be calculated according to XRD measurements.

The lattice spacing is given by Bragg's law:

$$2d_{exp} \sin\theta = \lambda \tag{5.3}$$

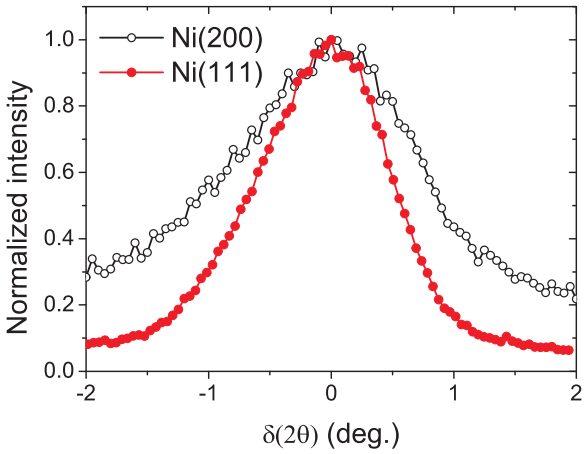

Figure 5.12: XRD 2θ-θ scan of Ni(200) and Ni(111).

Table 5.3: Comparison of magnetic-anisotropy energy density: magnetocrystalline K_1, magnetoelastic K_{ME}. λ_S is the magnetostriction coefficient, E the Young modulus, ϵ the elastic strain, and σ the stress ($\sigma = E\epsilon$).

Nanocrystals	k_{ME} (10^3 Jm^{-3})	k_1 (10^3 Jm^{-3})[a]	λ_S[a]	E (GPa)[a]	ϵ	σ (Gpa)
Ni (As-imp.)	54	-5.7	-24×10^{-6}	200	0.011	2.2
Ni (823 K ann.)	50	-5.7	-24×10^{-6}	200	0.010	2.0
Ni (923 K ann.)	25	-5.7	-24×10^{-6}	200	0.005	1.0
hcp-Co (As-imp.)	125	500	-5.5×10^{-5}	209	0.011	2.3

[a]Data from Refs.[139][140].

where d_{exp} is the lattice spacing, θ the Bragg angle, and λ=0.154 nm the wavelength of the X-rays. θ is obtained from Figure 5.2. The strain is defined as follows

$$\epsilon = (d_{exp} - d)/d \tag{5.4}$$

where d is the theoretical lattice spacing for bulk Ni or Co.

The magnetoelastic anisotropy constant is calculated using the approach and parameters of refs. [139][140] (see table 5.3). For Ni NCs, the magnetoelastic anisotropy is one order higher than the magnetocrystalline anisotropy. Therefore the magnetoelastic anisotropy energy dominates the total anisotropy energy. This finding demonstrates the possibility to tune the magnetic properties by embedding magnetic NCs in different host matrix. The annealing at 823 K does not change the strain status significantly. After annealing up to 923 K, the elastic strain is partially released. However, the magnetoelastic anisotropy energy is still much higher than the magnetocrystalline one. Note the anisotropy change in Figure 5.11(d) after 923 K annealing by comparing with the 823 K annealing. There could be another anisotropy source after 923 K annealing, which will be discussed in section 5.4.2.

For hcp-Co, the magnetocrystalline anisotropy constant is very large, and it is difficult to be dominated by other anisotropy energy contribution (as shown in Table 5.3). Therefore the hcp-Co NCs in the as-implanted sample still keep the bulk like anisotropy behavior.

However, the annealing at 823 K resulted in coexistence of fcc-Co and hcp-Co NCs. Since fcc-Co is a meta-stable state, only limited magnetic and mechanic data are available. Therefore we will not discuss its magnetoelastic anisotropy energy. After annealing at 923 K, hcp-Co is the only phase, and the elastic strain is not significantly changed compared with the as-implanted state (see Figure 5.8(a)). However, the anisotropy is obviously changed. Like the Ni case, there could be another anisotropy source, which will be discussed in section 5.4.2.

5.4.2 Annealing at 923 K

After annealing at 923 K, the magnetic properties, namely ZFC/FC magnetization, and magnetic anisotropy, are changed significantly compared with other samples. For the Co case, T_B in the ZFC curve increases drastically, while the FC curve does not decrease monotonically with increasing temperature. For the Ni case, there is a broad plateau in the ZFC curve.

One explanation for the higher T_B is the increase and broadening of the Co crystallite size. Jacobson *et al.* calculated the ZFC curves by varying different parameters, including the size distribution [84]. It is found that a slight broadening can result in a very broad and high ZFC curve. This can well explain the ZFC magnetization, but not the FC magnetization. Moreover the drastic changes in coercivity, and magnetic anisotropy cannot be explained in such an approach. In addition, Table 5.2 lists the comparison of the XRD peak area and the magnetization upon annealing. Note that the XRD peak area decreases drastically by almost one order after 923 K annealing, which indicates the decrease of the amount of the Co or Ni NCs, however the saturation magnetization only decreases slightly.

Another explanation is related to other anisotropic energy contributions. Skumryev *et al.* have found that the exchange coupling between Co NCs and their CoO shells drastically increases the blocking temperature [141]. In our XRD measurement, the amount of metallic Co and Ni decreases after annealing at 923 K, which is very probably due to the oxidation. Therefore we could assume the formation of a Co/CoO core/shell structure in our sample, and the exchange coupling increases the blocking temperature. The exchange coupling is further confirmed by the vertical shift of the magnetization loop (Figure 5.13). The loop-curve is shifted along the magnetization axis after cooling from 350 K in an applied field.

The vertical shift of the magnetization loop is an evidence for the presence of an interfacial interaction between an antiferromagnet (AFM) and a ferromagnet (FM) [142], *i.e.* the hcp Co NCs are surrounded by CoO, which is amorphous, and therefore cannot be detected by XRD. Dobrynin *et al.* [142] presented a model to discuss the exchange coupling of nanoscaled Co/CoO core/shell structures. Below a critical size (12 nm) of Co cores, the interfacial exchange energy is larger than both the Zeeman energy of FM and the anisotropy energy of the AFM due to a large surface-to-volume ratio of NCs, and consequently some spins in the FM part can be frozen by the AFM part, leading to a vertical shift along the magnetization axis after field cooling. This model well explains our Co/CoO system with an average diameter

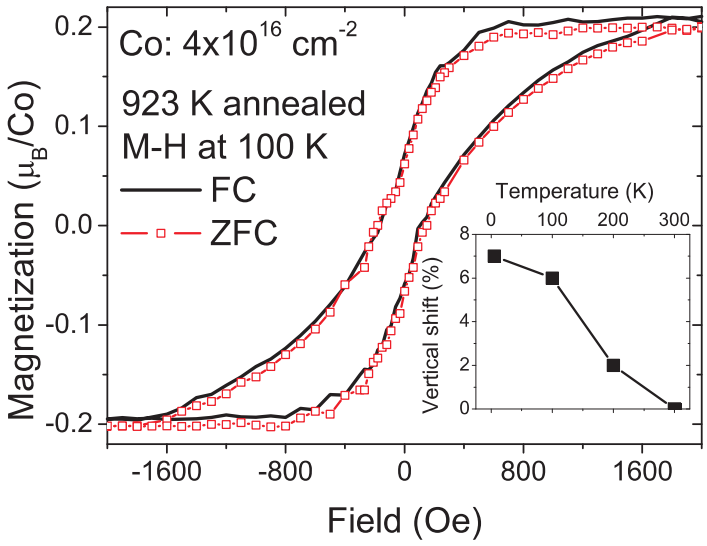

Figure 5.13: The sample annealed at 923 K shows a small vertical shift along the magnetization axis after field cooling (H=2000 Oe) due to the exchange coupling between FM and AFM materials. The field is along ZnO[0001] direction. The inset shows the temperature dependence of the vertical shift.

of 10 nm for Co NCs. The vertical shift of the magnetization loop decreases with increasing temperature and disappears at a temperature between 200 and 300 K. This is consistent with the Néel temperature of 290 K for CoO [141]. Such a vertical shift is also observed in the FC-loop measured along ZnO[10$\underline{1}$0]||hcp-Co[10$\underline{1}$0] (in-plane) (not shown).

For the Ni implanted sample annealed at 923 K, the hysteresis loop was also measured under both ZFC and FC conditions (not shown). A similar shift along the magnetization axis is observed. Therefore we would assume the formation of a Co/CoO (Ni/NiO) core/shell structure. The exchange coupling between Co (Ni) and CoO (NiO) contributes another anisotropy energy. This explains the high blocking temperature and the change in magnetic-anisotropy after annealing at 923 K. Obviously a detailed investigation using transmission electron microscopy could be directly prove this assumption.

Note that for both of cases, the magnetization is only slightly decreased after annealing at 923 K. This is controversial with the drastic decrease of the diffraction intensity (see Figure 5.8). One possible reason is the formation of small Co or Ni nanocrystals due to annealing. As shown in Table 5.1, only around 10-40% of Co or Ni form as metallic nanocrystals and others remain as dispersed ones. Annealing at 923 K, on one hand, oxidized some metallic nanocrystals partially, on the other hand, could induce the gettering of dispersed Co and Ni and result in small metallic nanocrystals. Below a critical size, nanocrystals are non-detectable by XRD. Another reason could be that only a thin shell of Co or Ni nanocrystals transforms into oxides, which results in the invisibility of oxides in XRD even they are crystalline. Obviously a detailed investigation using transmission electron microscopy or other more sensitive techniques should be performed to clarify this controversy.

5.5 Conclusions

A thorough characterization of the structural and magnetic properties has been presented on Co and Ni implanted ZnO single crystals. The results by SR-XRD and SQUID magnetometery correlate well with each other. The major conclusions are summarized as follows.

(1) Co or Ni NCs have been formed in ZnO upon ion implantation. Their crystalline sizes, generally below 10 nm, increase with increasing fluence. From several to 37% percent of implanted Co or Ni is in metallic states, while the remaining could be diluted into ZnO matrix. The Co or Ni NCs are the origin of the measured ferromagnetism.

(2) The Co and Ni NCs are crystallographically oriented with respect to the ZnO host matrix. The orientation relationship is as follows: hcp-Co(0001)[10$\underline{1}$0]||ZnO(0001)[10$\underline{1}$0], and Ni(111)[112]||ZnO(0001)[10$\underline{1}$0]. This well ordered structure of NCs could result in a rather smooth interface between them and the ZnO host, and makes the hybrid of ferromagnetic NCs and semiconductors promising for spintronics functionality.

(3) Magnetic anisotropy is observed for Co or Ni NCs in ZnO. Especially for the Ni NCs, the anisotropy is different from the bulk crystals. The extra anisotropy energy is attributed to the lattice strain impressed from the host matrix. This opens a route to artificially tune the magnetic properties of nanoparticles by selecting substrate materials.

(4) The structure and magnetic properties of Co or Ni NCs embedded inside ZnO can be tuned by post-annealing. For the Co case, 823 K annealing results in the co-existence of fcc-Co and hcp-Co. The magnetic anisotropy is changed from out-of-plane to in-plane. Annealing at 923 K could have partially oxidized metallic Co and Ni, and results in Co/CoO (Ni/NiO) core/shell structures. After annealing at 1073 K, no Co or Ni NCs can be detectable, at the same time, the samples shows no pronounced ferromagnetism down to 5 K.

Chapter 6

Suppression of secondary phase formation

Formation of secondary phases is one of the major problems in diluted magnetic semiconductor (DMS) creation. In this chapter we show possibilities to avoid such phases in Fe implanted and post-annealed ZnO(0001) single crystals.

This chapter has been published in following papers: (1) Appl. Phys. Lett., **91**, 062107 (2007); (2) J. Appl. Phys. **103**, 043901 (2008); and (3) J. Phys. D: Appl. Phys. **41**, 105011 (2008).

6.1 Experiments

The formation of secondary phases in ZnO single crystals implant-doped with Fe can be avoided by annealing the crystals prior to implantation. Moreover, weak ferromagnetic properties are introduced that are not related to ordinary superparamagnetic nanoparticles. The following sample set has been prepared from hydrothermal, commercial epi-polished ZnO(0001) substrates purchased from Crystec:
1. "non pre" - non pre-annealed, *i.e.* as-polished
2. "O_2 pre"- annealed in flowing O_2 at 1273 K for 15 min
3. "vac. pre" - Annealed in high vacuum (base pressure $< 1\times10^{-6}$ mbar) at 1273 K for 15 min

O_2-annealing at high temperatures is known to reduce lattice damage in the near surface region of ZnO [143, 144]. Treatment 3, *i.e.* vacuum annealing, was chosen due to the formation of free charge carriers from point defects. Such defects are expected to open a path for indirect ferromagnetic coupling of the dispersed TM ions via s-d coupling as has been reported earlier [23, 54]. Please note that mild vacuum annealing around 873 K usually introduces both O-vacancies and Zn-interstitials. Under high temperature annealing, however, defects like Zn vacancies or Zn interstitials are not stable, *i.e.* the defects are dominated by oxygen vacancies after such treatment. Following a recent paper [145], the latter

do not mediate FM while the former two do. Thus, our approach, besides the suppression of secondary phases, would give a confirmation of such different effects of various kinds of defects. For further processing our samples were subjected to ^{57}Fe ion implantation. The implantation energy was 80 keV at an incident angle of 7° yielding a projected range of 38 nm and a straggling of 17 nm (TRIM [95]). The implanted Fe-fluence of 2×10^{16} cm^{-2} yielded a maximum atomic concentration of 5 %. In order to avoid magnetic secondary phases already in the as-implanted samples, a low implantation temperature of 253 K was used [71]. Post-implantation annealing for lattice recovery was performed in high vacuum at a temperature of 823 K for 15 minutes. For that purpose, the samples were mounted at a Mo holder of high purity that was cleaned by heating cycles at 1073 K for 2 h. The heater below the holder was manufactured purely from tungsten isolated by Al_2O_3 ceramics. The base pressure was below 1×10^{-6} mbar. The particular parameters for the post-annealing have been chosen to avoid long-range diffusion and oxidation of the implanted Fe as have been observed earlier for higher annealing temperatures [102]. For a detailed analysis we applied different techniques.

- X-ray diffraction (XRD) using a Siemens D 5005 diffractometer
- Rutherford backscattering/channeling (RBS/C)
- Atomic force microscopy (AFM)
- Conversion electron Mößbauer spectroscopy (CEMS) at room temperature
- X-ray absorption spectroscopy (XAS) performed at beamline 8.0.1 of the Advanced Light Source (ALS) in Berkeley
- SQUID-magnetometry.

6.2 Results and discussion

Structural analysis was performed by means of RBS/C, AFM, and XRD, respectively. RBS/C revealed no significant change of the crystallinity after pre-annealing. In contrast, AFM (not shown) reveals pronounced changes of the crystal surface morphology. After O_2 pre-annealing the root mean square surface roughness (Rq) of the ZnO sample slightly increases from 0.23 nm to 0.27 nm and regularily oriented steps appear. The latter is an indication for surface recrystallization [144]. Vacuum pre-annealing, in contrast, yielded a surface roughness of 23 nm. While after implantation a slight increase of Rq is detectable, post-annealing does not change Rq significantly for any of the samples. Thus, our post-annealing treatment appears to be mild enough in order to not substantially change the condition of the ZnO crystals while simultaneously producing partial recovery of the introduced lattice damage. The latter statement is supported by RBS/C for both the pre-annealed and non pre-annealed crystals: Fig. 6.1(a) shows a decrease of the minimum channeling yield (χ_{min})

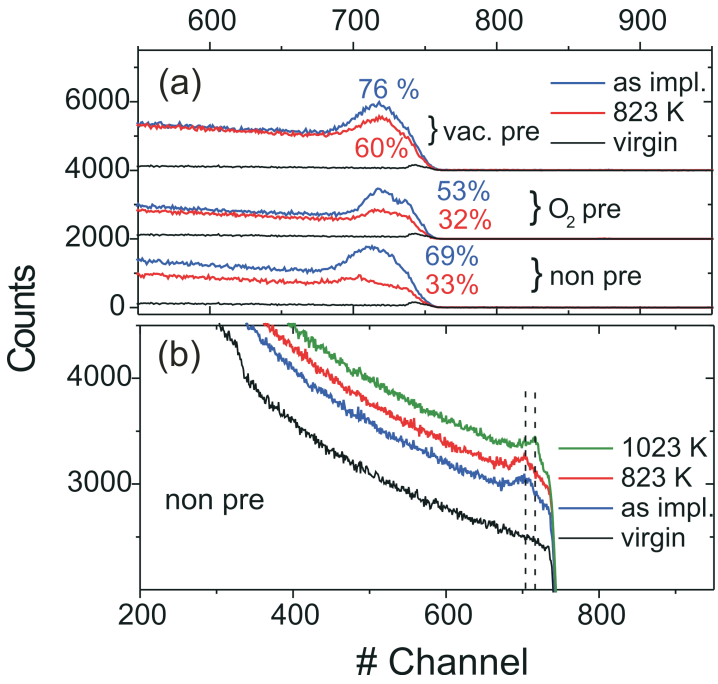

Figure 6.1: (a) Channeling RBS-spectra for the as-implanted and post-annealed ZnO single crystals. Pre-implantation annealing is indicated. (b) Exemplary random spectra for the non pre-annealed crystal for different post-annealing (y-shifted for better visibility). Although Fe has a smaller nuclear mass than Zn, it is visible in the random spectra as a bump. Please note that mild annealing at 823 K does not shift the Fe profile, annealing at 1023 K, however, does. The spectra have been shifted in y-direction for better clarity.

with post-annealing. The drop is largest for the non pre-annealed crystal and smallest for the vacuum pre-annealed sample. The lowest χ_{min} is achieved for the O_2 pre-annealed crystal. χ_{min} directly reflects the crystalline homogeneity, *i.e.* while an amorphous sample shows a min of 100 %, a perfect single crystalline sample exhibits 1-2 %. Diffusion of the implanted Fe due to the post-annealing could be ruled out by means of RBS/C random spectra (Fig. 6.1(b)). Bumps originating from the implanted Fe are visible in all samples that allow us to investigate the potential diffusion of the Fe inside ZnO. Upon post-annealing at 823 K these bumps do not shift, *i.e.* Fe is not segregating over larger distances. In order to check the potential formation of secondary phases, XRD of the implanted and post-annealed samples has been performed. The presence of secondary phases has only been observed for the non pre-annealed and post-annealed crystal (not shown), *i.e.* α-Fe nanoparticles of 7 nm mean diameter, as calculated using the Scherrer formula [105].

In order to further prove that metallic nanoparticle formation has been avoided by our pre-annealing, element specific spectroscopy was applied in order to determine the charge states of the implanted Fe. We performed CEMS and XAS, respectively. While CEMS is more bulk sensitive, XAS recording the total electron yield (TEY) is rather sensitive to the surface region. The combination of both methods thus leads to a complete picture of the charge states of the implanted Fe. Moreover, CEMS allows simultaneous detection of electronic and magnetic properties at the implanted Fe. The CEM spectra of the as-implanted samples

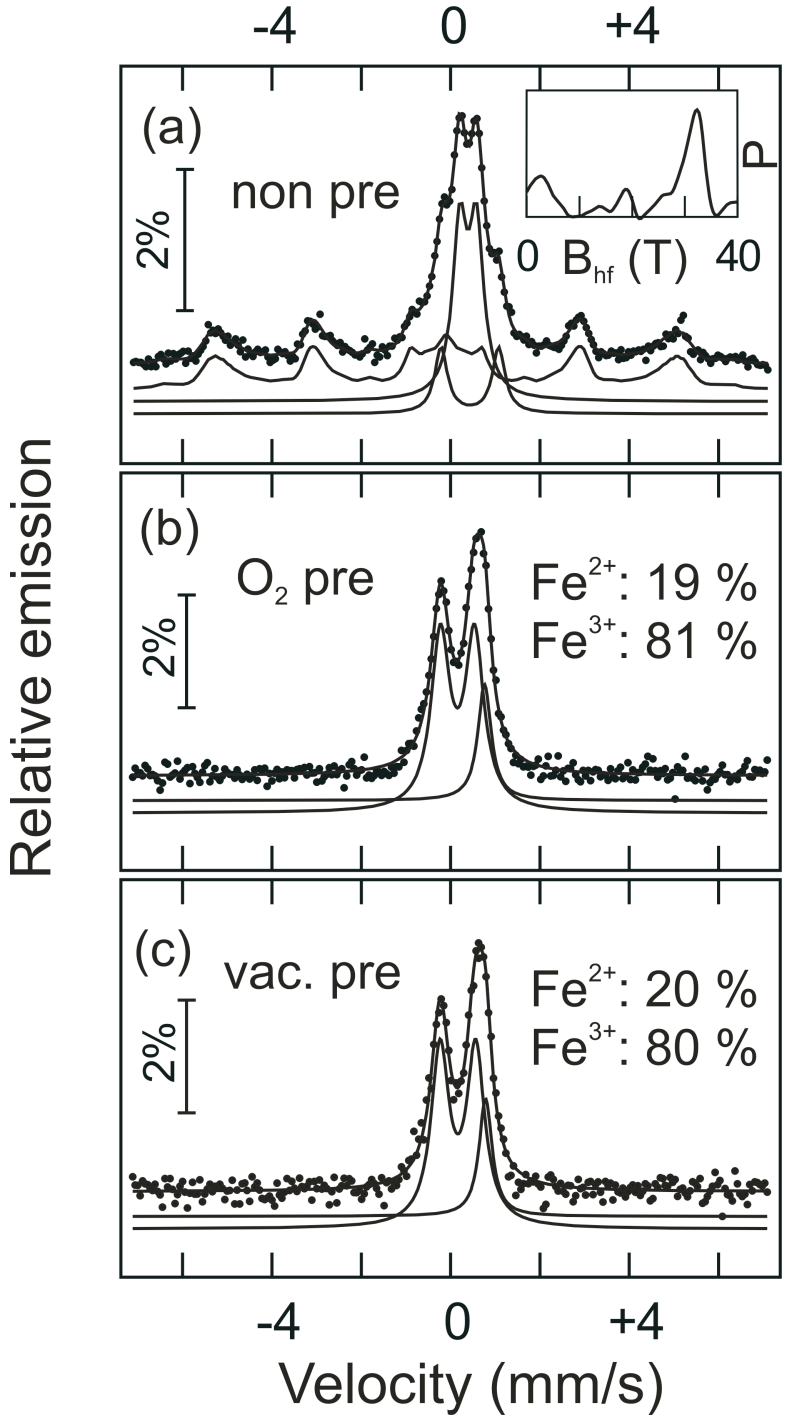

Figure 6.2: CEM spectra of the Fe implanted and post-annealed ZnO single crystals. (a) CEM spectrum of non pre-annealed sample. A pronounced magnetic hyperfine field distribution is visible. The main peak in the magnetic distribution (inset) corresponds to the known value for α-Fe. The ratio between Fe^0 and Fe^{3+} is 48%:52%. (b) and (c) CEM spectra of the pre-annealed samples. The ratio between the valence states is indicated.

(not shown) look similar exhibiting mixed Fe^{2+} and Fe^{3+} valence states. No magnetic sextet was detected for any of the samples. Thus, they are comparable to the ones from earlier work [71, 134]. Fig. 6.2 shows CEM spectra for all the post-annealed samples. Only the non pre-annealed one shows a magnetic hyperfine field with an isomer shift equal to that of α-Fe. The value of the magnetic hyperfine field is distributed over a wide range so that it can be assumed that a large part of the Fe ions also does not contribute to the full magnetic bulk moment. In contrast, no indication for metallic Fe exists in the spectra of the pre-annealed samples. They show similar hyperfine parameters dominated by a Fe^{3+} doublet. Please note that after post-annealing Fe^{2+} states are only present for the pre-annealed crystals but not for the non pre-annealed ones. The XAS measurements of the post-annealed samples yield similar results (Fig. 6.3), *i.e.* ionic 2+ and 3+ valence states in all of the crystals with a contribution from metallic Fe solely in the non pre-annealed sample. Also for the O_2 pre-annealed sample we find a good coincidence between the Mößbauer and XAS data. *I.e.*, from the multiplet structure of the corresponding Fe L2,3 XAS (third spectrum from the top in Fig. 6.3) one can conclude that Fe^{3+} ions are dominating in this sample, whereas the presence of some Fe^{2+} ions can not be excluded. We find quite good agreement with the Fe L2,3 XAS of Fe_3O_4 comprising 66.7% Fe^{3+} and 33.3% of Fe^{2+} ions. On the other hand we find some differences in detail in case of the vacuum pre-annealed crystal. The bulk sensitive CEMS suggests a very similar valence state as for the O_2 pre-annealed sample, dominated by Fe^{3+} ions. The more surface sensitive XAS also suggests a mixed valence state, however involving some more Fe^{2+} than Fe^{3+} states. The XAS of the O_2 pre-annealed sample is very similar to that of a Sr_2FeMoO_6 sample which has been found to have a mixed iron valence state involving around 65% Fe^{2+} ions and 35% Fe^{3+} ions . This discrepancy could be explained by different spatial distributions of the charge states for the different pre-annealing conditions. From the above mentioned analysis we conclude that nanoparticle formation is suppressed by either pre-annealing method. The mechanism of the suppression is not yet completely clear. One possibility is the removal of such kinds of defects which can act as nucleation centers, *e.g.* open volume defects [134], due to the pre-annealing.

Pronounced ferromagnetic properties were found only for the non pre-annealed crystal after post-annealing (Fig. 6.4(a)). Magnetization reversal and zero field cooled / field cooled temperature dependence (ZFC-FC) recorded at 50 Oe show typical behavior of superparamagnetic nanoparticles with size distribution. The non pre-annealed and the O_2 pre-annealed crystals do not show magnetic ordering for the as-implanted state (not shown). In contrast, after post-annealing a weak separation between ZFC and FC curve up to 70 K can be observed for the O_2 pre-annealed crystal and up to a temperature above 250 K for the vacuum pre-annealed crystal (Fig. 6.4 (b-c)). Please note the pecularity that weak ferromagnetic properties occur already after implantation for the vacuum pre-annealed crystal (Fig. 6.4(d)). The saturation magnetization extracted from hysteresis loops recorded at 5 K is below 0.025 μ_B per implanted Fe ion. The magnetic moment per implanted Fe ion is

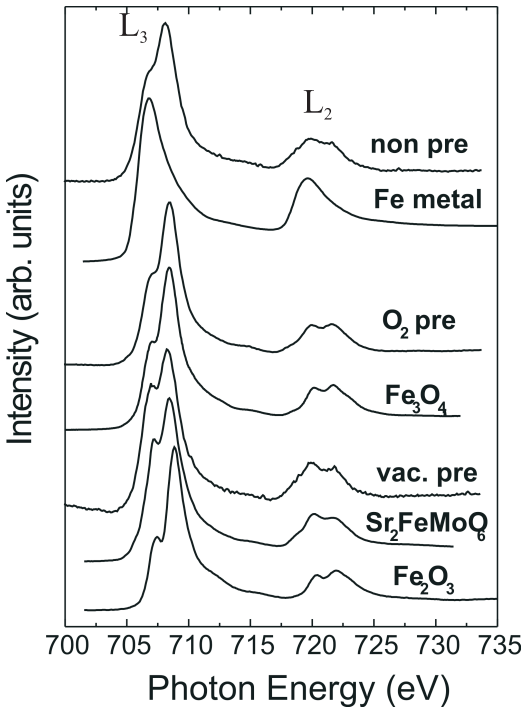

Figure 6.3: Fe L2,3 XAS of the non pre-annealed sample (top) and the two pre-annealed samples (3rd and 5th from the top) after implantation and post-annealing. Several measurements on reference compounds, namely Fe metal, Fe_2O_3, Fe_3O_4, and Sr_2FeMoO_6 are also shown for comparison (see Refs. [146, 147]). Please note that only the non-pre annealed sample shows pronounced contributions from metallic Fe.

about 20 times smaller as compared to the as-purchased crystal after post-annealing. The shape of the ZFC-FC curve indicates ferromagnetic regions with rather inhomogeneous Fe content as can be expected from the low temperature implantation. Post-annealing, however smoothes the ZFC-FC curve. The origin of the observed ferromagnetic properties is rather speculative at this point. First, due to the very low saturation magnetization, we conclude that a large amount of defects created by high temperature annealing, likely oxygen vacancies, do not lead to pronounced ferromagnetic coupling of the implanted Fe ions. Second, it is rather likely that implantation or implantation plus mild post annealing creates such defects, which ferromagnetically couple at least a small part of the implanted Fe ions. It is noteworthy that possible sources for ferromagnetic properties other than ordinary superparamagnetic nanoparticles or DMS are reported in the literature for similar systems. Among them are exotic, *i.e.* low-dimensional secondary phases [148] or purely defect induced magnetic moments [149]. Thus, further effort has to be applied in order to really clarify the origin of the ferromagnetism in TM doped ZnO.

In order to directly clarify, whether Fe is chemically involved in the magnetic properties, we applied XMCD measurements to sample Fe(10%):ZnO within max. 2 weeks after the SQUID magnetometry. Figs. 6.5 shows the corresponding XMCD spectra recorded at 20 K. Apparently, no evidence for ferromagnetic order assigned to the implanted Fe could be detected. The slight difference (b) does likely not originate from an XMCD effect as was

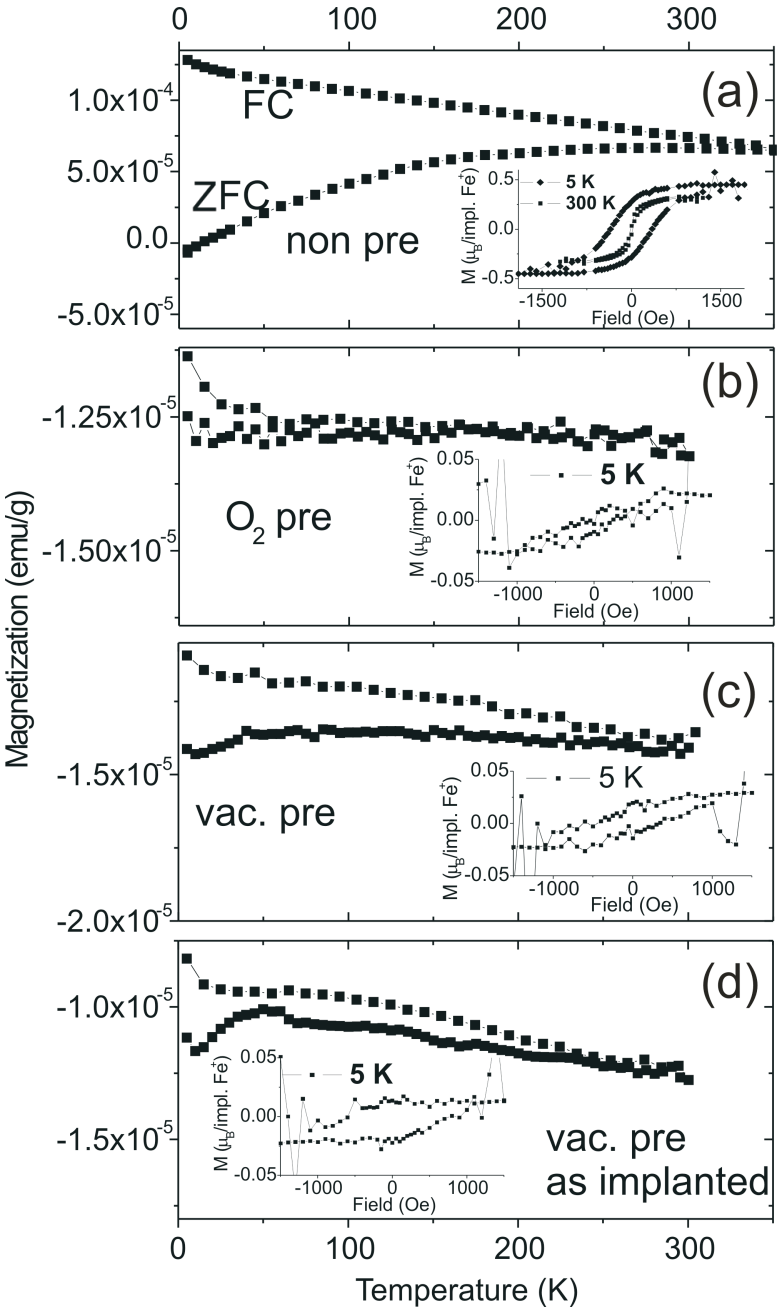

Figure 6.4: ZFC-FC magnetization vs. time measurements and magnetic hysteresis loops (insets) for all the Fe implanted and post-annealed ZnO single crystals (a-c). For the insets the diamagnetic background was subtracted. (a) non pre-annealed sample exhibiting -Fe nanoparticles (b)-(c) O_2- and vac. pre-annealed crystals after post-annealing. (d) As-implanted vac. pre-annealed crystal (for comparison). The latter 3 show a weak separation in the ZFC-FC and very low saturation moment in the hysteresis loops as compared to (a). For (c) and (d) the thermomagnetic irreversibility temperature is above 250-300 K.

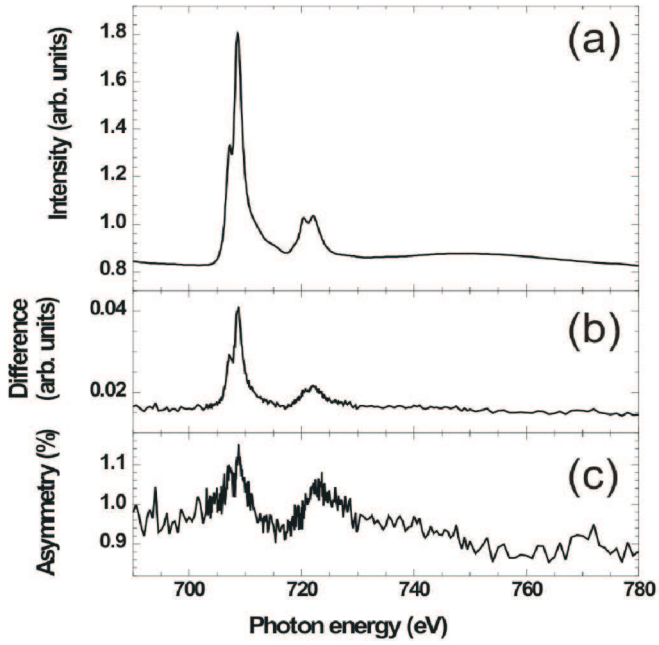

Figure 6.5: (a) Sum, (b) difference, and (c) asymmetry of the magnetic field dependent total electron yield (TEY) induced by application of circularly polarized soft X-rays to the surface of sample Fe(10%):ZnO. The magnetic field was switched between +2 kOe and -2 kOe for every datapoint. The X-ray incindence angle was 60° to the sample surface normal.

found by recording the spectrum at opposite photon helicity (not shown). It most likely originates from non-symmetric effects described by E. Goering *et al.* for TEY-measurements in applied magnetic fields [150].

6.3 Conclusion

In summary we demonstrated that pre-annealing of commercial ZnO(0001) single crystals in both, flowing O_2 or vacuum suppresses metallic secondary phase formation after Fe implantation and mild post-annealing in contrast to the non pre-annealed crystals. Weak ferromagnetic properties are induced in the vacuum and O_2 pre-annealed crystals. Also, in our previous publication [71], a weak ferromagnetic response has been detected in the sample implanted with low Fe fluence at low implantation temperature (253 K), These properties cannot be associated with ordinary superparamagnetic nanoparticles. By XMCD measurement, we have not found any evidence for the chemical involvement of Fe in the magnetic properties. Therefore, all these weak ferromagnetic response in ZnO could be purely defects related. Moreover, this finding is in consistent with the presentations in 52th Magnetism and Magnetic Materials conference (Nov. 2007, Tampa, Florida) by M. J. Coey and by S. Chambers.

This pre-annealing approach has also been checked in Ni implanted ZnO. The formation of metallic Ni nanoclusters is also sufficiently suppressed.

Chapter 7

Transition metal implanted Si and TiO_2

In the study of transition metal implanted ZnO, the correlation between structural and magnetic properties has been established, therefore the origin of the observed ferromagnetism is clarified. The same approach was used to investigate other semiconductors, namely Si and TiO_2, implanted with transition metal. The magnetic precipitates and their thermal stability have been clarified. In this chapter, a brief description of the study of Mn-implanted Si and TM-implanted TiO_2 (TM=Fe, Co, Ni) will be given, while the details have been reported in Refs. [151, 152]

This chapter has been published in following papers: (1) Phys. Rev. B, **75**, 085203 (2007); and (2) J. Appl. Phys. **103**, 083907 (2008).

7.1 Mn-implanted Si

7.1.1 Introduction

Comparing with compound semiconductors, Si-based DMS would be preferable due to the availability of high quality Si in large sizes at relatively low costs. More importantly, the fabrication of Si-based DMS is compatible with the mature microelectronics technique. Very recently, Bolduc *et al.* [153] have reported room temperature ferromagnetism of Mn-ion implanted Si. The ferromagnetic coupling was believed to be carrier-mediated. However, the high-resolution structural characterization of the investigated Si:Mn systems was rather limited. Generally Mn silicides are easily formed. *E.g.* if Mn is deposited on Si, an epitaxial MnSi is formed [154]. Also transition metal (*i.e.* Co and Ni) implantation into Si can easily lead to silicides [155]. Therefore a careful characterization of the Mn doped Si samples has to be carried out in order to clarify the origin of the ferromagnetism, *i.e.* the formation of nanoparticles or a DMS system. For this purpose, RBS/channeling, transmission electron microscopy (TEM) and synchrotron radiation x-ray diffraction (SR-XRD) are used to clarify

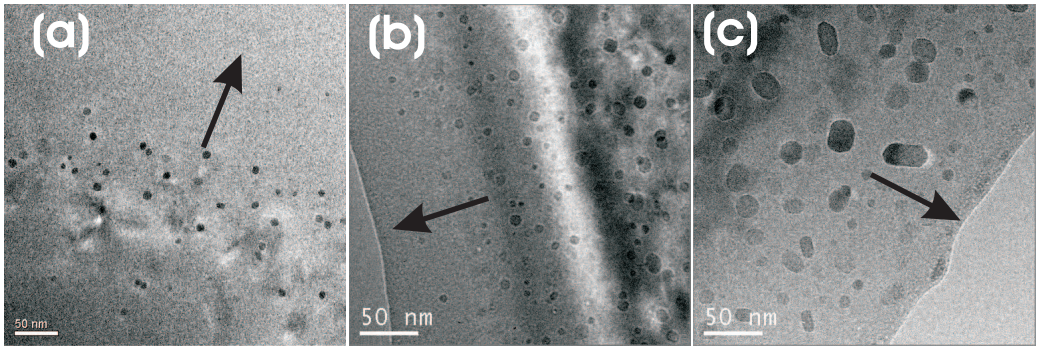

Figure 7.1: TEM-overview images show the implantation induced damage and nano-sized precipitates after RTA: (a) 1×10^{15}, (b) 1×10^{16} and (c) 5×10^{16} cm^{-2}. The nano-sized precipitates are visible as spot-like contrast, and they are growing with increasing fluence. The arrow marks the direction towards the sample surface.

the possible origin of the ferromagnetism in Mn-implanted Si.

7.1.2 Experiments

The Mn-implanted Si samples were prepared from commercially available, Czochralski grown single-crystal Si(001) wafers, which were p-type doped with a B concentration of 1.2×10^{19} cm^{-3}. Mn^+ ions were implanted at an energy of 300 keV with fluences of 1×10^{15}, 1×10^{16} and 5×10^{16} cm^{-2} (later referred as 1E15, 1E16 and 5E16, respectively), which corresponds to Mn peak concentrations of 0.08, 0.8 and 4 at %, respectively. After implantation, rapid thermal annealing (RTA) was performed at a temperature of 800°C for 5 min in a forming gas of N_2.

7.1.3 Results and discussion

Figure 7.1 shows typical TEM-overview images at lower magnification of samples after RTA treatment. Nano-sized precipitates are unambiguously found in all annealed samples with different fluence. They exhibit mean diameters of 5 nm for a fluence of 1E15, 10 nm for 1E16, and 20 nm for 5E16. In addition, grazing incidence X-ray diffraction (GIXRD) was performed in order to confirm the formation of Mn-silicide. Figure 7.2 shows GIXRD patterns of all samples. The diffraction peaks at around 42° and 46.3° cannot be attributed to the Si substrate, but to $MnSi_{1.7}$. For the highest fluence sample (5E16), nanoparticles were observed already in the as-implanted state, and they grew from around 5 nm to 15 nm in grain size after annealing. $MnSi_{1.7}$ was also found for a fluence of 1E16 after annealing, while there is no indication of any crystalline nanoparticles in the lowest fluence sample (1E15) even after annealing.

Figure 7.3 shows the magnetization versus field curves (M-H loops) recorded at 10 K. The sample 1E16 RTA shows a clear hysteretic behavior with a saturation of 0.21 μ_B/Mn and a coercivity of 275±25 Oe. In contrast, both samples of 5E16 Asimp and 5E16 RTA show very weak hysteretic behaviors. All other samples (1E16 Asimp, 1E15 Asimp. and 1E15 RTA) did

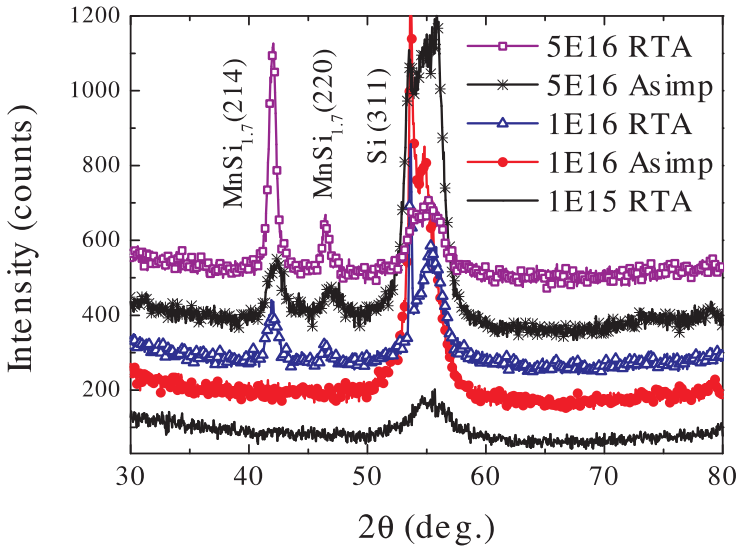

Figure 7.2: XRD grazing incidence scans of all investigated samples implanted with Mn. In some samples two peaks arise, which can be attributed to Mn-silicide nanoparticles ($MnSi_{1.7}$).

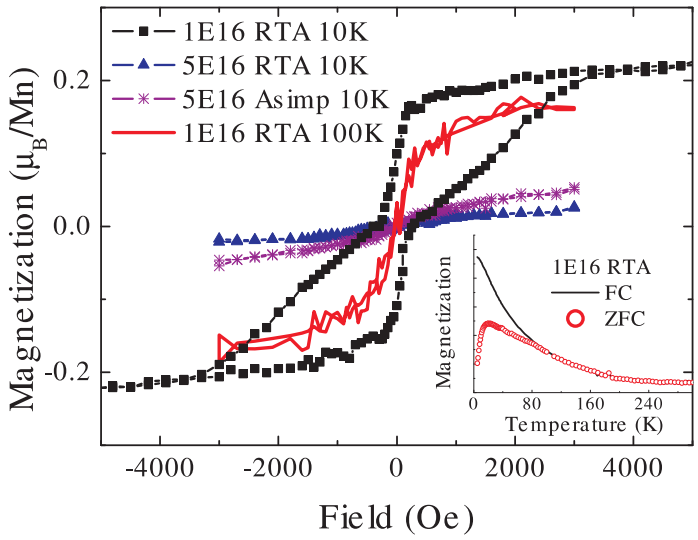

Figure 7.3: M-H hysteresis loops for Mn-implanted Si samples. Only the sample of 1E16 RTA exhibits a clear hysteretic behavior. Inset: ZFC (open circle) and FC (solid line) magnetization curves reveal a typical characteristic of a magnetic nanoparticle system for the sample 1E16 RTA.

not show any detectable magnetism (not shown here). In Ref. [156], single crystalline Mn_4Si_7 ($MnSi_{1.75}$) were reported to exhibit weak itinerant magnetism with an ordering temperature of 47 K and with a very low saturation moment of 0.012 μ_B/Mn. For the nanoparticles embedded in Si, *i.e.* with different surface/volume ratio and undergoing different pressure, the magnetism can be much different from bulk crystals. During intense investigations on MnSi (a weak itinerant magnetic material), the ordering temperature has been found to strongly depend on lattice strain, induced, *e.g.*, by hydrostatic pressure or by the lattice mismatch with substrate [157, 158, 159, 160]. Considering the different grain size of $MnSi_{1.7}$ in our sample, *i.e.* different stress provided by the surrounding lattice, we could explain the dependence of the magnetization on the Mn fluence and post-implantation annealing as following. Those $MnSi_{1.7}$ nanoparticles in the sample (1E16 RTA) have a particular medium grain size, *i.e.* particular lattice deformation or strain, therefore a higher ordering temperature and even a much higher moment (0.21 μ_B/Mn) than the bulk crystal (0.012 μ_B/Mn). In contrast, the bigger nanoparticles in the sample 5E16 RTA are more bulk-like and have very weak ferromagnetism. Those smaller $MnSi_{1.7}$ nanoparticles in other samples (5E16 Asimp. and 1E15 RTA) could be in a rather worse crystalline quality or different strain status, and therefore only show weak or non-detectable ferromagnetism. However an unambiguous reason for the anomalous dependence of the magnetization on the particle size is not yet known.

7.1.4 Conclusion

By investigating Mn-ion implanted Si, the observed ferromagnetism is attributed to $MnSi_{1.7}$ nanoparticles. The magnetization is maximized at a certain medium grain size of $MnSi_{1.7}$ nanoparticles, which could result in a particular strain status, consequently a stronger ferromagnetic coupling.

7.2 TM-implanted TiO_2 (TM=Fe, Co, Ni)

TiO_2 is an alternative wide-bandgap semiconductor promising for DMS formation. The bandgap is 3.0 eV for rutile TiO_2 (3.2 eV for anatase) [161]. Transition metal doped rutile and anatase TiO_2 have been reported to be ferromagnetic above room temperature by various groups [162, 163, 164, 165, 166, 167]. For a comprehensive review, see Ref. [14], in which the controversial attribution of the observed ferromagnetism has been discussed. A correlation between structural and magnetic properties obviously helps to clarify this question.

Figure 7.4 shows the phase transformation of precipitates in TiO_2 upon TM implantation and post annealing.

(1) **Fe implanted TiO_2**: crystalline bcc-Fe and ilmenite $FeTiO_3$ are detected in the as-implanted state already. The annealing at 823 K does not enhance the formation of $FeTiO_3$, but yields more Fe NCs with smaller crystallite size. During annealing at 923 K, both phases

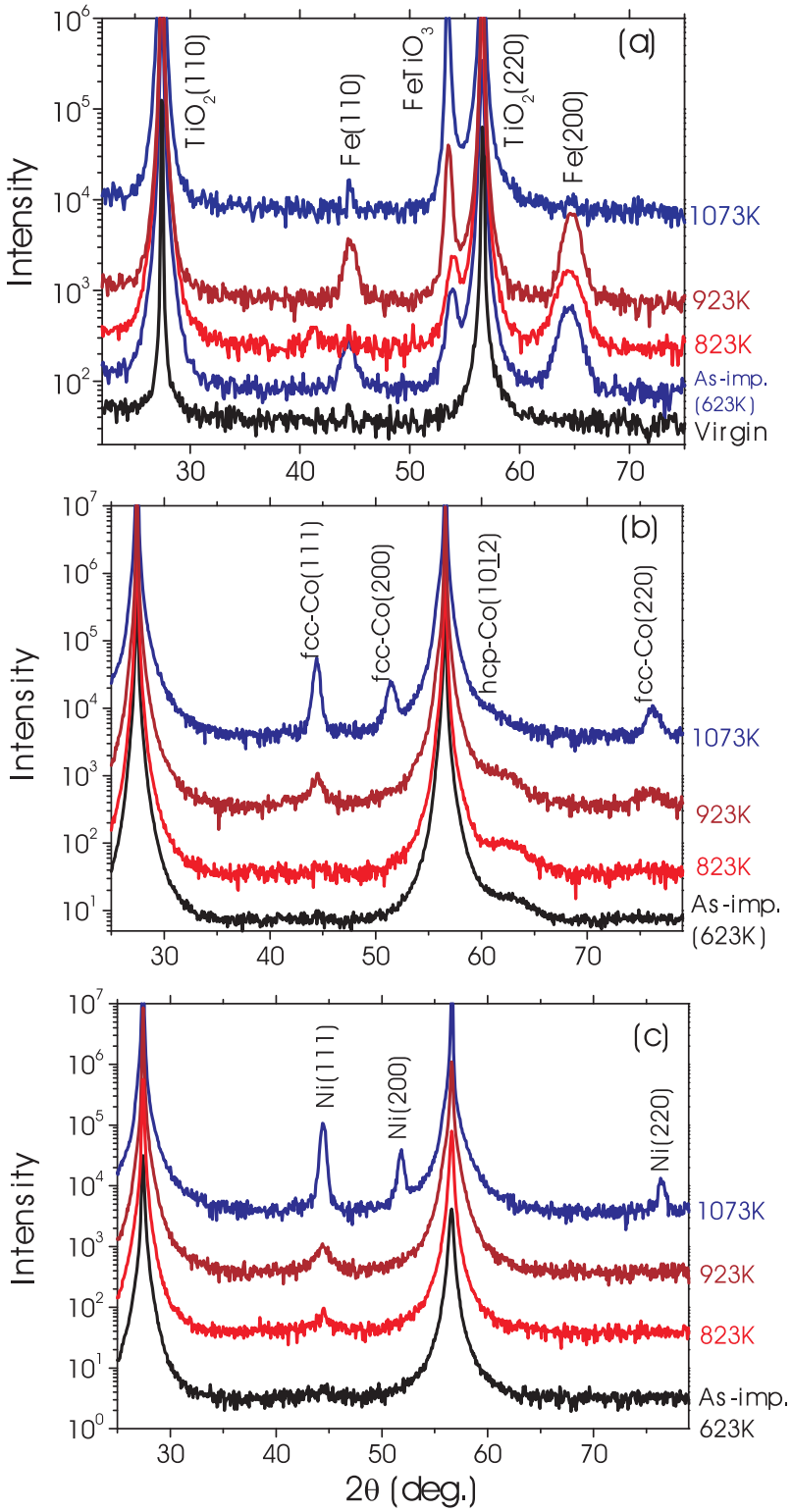

Figure 7.4: SR-XRD symmetric $2\theta/\theta$ scans reveal the crystalline precipitates in TiO_2 implanted with (a) Fe (α-Fe and $FeTiO_3$ form); (b) Co (hcp- and fcc-Co form) and (c) Ni (fcc-Ni forms). Annealing temperatures are indicated.

are growing in grain size, while the amount (peak area) of $FeTiO_3$ is drastically increased. After 1073 K annealing, $FeTiO_3$ is the predominant precipitate at the cost of metallic Fe.

(2) **Co implanted TiO_2**: Hcp-Co forms in the as-implanted state already, and increases after annealing at 823 K. After annealing at 923 K, fcc-Co starts to form, and becomes the predominant secondary phase during annealing at 1073 K. Note that the disappearance of the hcp-Co($10\underline{1}2$) peak.

(3) **Ni implanted TiO_2**: Fcc-Ni is the only secondary phase, and is growing with increasing annealing temperature.

The most noticeable difference between different TM nanocrystals in TiO_2 is the oxidation of Fe after annealing, while metallic Co and Ni nanocrystals are stable up to 1073 K. After annealing at 1073 K, the average crystallite sizes of Co and Ni nanocrystals are above 15 nm. The samples are ferromagnetic above room temperature. The detailed structural and magnetic properties will be reported in Ref. [152].

Chapter 8

Conclusions and future trends

In this thesis, detailed investigations of the structure and the magnetic properties of transition metal (TM) implanted semiconductors, (i) as-purchased ZnO single crystals (ii) pre-annealed ZnO and (iii) Si and TiO_2, have been presented. Various experimental techniques, such as XRD, RBS/channeling, SQUID magnetometry and Mössbauer spectroscopy, have been employed to study the above systems. In an overview, the achievements in this thesis can be summerized as follows: (1) clarify the origin of the ferromagnetism in TM implanted ZnO, TiO_2 and Si, (2) figure out the difficulty to detect nanocrystals embedded inside semiconductors, and (3) find an approach to suppress the formation of secondary phases. Based on these findings, a suggestion for future work is given.

This chapter has been presented in 52 international magnetism and magnetic materials conference as an oral talk, and was published in J. Appl. Phys. **103**, 07D530 (2008).

8.1 Formation of magnetic secondary phases

Fe, Co, Ni and $ZnFe_2O_4$ nanocrystals have been formed inside ZnO upon implantation or after post-annealing. They are responsible for the observed ferromagnetism. For Fe implantation, different implantation fluences and temperatures and post-implantation annealing temperatures have been chosen in order to evaluate the structural and magnetic properties over a wide range of parameters. Three different regimes with respect to the Fe concentration and the process temperature are found: 1) Disperse Fe^{2+} and Fe^{3+} at low Fe concentrations and low processing temperatures, 2) $FeZn_2O_4$ at very high processing temperatures and 3) an intermediate regime with a co-existence of metallic Fe (Fe^0) and ionic Fe (Fe^{2+} and Fe^{3+}). Ferromagnetism is only observed in the latter two cases. The ionic Fe in the last case could contribute to a carrier mediated coupling. However, their separation is too large to couple ferromagnetically due to the lack of p-type carrier.

Concerning their orientation with respect to ZnO host matrix, Fe nanocrystals are different from Co, Ni and $FeZn_2O_4$. Co, Ni and $FeZn_2O_4$ nanocrystals are crystallographically oriented inside ZnO, while Fe is not. This is due to their crystalline symmetry. Hexagonal

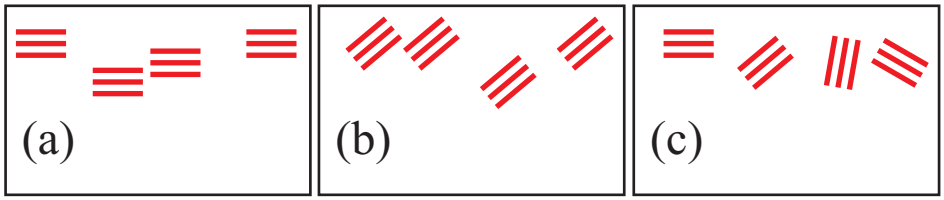

Figure 8.1: Schematic orientation of nanocrystalline precipitates with respect to the substrate.

ZnO(0001) is sixfold symmetric. Fcc- Co, Ni, and $FeZn_2O_4$ are also sixfold symmetric when they are viewed along [111] direction.

For Co NCs, the orientation relationship is hcp-Co(0001)[10$\underline{1}$0]||ZnO(0001)[10$\underline{1}$0]. The samples show magnetic anisotropy, and the easy axis is along hcp-Co[0001], the same as the bulk Co. After annealing at 923 K, fcc-Co is the predominant phase over hcp-Co. The magnetic anisotropy is changed to in-plane. For Ni NCs, the orientation relationship is Ni(111)[112]||ZnO(0001)[10$\underline{1}$0]. The magnetic anisotropy is also observed, however, the easy axis is along Ni[112], which is different from bulk Ni. The structure and magnetic properties are not significantly changed due to the annealing at 823 K. After annealing at 923 K, both Ni and Co-implanted samples exhibit much different magnetic properties with respect to the anisotropy, blocking temperatures and magnetization. The strain induced magnetic anisotropy, and the formation of antiferromagnetic oxides (CoO, and NiO) have been discussed.

8.2 Detecting crystalline secondary phases

The orientation between nanocrystals and substrates has three categories as shown in Figure 8.1. Figure 8.1(a) shows the case of crystallographical orientation, such as Ni and Co in ZnO, with one diffraction plane with large structure factor parallel with the sample surface. In the case of mis-oriented (*e.g.* Co in TiO_2), the precipitates are also crystallographically oriented inside substrates, however, the diffraction planes with large structure factors are not parallel with sample surface. The last case is random orientation. Obviously, in a 2θ-θ scan, the most often used method in phase identification by XRD, crystalline precipitates are easy to be detected in the first case since all precipitates contribute the diffraction intensity, but rather difficult in the last two cases.

8.3 Suppression of secondary phases

An approach, *i.e.* pre-annealing of ZnO substrates, has been established to avoid the formation of secondary phase,. α-Fe nanoparticles are formed in as-purchased ZnO crystals after implantation and post-annealing. In contrast, the same implantation and post-annealing leads the single phase formation in ZnO substrates, which are pre-annealed at high temperature (1273 K) in O_2 or in high vacuum. The saturation magnetization in the pre-annealed

ZnO single crystals is about 20 times lower than for the as-purchased ones and assigned to indirect coupling between isolated Fe ions rather than to clusters.

8.4 Suggestion on future work

8.4.1 Granular magnetic semiconductors

In this thesis, it has been shown that magnetic nanocrystals form inside semiconductors upon transition metal implantation. A straightforward question would be whether granular magnetic semiconductors (GMS) has any potential in spintronics application, which requires the interaction between ferromagnetic inclusions and free carriers in semiconductors.

Actually such coupling has been observed between TM metal thin films separated by a nonmagnetic metal layer. Depending on the thickness of the layers the magnetic films couple ferromagnetically or antiferromagnetically [90]. The coupling mechanism, *i.e.* RKKY interaction, leads to an oscillating polarization of the charge carriers.

An interaction between nanoparticles and free carriers in the host semiconductors, is also expected. For instance, anomalous Hall effect, and giant magnetoresistance have been observed in the GMS systems of MnAs precipitates embedded inside GaAs matrix [63, 67], Fe nanoclusters inside ZnS [91], Co nanoclusters inside TiO_2 [82], and GeMn nanocolumns in Ge [92]. Therefore one would expect that ferromagnetic clusters can actually be used to tailor desirable spintronic functionality [93]. In this thesis, the magnetic and structural properties of ferromagnetic nanocrystals inside ZnO have been carefully correlated. To measure the magneto-transport properties of ferromagnetic nanocrystals inside ZnO would be a task for future work.

8.4.2 Anomalous magnetism induced by defects

Traditional concept on magnetism is related to the spins of unpaired electrons. In this thesis (chapter 6), a weak ferromagnetic response has been detected in pre-annealed virgin ZnO. Such kind of anomalous magnetism has also been observed in Carbon [168], HfO_2 [169], epitaxial thin films of oxides [170], nanoparticles of oxides [171], and Si [172], and has been attributed to defects, *i.e.* the interface or the surface. This defect-induced magnetism is usually temperature independent and high anisotropic. The saturation magnetization (per atom at the interface or on the surface) is very large and decays quickly with time. This direction would be an interesting topic in the point of view of fundamental physics.

Bibliography

[1] G. Binasch, P. Grünberg, F. Saurenbach, and W. Zinn. Enhanced magnetoresistance in layered magnetic structures with antiferromagnetic interlayer exchange. *Phys. Rev. B*, 39:4828–4830, 1989.

[2] M. N. Baibich, J. M. Broto, A. Fert, F. Nguyen Van Dau, F. Petroff, P. Eitenne, G. Creuzet, A. Friederich, and J. Chazelas. Giant Magnetoresistance of (001)Fe/(001)Cr Magnetic Superlattices. *Phys. Rev. Lett.*, 61:2472–2475, 1988.

[3] S. Datta and B. Das. Electronic analog of the electrooptic modulator. *Appl. Phys. Lett.*, 56:665–667, 1990.

[4] G. Schmidt, D. Ferrand, L. W. Molenkamp, A. T. Filip, and B. J. van Wees. Fundamental obstacle for electrical spin injection from a ferromagnetic metal into a diffusive semiconductor. *Phys. Rev. B*, 62:R4790–R4793, 2000.

[5] A. H. Macdonald, P. Schiffer, and N. Samarth. Ferromagnetic semiconductors: moving beyond (Ga, Mn)As. *Nat. Mater.*, 4:195–202, 2005.

[6] T. Jungwirth, K. Y. Wang, J. Masek, K. W. Edmonds, J. Konig, J. Sinova, M. Polini, N. A. Goncharuk, A. H. MacDonald, M. Sawicki, A. W. Rushforth, R. P. Campion, L. X. Zhao, C. T. Foxon, and B. L. Gallagher. Prospects for high temperature ferromagnetism in (Ga,Mn)As semiconductors. *Phys. Rev. B*, 72:13, 2005.

[7] Y. Ohno, D. K. Young, B. Beschoten, F. Matsukura, H. Ohno, and D. D. Awschalom. Electrical spin injection in a ferromagnetic semiconductor heterostructure. *Nature*, 402:790–792, 1999.

[8] D. Chiba, F. Matsukura, and H. Ohno. Electric-field control of ferromagnetism in (Ga,Mn)As. *Appl. Phys. Lett.*, 89:162505, 2006.

[9] M. Tanaka and Y. Higo. Large Tunneling Magnetoresistance in GaMnAs /AlAs /GaMnAs Ferromagnetic Semiconductor Tunnel Junctions. *Phys. Rev. Lett.*, 87:26602, 2001.

[10] S. Humpfner, K. Pappert, J. Wenisch, K. Brunner, C. Gould, G. Schmidt, L. W. Molenkamp, M. Sawicki, and T. Dietl. Lithographic engineering of anisotropies in (Ga,Mn)As. *Appl. Phys. Lett.*, 90:102102, 2007.

[11] T. Dietl, H. Ohno, F. Matsukura, J. Cibert, and D. Ferrand. Zener model description of ferromagnetism in zinc-blende magnetic semiconductors. *Science*, 287:1019–1022, 2000.

[12] T. Fukumura, Y. Yamada, H. Toyosaki, T. Hasegawa, H. Koinuma, and M. Kawasaki. Exploration of oxide-based diluted magnetic semiconductors toward transparent spintronics. *Appl. Surf. Sci.*, 223:62–67, 2004.

[13] C. Liu, F. Yun, and H. Morkoc. Ferromagnetism of ZnO and GaN: A review. *J. Mater. Sci.-Mater. Electron.*, 16:555–597, 2005.

[14] R. Janisch, P. Gopal, and N. A. Spaldin. Transition metal-doped TiO_2 and ZnO - present status of the field. *J. Phys.-Condens. Matter*, 17:R657–R689, 2005.

[15] R. Seshadri. Zinc oxide-based diluted magnetic semiconductors. *Curr. Opin. Solid State Mat. Sci.*, 9:1–7, 2005.

[16] B. T. Matthias, R. M. Bozorth, and J. H. Van Vleck. Ferromagnetic Interaction in EuO. *Phys. Rev. Lett.*, 7:160–161, 1961.

[17] F. Leuenberger, A. Parge, W. Felsch, K. Fauth, and M. Hessler. GdN thin films: Bulk and local electronic and magnetic properties. *Phys. Rev. B*, 72:014427, 2005.

[18] J. K. Furdyna. Diluted magnetic semiconductors. *J. Appl. Phys.*, 64:R29–R64, 1988.

[19] A. Haury, A. Wasiela, A. Arnoult, J. Cibert, S. Tatarenko, T. Dietl, and Y. Merle d'Aubigné. Observation of a Ferromagnetic Transition Induced by Two-Dimensional Hole Gas in Modulation-Doped CdMnTe Quantum Wells. *Phys. Rev. Lett.*, 79:511–514, 1997.

[20] H. Munekata, H. Ohno, S. Vonmolnar, A. Segmuller, L. L. Chang, and L. Esaki. Diluted magnetic iii-v semiconductors. *Phys. Rev. Lett.*, 63:1849–1852, 1989.

[21] H. Ohno, A. Shen, F. Matsukura, A. Oiwa, A. Endo, S. Katsumoto, and Y. Iye. (Ga,Mn)As: A new diluted magnetic semiconductor based on GaAs. *Appl. Phys. Lett.*, 69:363–365, 1996.

[22] K. Sato and H. Katayama-Yoshida. Ferromagnetism in a transition metal atom doped ZnO. *Physica E*, 10:251–255, 2001.

[23] J. M. D. Coey, M. Venkatesan, and C. B. Fitzgerald. Donor impurity band exchange in dilute ferromagnetic oxides. *Nat. Mater.*, 4:173–179, 2005.

[24] U. Ozgur, Y. I. Alivov, C. Liu, A. Teke, M. A. Reshchikov, S. Dogan, V. Avrutin, S. J. Cho, and H. Morkoc. A comprehensive review of ZnO materials and devices. *J. Appl. Phys.*, 98:103, 2005.

[25] S. J. Pearton, D. P. Norton, K. Ip, Y. W. Heo, and T. Steiner. Recent advances in processing of ZnO. *J. Vac. Sci. Technol. B*, 22:932, 2004.

[26] S. J. Han, J. W. Song, C. H. Yang, S. H. Park, J. H. Park, Y. H. Jeong, and K. W. Rhie. A key to room-temperature ferromagnetism in Fe-doped ZnO: Cu. *Appl. Phys. Lett.*, 81:4212–4214, 2002.

[27] N. H. Hong, V. Brize, and J. Sakai. Mn-doped ZnO and (Mn,Cu)-doped ZnO thin films: Does the Cu doping indeed play a key role in tuning the ferromagnetism? *Appl. Phys. Lett.*, 86:082505, 2005.

[28] S. W. Jung, S. J. An, G. C. Yi, C. U. Jung, S. I. Lee, and S. Cho. Ferromagnetic properties of ZnMnO epitaxial thin films. *Appl. Phys. Lett.*, 80:4561–4563, 2002.

[29] M. Bouloudenine, N. Viart, S. Colis, J. Kortus, and A. Dinia. Antiferromagnetism in bulk ZnCoO magnetic semiconductors prepared by the coprecipitation technique. *Appl. Phys. Lett.*, 87:052501, 2005.

[30] S. Yin, M. X. Xu, L. Yang, J. F. Liu, H. Rosner, H. Hahn, H. Gleiter, D. Schild, S. Doyle, T. Liu, T. D. Hu, E. Takayama-Muromachi, and J. Z. Jiang. Absence of ferromagnetism in bulk polycrystalline $Zn_{0.9}Co_{0.1}O$. *Phys. Rev. B*, 73:224408, 2006.

[31] P. Sati, C. Deparis, C. Morhain, S. Schafer, and A. Stepanov. Antiferromagnetic Interactions in Single Crystalline ZnCoO Thin Films. *Phys. Rev. Lett.*, 98:137204, 2007.

[32] M. Fukumura, Z. W. Jin, , M. Kawasaki, T. Shono, T. Hasegawa, S. Koshihara, and H. Koinuma. Magnetic properties of Mn-doped ZnO. *Appl. Phys. Lett.*, 78:958, 2001.

[33] Z. W. Jin, T. Fukumura, M. Kawasaki, K. Ando, H. Saito, T. Sekiguchi, Y. Z. Yoo, M. Murakami, Y. Matsumoto, T. Hasegawa, and H. Koinuma. High throughput fabrication of transition-metal-doped epitaxial ZnO thin films: A series of oxide-diluted magnetic semiconductors and their properties. *Appl. Phys. Lett.*, 78:3824–3826, 2001.

[34] C. N. R. Rao and F. L. Deepak. Absence of ferromagnetism in Mn- and Co-doped ZnO. *J. Mater. Chem.*, 15:573–578, 2005.

[35] Z. Zhang, Q. Chen, H. D. Lee, Y. Y. Xue, Y. Y. Sun, H. Chen, F. Chen, and W. K. Chu. Absence of ferromagnetism in Co-doped ZnO prepared by thermal diffusion of Co atoms. *J. Appl. Phys.*, 100:043909, 2006.

[36] Shengqiang Zhou, K. Potzger, H. Reuther, K. Kuepper, W. Skorupa, M. Helm, and J. Fassbender. Absence of ferromagnetism in V-implanted ZnO single crystals. *J. Appl. Phys.*, 101:09H109, 2007.

[37] A. C. Mofor, A. El-Shaer, A. Bakin, A. Waag, H. Ahlers, U. Siegner, S. Sievers, M. Albrecht, W. Schoch, N. Izyumskaya, V. Avrutin, S. Sorokin, S. Ivanov, and J. Stoimenos. Magnetic property investigations on Mn-doped ZnO layers on sapphire. *Appl. Phys. Lett.*, 87:062501, 2005.

[38] D. W. Abraham, M. M. Frank, and S. Guha. Absence of magnetism in hafnium oxide films. *Appl. Phys. Lett.*, 87:252502, 2005.

[39] Y. Belghazi, G. Schmerber, S. Colis, J. L. Rehspringer, and A. Dinia. Extrinsic origin of ferromagnetism in ZnO and ZnCoO magnetic semiconductor films prepared by sol-gel technique. *Appl. Phys. Lett.*, 89:122504, 2006.

[40] B. Angadi, Y. S. Jung, W. K. Choi, R. Kumar, K. Jeong, S. W. Shin, J. H. Lee, J. H. Song, M. W. Khan, and J. P. Srivastava. Ferromagnetism in 200-MeV Ag+15-ion-irradiated Co-implanted ZnO thin films. *Appl. Phys. Lett.*, 88:142502, 2006.

[41] Y. M. Cho, W. K. Choo, H. Kim, D. Kim, and Y. Ihm. Effects of rapid thermal annealing on the ferromagnetic properties of sputtered $Zn_{1-x}(CoFe)_xO$ thin films. *Appl. Phys. Lett.*, 80:3358–3360, 2002.

[42] J. B. Cui and U. J. Gibson. Electrodeposition and room temperature ferromagnetic anisotropy of Co and Ni-doped ZnO nanowire arrays. *Appl. Phys. Lett.*, 87:133108, 2005.

[43] Y. W. Heo, M. P. Ivill, K. Ip, D. P. Norton, S. J. Pearton, J. G. Kelly, R. Rairigh, A. F. Hebard, and T. Steiner. Effects of high-dose Mn implantation into ZnO grown on sapphire. *Appl. Phys. Lett.*, 84:2292–2294, 2004.

[44] N. H. Hong, J. Sakai, and A. Hassini. Magnetism in V-doped ZnO thin films. *J. Phys.-Condens. Matter*, 17:199–204, 2005.

[45] K. Ip, R. M. Frazier, Y. W. Heo, D. P. Norton, C. R. Abernathy, S. J. Pearton, J. Kelly, R. Rairigh, A. F. Hebard, J. M. Zavada, and R. G. Wilson. Ferromagnetism in Mn- and Co-implanted ZnO nanorods. *J. Vac. Sci. Technol. B*, 21:1476–1481, 2003.

[46] M. Ivill, S. J. Pearton, D. P. Norton, J. Kelly, and A. F. Hebard. Magnetization dependence on electron density in epitaxial ZnO thin films codoped with Mn and Sn. *J. Appl. Phys.*, 97:053904, 2005.

[47] K. R. Kittilstved, N. S. Norberg, and D. R. Gamelin. Chemical manipulation of High-T-C ferromagnetism in ZnO diluted magnetic semiconductors. *Phys. Rev. Lett.*, 94:147209, 2005.

[48] H. J. Lee, S. Y. Jeong, C. R. Cho, and C. H. Park. Study of diluted magnetic semiconductor: Co-doped ZnO. *Appl. Phys. Lett.*, 81:4020–4022, 2002.

[49] H. T. Lin, T. S. Chin, J. C. Shih, S. H. Lin, T. M. Hong, R. T. Huang, F. R. Chen, and J. J. Kai. Enhancement of ferromagnetic properties in ZnCoO by additional Cu doping. *Appl. Phys. Lett.*, 85:621–623, 2004.

[50] X. Liu, F. Lin, L. Sun, W. Cheng, X. Ma, and W. Shi. Doping concentration dependence of room-temperature ferromagnetism for Ni-doped ZnO thin films prepared by pulsed-laser deposition. *Appl. Phys. Lett.*, 88:062508, 2006.

[51] A. Y. Polyakov, A. V. Govorkov, N. B. Smirnov, N. V. Pashkova, S. J. Pearton, K. Ip, R. M. Frazier, C. R. Abernathy, D. P. Norton, J. M. Zavada, and R. G. Wilson. Optical and magnetic properties of ZnO bulk crystals implanted with Cr and Fe. *Mater. Sci. Semicond. Process*, 7:77–81, 2004.

[52] A. Y. Polyakov, A. V. Govorkov, N. B. Smirnov, N. V. Pashkova, S. J. Pearton, M. E. Overberg, C. R. Abernathy, D. P. Norton, J. M. Zavada, and R. G. Wilson. Properties of Mn and Co implanted ZnO crystals. *Solid-State Electronics*, 47:1523–1531, 2003.

[53] A. C. Tuan, J. D. Bryan, A. B. Pakhomov, V. Shutthanandan, S. Thevuthasan, D. E. McCready, D. Gaspar, M. H. Engelhard, J. W. Rogers, K. Krishnan, D. R. Gamelin, and S. A. Chambers. Epitaxial growth and properties of cobalt-doped ZnO on alpha-Al_2O_3 single-crystal substrates. *Phys. Rev. B*, 70:054424, 2004.

[54] M. Venkatesan, C. B. Fitzgerald, J. G. Lunney, and J. M. D. Coey. Anisotropic ferromagnetism in substituted zinc oxide. *Phys. Rev. Lett.*, 93:177206, 2004.

[55] H. Wang, H. B. Wang, F. J. Yang, Y. Chen, C. Zhang, C. P. Yang, Q. Li, and S. P. Wong. Structure and magnetic properties of Zn1-xCoxO single-crystalline nanorods synthesized by a wet chemical method. *Nanotechnology*, 17:4312–4316, 2006.

[56] F. Matsukura, H. Ohno, and T. Dietl. *Handbook of Magnetic Materials*. North-Holland, Amsterdam, 2002.

[57] T. Dietl and H. Ohno. Engineering magnetism in semiconductors. *Materials Today*, 9:18–26, 2006.

[58] P. J. Wellmann, J. M. Garcia, J. L. Feng, and P. M. Petroff. Formation of nanoscale ferromagnetic MnAs crystallites in low-temperature grown GaAs. *Appl. Phys. Lett.*, 71:2532–2534, 1997.

[59] J. DeBoeck, R. Oesterholt, A. VanEsch, H. Bender, C. Bruynseraede, C. VanHoof, and G. Borghs. Nanometer-scale magnetic MnAs particles in GaAs grown by molecular beam epitaxy. *Appl. Phys. Lett.*, 68:2744–2746, 1996.

[60] J. Shi, J. M. Kikkawa, R. Proksch, T. Schaffer, D. D. Awschalom, G. Medeirosribeiro, and P. M. Petroff. Assembly of submicrometer ferromagnets in gallium-arsenide semiconductors. *Nature*, 377:707–710, 1995.

[61] J. P. Zhang, A. K. Cheetham, K. Sun, J. S. Wu, K. H. Kuo, J. Shi, and D. D. Awschalom. Submicron GaMn quasicrystals in ferromagnetic GaAs. *Appl. Phys. Lett.*, 71:143–145, 1997.

[62] H. Akinaga, J. De Boeck, G. Borghs, S. Miyanishi, A. Asamitsu, W. Van Roy, Y. Tomioka, and L. H. Kuo. Negative magnetoresistance in GaAs with magnetic MnAs nanoclusters. *Appl. Phys. Lett.*, 72:3368–3370, 1998.

[63] P. J. Wellmann, J. M. Garcia, J. L. Feng, and P. M. Petroff. Giant magnetoresistance in a low-temperature GaAs/MnAs nanoscale ferromagnet hybrid structure. *Appl. Phys. Lett.*, 73:3291–3293, 1998.

[64] S. U. Yuldashev, Y. Shon, Y. H. Kwon, D. J. Fu, D. Y. Kim, H. J. Kim, T. W. Kang, and X. Fan. Enhanced positive magnetoresistance effect in GaAs with nanoscale magnetic clusters. *J. Appl. Phys.*, 90:3004–3006, 2001.

[65] M. Ramsteiner, H. Y. Hao, A. Kawaharazuka, H. J. Zhu, M. Kastner, R. Hey, L. Daweritz, H. T. Grahn, and K. H. Ploog. Electrical spin injection from ferromagnetic MnAs metal layers into GaAs. *Phys. Rev. B*, 66:4, 2002.

[66] M. Moreno, B. Jenichen, L. Daweritz, and K. H. Ploog. Anisotropic strain fields in granular GaAs : MnAs epitaxial layers: Towards self-assembly of magnetic nanoparticles embedded in GaAs. *J. Vac. Sci. Technol. B*, 23:1700–1705, 2005.

[67] M. Yokoyama, T. Ogawa, A. M. Nazmul, and M. Tanaka. Large magnetoresistance (> 600% of a GaAs : MnAs granular thin film at room temperature. *J. Appl. Phys.*, 99:08D502, 2006.

[68] H. A. K. von Nidda, T. Kurz, A. Loidl, T. Hartmann, P. J. Klar, W. Heimbrodt, M. Lampalzer, K. Volz, and W. Stolz. Tuning the magnetic properties of GaAs : Mn/MnAs hybrids via the MnAs cluster shape. *J. Phys.-Condens. Matter*, 18:6071–6083, 2006.

[69] K. Sato, H. Katayama-Yoshida, and P. H. Dederichs. High curie temperature and nanoscale spinodal decomposition phase in dilute magnetic semiconductors. *Jpn. J. Appl. Phys.*, 44:L948–L951, 2005.

[70] H. Katayama-Yoshida, K. Sato, T. Fukushima, M. Toyoda, H. Kizaki, V. A. Dinh, and P. H. Dederichs. Theory of ferromagnetic semiconductors. *Phys. Status Solidi. A*, 204:15–32, 2007.

[71] K. Potzger, S. Q. Zhou, H. Reuther, A. Mücklich, F. Eichhorn, N. Schell, W. Skorupa, M. Helm, J. Fassbender, T. Herrmannsdorfer, and T. P. Papageorgiou. Fe implanted ferromagnetic ZnO. *Appl. Phys. Lett.*, 88:052508, 2006.

[72] J. H. Shim, T. Hwang, S. Lee, J. H. Park, S. J. Han, and Y. H. Jeong. Origin of ferromagnetism in Fe- and Cu-codoped ZnO. *Appl. Phys. Lett.*, 86:082503, 2005.

[73] T. Shinagawa, M. Izaki, H. Inui, K. Murase, and Y. Awakura. Microstructure and electronic structure of transparent ferromagnetic ZnO-Spinel iron oxide composite films. *Chem. Mater.*, 18:763–770, 2006.

[74] D. P. Norton, M. E. Overberg, S. J. Pearton, K. Pruessner, J. D. Budai, L. A. Boatner, M. F. Chisholm, J. S. Lee, Z. G. Khim, Y. D. Park, and R. G. Wilson. Ferromagnetism in cobalt-implanted ZnO. *Appl. Phys. Lett.*, 83:5488–5490, 2003.

[75] J. H. Park, M. G. Kim, H. M. Jang, S. Ryu, and Y. M. Kim. Co-metal clustering as the origin of ferromagnetism in Co-doped ZnO thin films. *Appl. Phys. Lett.*, 84:1338–1340, 2004.

[76] Shengqiang Zhou, K. Potzger, Gufei Zhang, F. Eichhorn, W. Skorupa, M. Helm, and J. Fassbender. Crystalline Ni nanoparticles as the origin of ferromagnetism in Ni implanted ZnO crystals. *J. Appl. Phys.*, 100:114304, 2006.

[77] R. K. Zheng, H. Liu, X. X. Zhang, V. A. L. Roy, and A. B. Djurisic. Exchange bias and the origin of magnetism in Mn-doped ZnO tetrapods. *Appl. Phys. Lett.*, 85:2589–2591, 2004.

[78] D. C. Kundaliya, S. B. Ogale, S. E. Lofland, S. Dhar, C. J. Metting, S. R. Shinde, Z. Ma, B. Varughese, K. V. Ramanujachary, L. Salamanca-Riba, and T. Venkatesan. On the origin of high-temperature ferromagnetism in the low-temperature-processed Mn-Zn-O system. *Nat. Mater.*, 3:709–714, 2004.

[79] M. Farle. Proceedings of the 36th IFF Spring School. In *Magnetism goes Nano*, page C4.2, Juelich, Germany, 2005.

[80] M. Respaud, J. M. Broto, H. Rakoto, A. R. Fert, L. Thomas, B. Barbara, M. Verelst, E. Snoeck, P. Lecante, A. Mosset, J. Osuna, T. Ould Ely, C. Amiens, and B. Chaudret. Surface effects on the magnetic properties of ultrafine cobalt particles. *Phys. Rev. B*, 57:2925–2935, 1998.

[81] C. P. Bean and J. D. Livingston. Superparamagnetism. *J. Appl. Phys.*, 30:S120–S129, 1959.

[82] S. R. Shinde, S. B. Ogale, J. S. Higgins, H. Zheng, A. J. Millis, V. N. Kulkarni, R. Ramesh, R. L. Greene, and T. Venkatesan. Co-occurrence of superparamagnetism and anoma-

lous Hall effect in highly reduced cobalt-doped rutile TiO_2-delta films. *Phys. Rev. Lett.*, 92:166601, 2004.

[83] Young Sun, M. B. Salamon, K. Garnier, and R. S. Averback. Memory Effects in an Interacting Magnetic Nanoparticle System. *Phys. Rev. Lett.*, 91:167206, 2003.

[84] L. G. Jacobsohn, M. F. Hundley, J. D. Thompson, R. M. Dickerson, and M. Nastasi. Investigation of the magnetic susceptibility of nanocomposites obtained in zero-field-cooled conditions. *J. Vac. Sci. Technol. B*, 24:321–325, 2006.

[85] P. Poddar, Y. Sahoo, H. Srikanth, and P. N. Prasad. Ferromagnetic ordering in nanostructured Mn-doped InP. *Appl. Phys. Lett.*, 87:062506, 2005.

[86] S. Kuroda, N. Nishizawa, K. Takita, M. Mitome, Y. Bando, K. Osuch, and T. Dietl. Origin and control of high-temperature ferromagnetism in semiconductors. *Nat. Mater.*, 6:440, 2007.

[87] D. Bougeard, S. Ahlers, A. Trampert, N. Sircar, and G. Abstreiter. Clustering in a Precipitate-Free GeMn Magnetic Semiconductor. *Phys. Rev. Lett.*, 97:237202, 2006.

[88] T. Song and R.M. Rochko. A preisach model for systems with magnetic order. *Physica B*, 275:24–27, 2000.

[89] Yoshiki Takano, Atsuko Arai, Yumiko Takahashi, Kouichi Takase, and Kazuko Sekizawa. Magnetic properties and specific heat of new spin glass $Mn_{0.5}Fe_{0.5}PS_3$. *J. Appl. Phys.*, 93:8197–8199, 2003.

[90] M.D. Stiles. Interlayer exchange coupling. *J. Magn. Magn. Mater.*, 200:322, 2000.

[91] K. W. Liu, J. Y. Zhang, D. Z. Shen, X. J. Wu, B. H. Li, B. S. Li, Y. M. Lu, and X. W Fan. Magnetic properties and tunneling magnetoresistance effect in Fe–CdFeS granular films. *Appl. Phys. Lett.*, 90:092507, 2007.

[92] M. Jamet, A. Barski, T. Devillers, V. Poydenot, R. Dujardin, P. Bayle-Guillemaud, J. Rothman, E. Bellet-Amalric, A. Marty, J. Cibert, R. Mattana, and S. Tatarenko. High-Curie-temperature ferromagnetism in self-organized $Ge_{1-x}Mn_x$ nanocolumns. *Nat. Mater.*, 5:653–659, 2006.

[93] N. Samarth. Ferromagnetic semiconductors: ruled by a magnetic-rich minority. *Nat. Mater.*, 6:403, 2007.

[94] A. F. Hebard, R. P. Rairigh, J. G. Kelly, S. J. Pearton, C. R. Abernathy, S. N. G. Chu, and R. G. Wilson. Mining for high T-c ferromagnetism in ion-implanted dilute magnetic semiconductors. *J. Phys. D-Appl. Phys.*, 37:511–517, 2004.

[95] J. Ziegler, J. Biersack, and U. Littmark. *The stopping and range of ions in matter*. Pergamon, New York, 1985.

[96] J. W. Rohlf. *Modern Physics from a to Z*. Wiley, 1994.

[97] L. C. Feldman and J. M. Mayer. *Fundamentals of surface and thin film analysis*. North-Holland, New York, 1986.

[98] J. Lindhard. Influence of crystal lattice on motion of charged particles. *Mat. Fys. Medd. Dan. Vid. Selsk.*, 34:1, 1965.

[99] U. Gonser. *Mössbauer Spectroscopy*. Springer-Verlag, 1975.

[100] S. O. Kucheyev, J. S. Williams, C. Jagadish, J. Zou, Cheryl Evans, A. J. Nelson, and A. V. Hamza. Ion-beam-produced structural defects in ZnO. *Phys. Rev. B*, 67:094115, Mar 2003.

[101] S. O. Kucheyev, P. N. K. Deenapanray, C. Jagadish, J. S. Williams, Mitsuaki Yano, Kazuto Koike, Shigehiko Sasa, Masataka Inoue, and Ken ichi Ogata. Electrical isolation of ZnO by ion bombardment. *Appl. Phys. Lett.*, 81:3350–3352, 2002.

[102] Shengqiang Zhou, K. Potzger, H. Reuther, G. Talut, F. Eichhorn, J. von Borany, W. Skorupa, M. Helm, and J. Fassbender. Crystallographically oriented magnetic $ZnFe_2O_4$ nanoparticles synthesized by Fe implantation into ZnO . *J. Phys. D-Appl. Phys.*, 40:964, 2007.

[103] S. O. Kucheyev, J. S. Williams, and S. J. Pearton. Ion implantation into GaN. *Mater. Sci. Eng.*, R33:51, Mar 2001.

[104] V. A. Coleman, H. H. Tan, C. Jagadish, S. O. Kucheyev, and J. Zou. Thermal stability of ion-implanted ZnO. *Appl. Phys. Lett.*, 87:231912, 2005.

[105] B. D. Cullity. *Elements of X-ray Diffractions*. Reading, Addison-Wesley, 1978.

[106] Shengqiang Zhou, K. Potzger, J. von Borany, R. Grötzschel, W. Skorupa, M. Helm, and J. Fassbender. Crystallographically oriented co and ni nanocrystals inside zno formed by ion implantation and postannealing. *Phys. Rev. B*, 77:035209, 2008.

[107] C. Liu, B. Mensching, K. Volz, and B. Rauschenbach. Lattice expansion of Ca and Ar ion implanted GaN. *Appl. Phys. Lett.*, 71:2313–2315, 1997.

[108] C. Ronning, E. P. Carlsonb, and R. F. Davis. Ion implantation into gallium nitride. *Phys. Rep.*, 351:349, 2001.

[109] G. M. Tsoi, L. E. Wenger, U. Senaratne, R. J. Tackett, E. C. Buc, R. Naik, P. P. Vaishnava, and V. Naik. Memory effects in a superparamagnetic gamma-Fe_2O_3 system. *Phys. Rev. B*, 72:014445, 2005.

[110] X. Batlle and A. Labarta. Finite-size effects in fine particles: magnetic and transport properties. *J. Phys. D-Appl. Phys.*, 35:R15, 2002.

[111] Justin M. Shaw, Sukmock Lee, and Charles M. Falco. Overlayer-induced magnetic uniaxial anisotropy in nanoscale epitaxial Fe. *Phys. Rev. B*, 73:094417, 2006.

[112] R. Pulwey, M. Zolfl, G. Bayreuther, and D. Weiss. Magnetic domains in epitaxial nanomagnets with uniaxial or fourfold crystal anisotropy. *J. Appl. Phys.*, 91:7995–7997, 2002.

[113] R. K. Zheng, Hongwei Gu, and X. X. Zhang. Comment on "Memory Effects in an Interacting Magnetic Nanoparticle System". *Phys. Rev. Lett.*, 93:139702, 2004.

[114] M. Sasaki, P. E. Jonsson, H. Takayama, and H. Mamiya. Aging and memory effects in superparamagnets and superspin glasses. *Phys. Rev. B*, 71:104405, 2005.

[115] S. Chakraverty, B. Ghosh, S. Kumar, and A. Frydman. Magnetic coding in systems of nanomagnetic particles. *Appl. Phys. Lett.*, 88:042501, 2006.

[116] E. M. Kaidashev, M. Lorenz, H. von Wenckstern, A. Rahm, H.-C. Semmelhack, K.-H. Han, G. Benndorf, C. Bundesmann, H. Hochmuth, and M. Grundmann. High electron mobility of epitaxial ZnO thin films on c-plane sapphire grown by multistep pulsed-laser deposition. *Appl. Phys. Lett.*, 82:3901–3903, 2003.

[117] M. Lorenz, E. M. Kaidashev, H. von Wenckstern, Riede V., C. Bundesmann, D. Spemann, G. Benndorf, H. Hochmuth, A. Rahm, H.-C. Semmelhack, and M. Grundmann. Optical and electrical properties of epitaxial $(Mg,Cd)_xZn_{1-x}O$, ZnO, and ZnO:(Ga,Al) thin films on c-plane sapphire grown by pulsed laser deposition. *Solid State Electron.*, 47:2205–2209, 2003.

[118] M. Lorenz, R. Johne, T. Nobis, H. Hochmuth, J. Lenzner, M. Grundmann, H. P. D. Schenk, S. I. Borenstain, A. Schon, C. Bekeny, T. Voss, and J. Gutowski. Fast, high-efficiency, and homogeneous room-temperature cathodoluminescence of ZnO scintillator thin films on sapphire. *Appl. Phys. Lett.*, 89:243510, 2006.

[119] C. N. Chinnasamy, A. Narayanasamy, N. Ponpandian, K. Chattopadhyay, H. Guerault, and J. M. Greneche. Magnetic properties of nanostructured ferrimagnetic zinc ferrite. *J. Phys.-Condens. Matter*, 12:7795–7805, 2000.

[120] G. F. Goya and E. R. Low. Ferrimagnetism and spin canting of $ZnFe_2O_4$)-Fe nanoparticles embedded in ZnO matrix. *J. Phys.-Condens. Matter*, 15:641–651, 2003.

[121] H. H. Hamdeh, J. C. Ho, S. A. Oliver, R. J. Willey, G. Oliveri, and G. Busca. Magnetic properties of partially-inverted zinc ferrite aerogel powders. *J. Appl. Phys.*, 81:1851–1857, 1997.

[122] S. Ammar, N. Jouini, F. Fievet, Z. Beji, L. Smiri, P. Moline, M. Danot, and J. M. Greneche. Magnetic properties of zinc ferrite nanoparticles synthesized by hydrolysis in a polyol medium. *J. Phys.-Condens. Matter*, 18:9055–9069, 2006.

[123] Z. H. Zhou, J. Wang, J. M. Xue, and H. S. O. Chan. Cluster glass structure in nanohybrids of nonstoichiometric zinc ferrite in silica matrix. *Appl. Phys. Lett.*, 79:3167–3169, 2001.

[124] D. J. Singh, M. Gupta, and R. Gupta. Density-functional description of spinel $ZnFe_2O_4$. *Phys. Rev. B*, 63:205102, 2001.

[125] S. A. Oliver, H. H. Hamdeh, and J. C. Ho. Localized spin canting in partially inverted $ZnFe_2O_4$ fine powders. *Phys. Rev. B*, 60:3400–3405, 1999.

[126] Murtaza Bohra, Shiva Prasad, Naresh Kumar, D. S. Misra, S. C. Sahoo, N. Venkataramani, and R. Krishnan. Large room temperature magnetization in nanocrystalline zinc ferrite thin films. *Appl. Phys. Lett.*, 88:262506, 2006.

[127] H. Heinke, V. Kirchner, S. Einfeldt, and D. Hommel. X-ray diffraction analysis of the defect structure in epitaxial GaN. *Appl. Phys. Lett.*, 77:2145–2147, 2000.

[128] Y. Suzuki. Epitaxial spinel ferrite thin films. *Annu. Rev. Mater. Res.*, 31:265–289, 2001.

[129] S. Shikazumi. *Physics of Ferromagnetism*. Oxford University Press, Oxford, 1997.

[130] N. Ponpandian and A. Narayanasamy. Influence of grain size and structural changes on the electrical properties of nanocrystalline zinc ferrite. *J. Appl. Phys.*, 92:2770–2778, 2002.

[131] T. Dietl. Self-organized growth controlled by charge states of magnetic impurities. *Nat. Mater.*, 5:673–673, 2006.

[132] J. Narayan, K. Dovidenko, A. K. Sharma, and S. Oktyabrsky. Defects and interfaces in epitaxial ZnO/alpha-Al_2O_3 and AlN/ZnO/alpha-Al_2O_3 heterostructures. *J. Appl. Phys.*, 84:2597–2601, 1998.

[133] U. Kaiser, D.A. Muller, J.L. Grazul, A. Chuvilin, and M. Kawasaki. Direct observation of defect-mediated cluster nucleation. *Nat. Mater.*, 1:102, 2002.

[134] K. Potzger, W. Anwand, H. Reuther, Shengqiang Zhou, G. Talut, G. Brauer, W. Skorupa, and J. Fassbender. The effect of flash lamp annealing on Fe implanted ZnO single crystals. *J. Appl. Phys.*, 101:033906, 2007.

[135] S. Kolesnik, B. Dabrowski, and J. Mais. Structural and magnetic properties of transition metal substituted ZnO. *J. Appl. Phys.*, 95:2582–2586, 2004.

[136] Shengqiang Zhou, K. Potzger, G. Talut, H. Reuther, J. von Borany, R. Grötzschel, W. Skorupa, M. Helm, J. Fassbender, N. Volbers, M. Lorenz, and T. Herrmannsdörfer. Fe-implanted zno: Magnetic precipitates versus dilution. *J. Appl. Phys.*, 103:023902, 2008.

[137] V. M. Kaganer, O. Brandt, A. Trampert, and K. H. Ploog. X-ray diffraction peak profiles from threading dislocations in GaN epitaxial films. *Phys. Rev. B*, 72:045423, 2005.

[138] L. G. Jacobsohn, M. E. Hawley, D. W. Cooke, M. F. Hundley, J. D. Thompson, R. K. Schulze, and M. Nastasi. Synthesis of cobalt nanoparticles by ion implantation and effects of postimplantation annealing. *J. Appl. Phys.*, 96:4444, 2004.

[139] A. Kumar, S. Fahler, H. Schlorb, K. Leistner, and L. Schultz. Competition between shape anisotropy and magnetoelastic anisotropy in Ni nanowires electrodeposited within alumina templates. *Phys. Rev. B*, 73:064421, 2006.

[140] Olga Kazakova, Brian Daly, and Justin D. Holmes. Tunable magnetic properties of metal/metal oxide nanoscale coaxial cables. *Phys. Rev. B*, 74:184413, 2006.

[141] Vassil Skumryev, Stoyan Stoyanov, Yong Zhang, George Hadjipanayis, Dominique Givord, and Josep Nogues. Beating the superparamagnetic limit with exchange bias. *Nature*, 423:850–853, 2003.

[142] A. N. Dobrynin, D. N. Ievlev, K. Temst, P. Lievens, J. Margueritat, J. Gonzalo, C. N. Afonso, S. Q. Zhou, A. Vantomme, E. Piscopiello, and G. Van Tendeloo. Critical size for exchange bias in ferromagnetic-antiferromagnetic particles. *Appl. Phys. Lett.*, 87:012501, 2005.

[143] T. Monteiro, C. Boemare, M. J. Soares, E. Rita, and E. Alves. Photoluminescence and damage recovery studies in Fe-implanted ZnO single crystals. *J. Appl. Phys.*, 93:8995–9000, 2003.

[144] S. Graubner, C. Neumann, N. Volbers, B. K. Meyer, J. Blasing, and A. Krost. Preparation of ZnO substrates for epitaxy: Structural, surface, and electrical properties. *Appl. Phys. Lett.*, 90:042103, 2007.

[145] Marcel H. F. Sluiter, Y. Kawazoe, Parmanand Sharma, A. Inoue, A. R. Raju, C. Rout, and U. V. Waghmare. First Principles Based Design and Experimental Evidence for a ZnO-Based Ferromagnet at Room Temperature. *Phys. Rev. Lett.*, 94:187204, 2005.

[146] A. Quesada, M. A. Garcia, M. Andres, A. Hernando, J. F. Fernandez, A. C. Caballero, M. S. Martin-Gonzalez, and F. Briones. Ferromagnetism in bulk Co-Zn-O. *J. Appl. Phys.*, 100:113909, 2006.

[147] K. C. Prince, M. Matteucci, K. Kuepper, S. G. Chiuzbaian, S. Bartkowski, and M. Neumann. Core-level spectroscopic study of FeO and FeS_2. *Phys. Rev. B*, 71:085102, 2005.

[148] C. Sudakar, J. S. Thakur, G. Lawes, R. Naik, and V. M. Naik. Ferromagnetism induced by planar nanoscale CuO inclusions in Cu-doped ZnO thin films. *Phys. Rev. B*, 75:054423, 2007.

[149] L. S. Dorneles, M. Venkatesan, M. Moliner, J. G. Lunney, and J. M. D. Coey. Magnetism in thin films of CaB_6 and SrB_6. *Appl. Phys. Lett.*, 85:6377–6379, 2004.

[150] A. Bayer E. Goering, S. Gold and G. Schuetz. Non-symmetric influences in the total electron yield x-ray magnetic circular dichroism signal in applied magnetic fields. *J. Synchrotron Rad.*, 8:434, 2001.

[151] Shengqiang Zhou, K. Potzger, Gufei Zhang, A. Mücklich, F. Eichhorn, N. Schell, R. Grotzschel, B. Schmidt, W. Skorupa, M. Helm, J. Fassbender, and D. Geiger. Structural and magnetic properties of Mn-implanted Si. *Phys. Rev. B*, 75:085203, 2007.

[152] Shengqiang Zhou, K. Potzger, G. Talut, J. von Borany, R. Grötschel, W. Skorupa, M. Helm, and J. Fassbender. Crystallographically oriented Fe nanocrystals formed in Fe-implanted TiO_2. $J.Appl.Phys.$, 103 : 083907, 2008.

[153] M. Bolduc, C. Awo-Affouda, A. Stollenwerk, M. B. Huang, F. G. Ramos, G. Agnello, and V. P. LaBella. Above room temperature ferromagnetism in Mn-ion implanted Si. *Phys. Rev. B*, 71:033302, 2005.

[154] Y. C. Lian and L. J. Chen. Localized epitaxial growth of $MnSi_{1.7}$ on silicon. *Appl. Phys. Lett.*, 48:359–361, 1986.

[155] M. F. Wu, J. De Wachter, A.-M. Van Bavel, R. Moons, A. Vantomme, H. Pattyn, G. Langouche, H. Bender, J. Vanhellemont, K. Temst, and Y. Bruynseraede. Structural characterization of ion-beam synthesized $NiSi_2$ layers. *J. Appl. Phys.*, 78:1707–1712, 1995.

[156] U. Gottlieb, A. Sulpice, B. Lambert-Andron, and O. Laborde. Magnetic properties of single crystalline Mn_4Si_7. *J. Alloys Compd.*, 361:13, 2003.

[157] C. Pfleiderer, S. R. Julian, and G. G. Lonzarich. Non-Fermi-liquid nature of the normal state of itinerant-electron ferromagnets. *Nature*, 414:427, 2001.

[158] K. Koyama, T. Goto, T. Kanomata, and R. Note. Observation of an itinerant metamagnetic transition in MnSi under high pressure. *Phys. Rev. B*, 62:986–991, 2000.

[159] K. Schwinge, C. Müller, A. Mogilatenko, J. J. Paggel, and P. Fumagalli. Structure and magneto-optic Kerr measurements of epitaxial MnSi films on Si(111). *J. Appl. Phys.*, 97:103913, 2005.

[160] W. Yu, F. Zamborszky, J. D. Thompson, J. L. Sarrao, M. E. Torelli, Z. Fisk, and S. E. Brown. Phase Inhomogeneity of the Itinerant Ferromagnet MnSi at High Pressures. *Phys. Rev. Lett.*, 92:086403, 2004.

[161] S Kitazawaa, Y Choib, S Yamamotoc, and T Yamaki. Rutile and anatase mixed crystal TiO_2 thin films prepared by pulsed laser deposition. *Thin Solid Films*, 515:1901–1904, 2006.

[162] Y. Matsumoto, M. Murakami, T. Shono, T. Hasegawa, T. Fukumura, M. Kawasaki, P. Ahmet, T. Chikyow, S. Koshihara, and H. Koinuma. Room-temperature ferromagnetism in transparent transition metal-doped titanium dioxide. *Science*, 291:854–856, 2001.

[163] Y Matsumoto, R Takahashi, M Murakami, T Koida, X Fan, T Hasegawa, T Fukumura, M Kawasaki, S Koshihara, and H Koinuma. Ferromagnetism in Co-Doped TiO_2 Rutile Thin Films Grown by Laser Molecular Beam Epitaxy. *Jpn. J. Appl. Phys.*, 40:L1204–L1206, 2003.

[164] N. H. Hong, W. Prellier, J. Sakai, and A. Hassini. Fe- and Ni-doped $TiO_2$2 thin films grown on $LaAlO_3$ and $SrTiO_3$ substrates by laser ablation. *Appl. Phys. Lett.*, 84:2850–2852, 2004.

[165] R. Suryanarayanan, V. M. Naik, P. Kharel, P. Talagala, and R. Naik. Room temperature ferromagnetism in spin-coated anatase- and rutile-$Ti_{0.95}Fe_{0.05}O_2$ films. *J. Phys.-Condens. Matter*, 17:755–762, 2005.

[166] K. Inaba, T. Hitosugi, Y. Hirose, Y. Furubayashi, G. Kinoda, Y. Yamamoto, T. W. Kim, H. Fujioka, T. Shimada, and T. Hasegawa. Magnetic properties of rutile $Ti_{1-x}Fe_xO_2$ epitaxial thin films. *Jpn. J. Appl. Phys.*, 45:L114–L116, 2006.

[167] T. Hitosugi, G. Kinoda, Y. Yamamoto, Y. Furubayashi, K. Inaba, Y. Hirose, K. Nakajima, T. Chikyow, T. Shimada, and T. Hasegawa. Carrier induced ferromagnetism in Nb doped Co : TiO_2 and Fe : TiO_2 epitaxial thin film. *J. Appl. Phys.*, 99:08M121, 2006.

[168] P. Esquinazi, D. Spemann, R. Höhne, A. Setzer, K.-H. Han, and T. Butz. Induced Magnetic Ordering by Proton Irradiation in Graphite. *Phys. Rev. Lett.*, 91:227201, 2003.

[169] M. Venkatesan, C. B. Fitzgerald, and J. M. D. Coey. Thin films: Unexpected magnetism in a dielectric oxide. *Nature*, 430:650, 2004.

[170] Nguyen Hoa Hong, Joe Sakai, Nathalie Poirot, and Virginie Brizé. Room-temperature ferromagnetism observed in undoped semiconducting and insulating oxide thin films. *Phys. Rev. B*, 73:132404, 2006.

[171] A. Sundaresan, R. Bhargavi, N. Rangarajan, U. Siddesh, and C. N. R. Rao. Ferromagnetism as a universal feature of nanoparticles of the otherwise nonmagnetic oxides. *Phys. Rev. B*, 74:161306, 2006.

[172] G. Kopnov, Z. Vager, and R. Naaman. New Magnetic Properties of Silicon/Silicon Oxide Interfaces. *Adv. Mater.*, 19:925, 2007.

Appendix A

Publications

Paper published or accepted

1. K. Potzger, ***Shengqiang Zhou***, H. Reuther, A. Mücklich, F. Eichhorn, N. Schell, W. Skorupa, M. Helm, J. Fassbender, T. Herrmannsdörfer and T. P. Papageorgiou, Fe implanted ferromagnetic ZnO, Appl. Phys. Lett. **88**, 052508 (2006). [Chapter 4]

2. K. Potzger, ***Shengqiang Zhou***, F. Eichhorn, M. Helm, W. Skorupa, A. Mücklich, J. Fassbender, T. Herrmannsdörfer, and A. Bianchi, Ferromagnetic Gd-implanted ZnO single crystals, J. Appl. Phys. **99**, 114304 (2006).

3. K. Potzger, H. Reuther, ***Shengqiang Zhou***, A. Mücklich, R. Grötzschel, F. Eichhorn, M. O. Liedke, J. Fassbender, H. Lichte, and A. Lenk, Ion beam synthesis of Fe nanoparticles in MgO and yttria-stabilized zirconia, J. Appl. Phys. **99**, 114304 (2006).

4. ***Shengqiang Zhou***, K. Potzger, Gufei Zhang, F. Eichhorn, W. Skorupa, M. Helm, and J. Fassbender, Crystalline Ni nanoparticles as the origin of ferromagnetism in Ni implanted ZnO crystals, J. Appl. Phys. **100**, 114304 (2006). [Chapter 5]

5. ***Shengqiang Zhou***, K. Potzger, Gufei Zhang, A. Mücklich, F. Eichhorn, N. Schell, R. Grötzschel, B. Schmidt, W. Skorupa, M. Helm, J. Fassbender, and D. Geiger, Structural and magnetic properties of Mn-implanted Si. Phys. Rev. B **75**, 085203 (2007). [Chapter 7]

6. K. Potzger, ***Shengqiang Zhou***, H. Reuther, K. Kuepper, G. Talut, M. Helm, J. Fassbender and J. D. Denlinger, Suppression of secondary phase formation in Fe implanted ZnO single crystals, Appl. Phys. Lett. **91**, 062107 (2007). [Chapter 6]

7. ***Shengqiang Zhou***, K. Potzger, H. Reuther, K. Kuepper, W. Skorupa, M. Helm, and J. Fassbender, Absence of ferromagnetism in v-implanted zno single crystals. J. Appl. Phys. 101, 09H109 (2007).

8. K. Potzger, W. Anwand, H. Reuther, ***Shengqiang Zhou***, G. Talut, G. Brauer, W. Skorupa, and J. Fassbender, The effect of flash lamp annealing on Fe implanted ZnO single crystals. J. Appl. Phys. **101**, 033906 (2007). [Chapter 4]

9. G. Talut, H. Reuther, ***Shengqiang Zhou***, K. Potzger, F. Eichhorn, and F. Stromberg Ferromagnetism in GaN induced by Fe ion implantation, J. Appl. Phys. **102**, 083909 (2007).

10. ***Shengqiang Zhou***, K. Potzger, H Reuther, G Talut, F Eichhorn, J von Borany, W Skorupa, M Helm and J Fassbender, Crystallographically oriented magnetic $ZnFe_2O_4$ nanoparticles synthesized by Fe implantation into ZnO, J. Phys. D-Appl. Phys. **40**, 964 (2007). [Chapter 4]

11. ***Shengqiang Zhou***, K. Potzger, J. von Borany, R. Grötzschel, W. Skorupa, M. Helm, and J. Fassbender, Crystallographically oriented Co and Ni nanocrystals inside ZnO formed by ion implantation and post-annealing, Phys. Rev. B **77**, 035209 (2008). [Chapter 5]

12. ***Shengqiang Zhou***, K. Potzger, G. Talut, H Reuther,J. von Borany, R. Grötzschel, W. Skorupa, M. Helm,1 J. Fassbender, N. Volbers, M. Lorenz and T. Herrmannsdörfer, Fe implanted ZnO: magnetic precipitates versus dilution, J. Appl. Phys. **103**, 023902 (2008). [Chapter 4]

13. ***Shengqiang Zhou***, K. Potzger, K. Kuepper, J. Grenzer, M. Helm, J. Fassbender, E. Arenholz, and J. Denlinger, Ni implanted ZnO single crystals - correlation between nanoparticle formation and defect structure, J. Appl. Phys. **103**, 043901 (2008). [Chapter 6]

14. ***Shengqiang Zhou***, K. Potzger, G. Talut, J. von Borany, W. Skorupa, M. Helm, and J. Fassbender, Using X-ray diffraction to identify precipitates in transition metal doped semiconductors, J. Appl. Phys. **103**, 07D530 (2008). [Chapter 8]

15. ***Shengqiang Zhou***, K. Potzger, G. Talut, A. Shalimov, J. Grenzer, W. Skorupa, M. Helm, J. Fassbender, E. Cizmar, S. A. Zvyagin, and J. Wosnitza, Crystallographically oriented Fe nanocrystals formed in Fe-implanted TiO_2, J. Appl. Phys. **103**, 083907 (2008). [Chapter 7]

16. ***Shengqiang Zhou***, K. Potzger, G. Talut, Q. Xu, H. Reuther, K. Kuepper, J. Grenzer, M. Helm, J. Fassbender, and E. Arenholz, Ferromagnetic ZnO - a purely defect induced phenomenon, J. Phys. D: Appl. Phys. **41**, 105011 (2008). [Chapter 6]

17. Qingyu Xu, Heidemarie Schmidt, ***Shengqiang Zhou***, Kay Potzger, Manfred Helm, Holger Hochmuth, Michael Lorenz, Annette Setzer, Pablo Esquinazi, Christoph Meinecke, and Marius Grundmann, Appl. Phys. Lett. **92**, 082508 (2008).

18. K. Potzger, ***Shengqiang Zhou***, J. Grenzer, M. Helm, J. Fassbender, An easy mechanical way to create ferromagnetic defective ZnO, Appl. Phys. Lett., accepted (2008).

19. G. Talut, K. Potzger, A. Mücklich, and ***Shengqiang Zhou***, Formation of metallic clusters in oxide insulators by means of ion beam mixing, J. Appl. Phys. **103**, 07D505 (2008).

20. ***Shengqiang Zhou***, K. Potzger, *et al.* , Structural and magnetic properties of Tb implanted into ZnO single crystals, Nucl. Instrum. Methods Phys. Res. B **266**, 589 (2008).

21. N. Volbers, S. Lautenschläger, T. Leichtweiss, A. Laufer, S. Graubner, B. Meyer, K. Potzger, and ***Shengqiang Zhou***, Arsenic Doped Zinc Oxide, J. Appl. Phys. accepted (2008).

22. V. Cantelli, J. von Borany, A. Mücklich, ***Shengqiang Zhou***, *et al.* Influence of energetic ions and neutral atoms on the L10 ordering of FePt films, Nucl. Instrum. Methods Phys. Res. B 257, 406 (2007).

Paper submitted or in preparation

1. Gufei Zhang, K. Potzger, ***Shengqiang Zhou***, *et al.* Memory effect of magnetic nanoparticle systems originating from particle size distribution, Nucl. Instrum. Methods Phys. Res. B to be submitted (2008).

2. ***Shengqiang Zhou***, K. Potzger, K. Kuepper, M. Helm, and J. Fassbender, Substitution and mobility of rare earth ions inside ZnO, Nucl. Instrum. Methods Phys. Res. B, in preparation (2007).

Conference presentation

1. Ferromagnetic Gd-implanted ZnO single crystals, ***Oral talk***, DPG Frühjahrstagung 2006, 27.-31.03.2006, Dresden, Germany.

2. Magnetic nanoparticle formation in Fe implanted ZnO, Poster, E-MRS IUMRS ICEM 2006 Spring Meeting, 29.05.-02.06.2006, Nice, France.

3. Ferromagnetic $ZnFe_2O_4$ synthesized by Fe implantation into ZnO, Poster, The 4th International Conference on Physics and Applications of Spin Related Phenomena in Semiconductors, 15.-18.08.2006, Sendai, Japan.

4. Mn-silicide nanoparticles: the origin of ferromagnetism in Mn-implanted Si? Poster, IBMM 2006, 18.-22.09.2006, Taormina, Italy.

5. Probing the nanoscaled phase separation in DMS materials by synchrotron radiation XRD, Poster, ESRF user meeting 2007, Grenoble, France, and Oral talk at work shop

on "Ion beam processing and magnetic properties of semiconductors", KU Leuven, Belgium, 13.02.2007, Leuven, Belgium

6. Thermal phase transformation and perpendicular exchange coupling of Co nanocrystals embedded in ZnO, ***Oral talk***, DPG Frühjahrstagung , 26.-30.03.2007, Regensburg

7. Absence of ferromagnetism in V implanted ZnO crystals, Poster, 51th Magnetism and magnetic materials conference, 7-11.01.2007, Baltimore, USA.

8. Magnetic and structural properties of nanocrystals embedded in semiconductors, ***Oral talk***, 52th Magnetism and magnetic materials conference, 5-9.11.2007, Tampa, USA.

Appendix B

Curriculum vitae

Personal data

Name:	Shengqiang Zhou
Birthday:	16 Aug. 1976
Birth place:	Shandong, China
Family status:	married with Rong Xiang

Education

Sep. 1992 - Jul. 1995	No. 1 High school of Yuncheng, China
Sep. 1995 - Jul. 1999	Bachelor degree in ScienceBeijing (Peking) University, China
Sep. 1999 - Jul. 2002	Master degree in Science with honors Beijing (Peking) University, China Thesis: Characterization and modification of GaN-based optoelectronics materials
Oct. 2002 - Dec. 2004	PhD student K.U.Leuven, Belgium Topic: Structure characterization of III-nitrides alloys by RBS/channeling and XRD
Jan. 2005 - Dec. 2007	PhD student Forschungszentrum Dresden-Rossendorf/TU-Dresden, Germany Topic: Correlation between structure and magnetism in transition metal implanted semiconductors

Short-term advanced school

Feb. 2005	Magnetism goes Nano 36th Spring School, Jülich, Germany
May 2005	Ion beam, photon and hyperfine methods in nano-structure materials Madrid, Spain

Teaching

Sep. 2000 - Jan. 2001	Teaching assistant at Beijing (Peking) University Lecture: Laboratory of Nuclear Physics for undergraduate student
Mar. 2006 - Jan. 2007	Teaching assistant at TU-Dresden Lecture: Laboratory of Fundamental Physics

Erklärung

Hiermit versichere ich, daß ich die vorliegende Arbeit ohne unzulässige Hilfe Dritter und ohne Benutzung anderer als der angegebenen Hilfsmittel angefertigt habe; die aus fremden Quellen direkt oder indirekt übernommenen Gedanken sind als solche kenntlich gemacht. Die Arbeit wurde bisher weder im Inland noch im Ausland in gleicher oder ähnlicher Form einer anderen Prüfungsbehörde vorgelegt.

Diese Dissertation wurde angefertigt im

Forschungszentrum Dresden-Rossendorf
Institut für Ionenstrahlphysik und Materialforschung
Postfach 51 01 19
01314 Dresden

Die wissenschaftliche Betreuung der Arbeit erfolgte durch Prof. Dr. Manfred Helm.

Ich versichere, an keiner Institution, auch nicht im Ausland, jemals den Antrag auf Eröffnung eines Promotionsverfahrens gestellt zu haben.

Ich erkenne die Promotionsordnung der Fakultät Mathematik und Naturwissenschaften der Technischen Universität Dresden an.

Dresden, den 07.12.2007

Shengqiang Zhou